Title
Engineering the Mesoporous Silica Nanoparticles to Chelate to Metal Ions for Bioapplications

Author
Yu, Chia Jung

Publication Date
2018

Peer reviewed|Thesis/dissertation

UNIVERSITY OF CALIFORNIA

Los Angeles

Engineering the Mesoporous Silica Nanoparticles to Chelate to Metal Ions for Bioapplications

A dissertation submitted in partial satisfaction of the requirements for the degree Doctor of Philosophy in Biochemistry and Chemistry

by

Chia Jung Yu

2018

ABSTRACT OF THE DISSERTATION

Engineering the mesoporous silica nanoparticles to chelate to metal ions for bioapplications

by

Chia Jung Yu

Doctor of Philosophy in Biochemistry and Chemistry

University of California, Los Angeles, 2018

Professor Jeffrey I. Zink, Chair

This dissertation focuses on improving cancer therapies and imaging by utilizing non-harmful material such as metal ions to replace traditional cancer therapies. The three chapters of this dissertation are presented as follows: 1. *In Vitro* Delivery of Calcium Ions by Nanogated Mesoporous Silica Nanoparticles to Induce Cancer Cellular Apoptosis. 2. Enhanced Fenton Reaction for Reactive Oxygen Species Generation by Iron Ion-Loaded Mesoporous Silica Nanoparticles for Cancer Therapy. 3. Cellular uptake efficiency study of enhanced T_1 relaxivity gadolinium loaded iminodiacetic acid modified mesoporous silica nanoparticle.

This dissertation of Chia Jung Yu is approved.

Xiangfeng Duan

Timothy J. Deming

Fuyuhiko Tamanoi

Jeffrey I. Zink, Committee Chair

University of California, Los Angeles

2018

Table of contents

Acknowledgments

In my life, there are a lot of people I have to thank. Thanks to my family and family friend Mrs. Min-Jhu Wu Jhang for helping me discover what I wanted to pursue after I finished my undergraduate program. While I was hesitating and struggling through the applications for graduate school, my family and Mrs. Jhang were always by my side, and encouraged me to pursue a higher degree in the U.S.

My mentor, Prof. Jeffrey I. Zink, guided, taught, and supported me through these six years. He helped me build the capabilities of logical thinking, troubleshooting, and finding scientific ideas. I feel very lucky to have met him and have him as my first boss.

I am fortunate to have been mentored and trained by many wonderful labmates. To Dr. Juyao Dong and Dr. Janie Chen, thank you for training me in my first year after joining the Zink group. Juyao taught me all the particle synthesis and the characterization techniques that I would use during the remainder of my studies. Janie helped me adjust to the lab life, and kept me company during my most stressful times of grad school. To Dr. Angela Hwang, thanks for the training on ICP-OES and tissue digestions. These techniques actually were the most important and fundamental to my research.

I want to thank to our CNSI collaborators as well. Thanks to Dr. Chong Hyun Chang (Paul) for training me on all the analytical instruments. Thanks to Dr. Xiang Wang and Dr. Han Liao for teaching and discussing with me about all the cell assays. I learned all the biology techniques from them.

To Prof. Fuyu Tamanoi, thanks for sharing the cell room with me so that I have a chance to learn many cell studies.

To my first granduncle and grandaunt, Aunt Susanna, Uncle David, cousins Christina and Rita, thanks for inviting me over for all the family gatherings through these six years in LA. All of you have made me feel that here is just like home. Your support and encouragement always gave me motivation to continue my research.

To my family, grandparents, parents, and brothers, thanks for all the financial, emotional, and physical support. Thanks for giving me a chance to start a life in the U.S.

To Corey Mynatt, thanks for being an awesome boyfriend, friend, and for mentally supporting me.

Vita

2011	Bachelor of Science in Chemistry National Tsing Hua University, Taiwan
2013-2018	Research Assistant Zink Research Group University of California Los Angeles, CA

Chapter 1

1.1 Introduction of mesoporous silica nanoparticles (MSNs) (MCM-41 as the model)

In order to make a nanoparticle-based delivery platform suitable for bio-applications, there are some requirements that should be satisfied. First, it is necessary that the nanoparticles have a suitable size that can utilize the enhanced permeability and retention effect (EPR).[1,2] From previous studies, researchers have found that 100 nm diameter and spherical silica nanoparticles increase the circulation time in the body, increasing the chance of reaching the tumor and accumulating.[3,4] Also, it is known that the endothelial cells of the blood vessel walls possess large gaps between cells compared to normal healthy tissue, which have tight junctions.[5] These gaps within the endothelial cell layer provide the nanoparticles a way to escape from blood vessels and enter tumor cells, which is a form of passive targeting. The second requirement for a nanocarrier is biocompatibility, which is confirmed by many studies.[5–7] The third requirement is that the nanocarrier possess a suitable level of available porous volume for loading cargo. The fourth requirement is the availability of Si-OH groups on the surface of the silica nanoparticle. The Si-OH groups provide the possibility of modifying the silica surface with various organic compounds such as targeting agents, polymers as a capping system, or bulky molecules shown in figure 1.7.2.

1.2 Synthesis of MSNs

The most widely used synthesis method of mesoporous silica nanoparticles is the base-catalyzed sol–gel process.[8] The sol-gel process includes hydrolysis and condensation.

Hydrolysis: $OH^- + Si(OR)_4 \rightarrow Si(OR)_3OH + RO^-$ (1)

Condensation: $SiO^- + Si(OH)_4 \rightarrow Si–O–Si + OH^-$ (2)

The sol–gel process utilizes the hydrolysis of organosilane precursors (Tetraethyl orthosilicate, (TEOS), for MCM-41 and condensation reactions of hydrolyzed $SiOH_4$. The small colloidal particles within the sol then condense into the gel phase.

In order to control the morphology and the pore structure, templating agents are needed. The common method of making templates is to use surfactant to form micelles and allow the hydrolyzed silica precursors to be directed to condense around the micelles and form the ordered silica structures. In a typical synthesis of the 100 nm MCM-41 type mesoporous silica nanoparticles (figure 1.7.3), the silica source, tetraethyl orthosilicate (TEOS), is added into a heated basic (pH 11) aqueous solution of the templating surfactant, cetyltrimethyl ammonium bromide (CTAB). 100 nm diameter nanoparticles are formed through base-catalyzed sol–gel condensation around the hexagonally packed micelle structures. After aging, the resulting nanoparticles are refluxed in acidic alcohol to decrease the interactions between the surfactant and the silica frame, and remove the surfactants from the mesopores. Transmittance electron microscopy and X-ray diffraction confirm that the hexagonal arrays of pores remain intact after the surfactant removal process. The solvent extracted particles are spherical in shape, roughly 100 nanometers in diameter, and contain 2D-hexagonally arranged pores 2–3 nanometers in diameter (figure

1.7.3).

1.3 Surface modification of MSNs

The surface of MSNs have an abundance of silanol (Si-O-H) groups inside the pores and the outer surface.[9] The silanol groups can react with various alkoxysilanes to change the surface properties of the MSN surface. The introduced organic functionalities can have the properties of active targeting, hydrophilia or hydrophobia, carrying positive charge or negative charge, or carrying different polymers, as shown in figure 1.7.2.[10–13] The introduced molecules can have responses to various external excitations such as light,[13] heat,[14] or ultrasound.[15] As a result, the surface functionality opens up the potential for controllable cargo delivery or other applications.

There are some common methods to introduce organic functionalities onto MSNs. The surface silanol groups are deprotonated at neutral pH; as a result, the surface of MSN is negatively charged. The negatively charged $Si\text{-}O^-$ can non-covalently bond to positively charged polymers through electrostatic attraction. Another way to functionalize the surface of MSNs is through covalent bonding to organic molecules, which has two main routes: co-condensation and post-grafting.[16–19] The co-condensation route involves mixing the various alkoxysilanes with organoalkoxysilanes first, which are then added into a basic solution for hydrolysis and condensation. This method has more organic functional groups inside the pore walls, since the organoalkoxysilanes are spread throughout the particle structure. The post-grafting procedure modifies the surface of the MSN after synthesis. The method is to utilize the surface-accessible silanol groups to react with introduced alkoxysilanes or organoalkoxysilanes. The outer surface silanes are

more accessible to the introduced silanes compared to the silanes in the interior pore walls; however, the size of introduced silanes must also be considered. The modification can be performed prior to extracting the templating agent. The templating agent can then be removed, and the protected, unreacted silanol groups in the pore interiors can be further modified. In this way, functionalization can be directed.

1.4 Active targeting property of MSNs

As mentioned in section 1.1, the enhanced permeability and retention effect (EPR) increases the accumulation of MSNs in the tumors. Xia *et al.* successfully demonstrated that the polyethyleneimine (PEI) coating enhances the cellular uptake of MSNs through EPR effect.[20] Despite the success in developing MSN that passively accumulate at the tumor sites, the cell-specific targeting still relies on the active targeting to increase the treatment efficacy. Selective targeting strategies employ ligands that specifically interact with receptors on the cell surface of interest to promote nanocarrier binding and internalization. Lu *et al.* showed the enhanced efficacy of suppressing the pancreatic tumor growth with the help of folic acid-conjugated MSNs.[21]

1.5 Potential metal ions to replace traditional cancer drugs

1.5.1 Calcium ion (Ca^{2+})

Calcium ions (Ca^{2+}) are essential to mammals and control some key biochemistry functions in cells and organisms.[22] For example, Ca^{2+} acts as a messenger in signal transduction pathways in the nervous system, and a cofactor in various enzymes.[22–24] Extracellular Ca^{2+} is responsible for maintaining the potential difference across the cell

membranes and bone formation.[25] The Ca^{2+} concentration in mammals is highly regulated inside and outside the cells. Ca^{2+} ions enter into the cytoplasm either from outside the cell through the calcium channels, or are released from intracellular storage such as mitochondria and endoplasmic reticuli. Recent studies have found that unregulated intracellular Ca^{2+} concentration is related to apoptosis.[26,27] The Ca^{2+} acts as a messenger that coordinates mitochondrial–endoplasmic reticulum interactions that drive apoptosis (figure 1.7.4). The Ca^{2+} in cytoplasm can trigger the cytochrome *c* to be released from mitochondria. The cytochrome *c* can bind to inositol-1,4,5- trisphosphate ($InsP_3$) receptors on the endoplasmic reticulum (ER) membrane and then promote calcium conductance to form a positive feedback loop. The released calcium then triggers more cytochrome *c* released from all mitochondria in the cell, thus activating the caspases and nuclease enzymes that finalize the apoptotic process.[26,27] By artificially delivering a large amount of Ca^{2+} to the cell cytoplasm, we hope to disturb the Ca^{2+} concentration to stimulate this apoptotic cycle and induce cellular death in cancer cells. This strategy can be an alternative to using traditional, costly, and more hazardous chemotherapy drugs. All the details are demonstrated in Chapter 2.

1.5.2 Iron ion

Another essential metal ion for life is iron.[28,29] Iron is the most abundant metal in humans - for example, about 3-4 grams of iron exist in a healthy adult. About 75% of existing iron in healthy adults is found in the oxygen-transporting protein hemoglobin in the red blood corpuscles, the muscle oxygen storage protein myoglobin, or stored by ferritin and hemosiderin. The rest of the iron is bound to the various iron enzymes and

redox proteins, or is being transported through the blood by transferrin. Iron-containing enzymes are also responsible for many redox reactions whereby electron transport is facilitated by changes in the oxidation state of the metal.[29] One of the redox reactions in cells is called the Fenton reaction. The Fenton reaction was first described by H. J. H. Fenton in 1894, and involves the oxidation of organic substrates by iron (II or III) and hydrogen peroxide (H_2O_2).[30]

$$Fe^{2+} + H_2O_2 \rightarrow Fe^{3+} + \cdot OH + OH^- \quad (1)$$

$$Fe^{3+} + H_2O_2 \rightarrow Fe^{2+} + \cdot OOH + H^+ \quad (2)$$

There is evidence showing that H_2O_2 concentration in cells is related to cancer development.[31] The increased cellular level of H_2O_2 has been related to some cancer cell features such as DNA alterations, cell proliferation, apoptosis resistance, metastasis, angiogenesis and hypoxia-inducible factor 1 (HIF-1) activation. Here, we tried to develop a new cancer treatment strategy by utilizing the high H_2O_2 in cancer cells combined with the Fenton reaction to produce extra reactive oxygen species (ROS) to trigger cell death. After cell death, the iron will be released from cells and will be diluted after entering the blood stream; as a result, the toxicity of this treatment is very low. The details are described in Chapter 3.

1.5.3 Gadolinium ion (Gd^{3+})

Magnetic resonance imaging (MRI) has emerged as a widely used clinical diagnostic technique to detect infected tissues, tumors, and infarction.[32–36] MRI is non-invasive and does not involve X-rays, which is different from computed tomography (CT) scans. However, the sensitivity of MRI still needs to be improved.[36,37] MRI is

unable to distinguish early stage tumors or inflammation from healthy tissues. As a result, the contrast agents have been developed to improve the visibility of the internal body in MRI.[38,39] An effective MRI contrast agent should have a strong effect on the longitudinal ($1/T_1$) and transverse ($1/T_2$) relaxation rates of water protons.[40] The current commercialized contrast agents are based on gadolinium because of its seven unpaired electrons and relatively long electronic relaxation. Also, for stability reasons and safety, most of the known contrast agents use multidentate ligands such as Magnevist ($[Gd(DTPA)(H_2O)]^{2-}$, where DTPA is diethylenetriaminepentaacetic acid), Dotarem ($[Gd(DOTA)(H_2O)]$, where DOTA is 1,4,7,10-tetraazacyclododecane-1,4,7,10-tetraacetic acid), etc.[41–43]

However, commercially available contrast agents have some limitations, including a lack of targeting properties, and a low sensitivity, which prevent them from detecting early stage tumors.[44] Here, we developed a potential contrast agent, which has a high cancer cell uptake, and 7 times longer longitudinal rate compared to Magnevist. All the details are in Chapter 4.

1.6 Determine the suitable system to deliver metal ions

As mentioned above, the MCM-41 type of mesoporous silica nanoparticles have found a variety of applications in many fields due to their large pore volume, easily accessible pores, well-established surface chemistry, and high rate of endocytosis by mammalian cells, all of which make them versatile nanocontainers. Combined with the highly accessible surface modification properties, various controllable stimuli-responsive releasing cargo molecules from the pores have been developed to include polymer

networks,[45] supramolecular nanovalves,[46] snap-tops,[47] biomolecules,[13] light responsive nanogates,[48] magnetic field responsive nanogates,[14] nanoimpellers,[49] and cleavable chemical bonds.[15] These methods have demonstrated the stimulated release of a variety of ~1−2nm sized cargo molecules, but are unable to hold back small cargoes such as metal ions (1-2 Å) in pores. In order to use Ca and Fe ions as cancer therapies, and Gd ions for MRI imaging, the reversible chelation on nanoparticles is necessary. From previous work published by Derrick Tarn, coordination chemistry was used in order to achieve the objective of carrying and releasing both metal ions and biologically useful small molecules.[50]

In Tarn's system, the pore opening was controlled by a system including a swinging gate with a latch assembled on MSNs.[50] For realizing this system, iminodiacetic acid (IDA), a chelating agent, is selected as the gate and a metal ion integrated as the latch.[51] Two gates can freely swing on hinges or be locked in place with a latch. The metal ions as the latch here serves a dual purpose of being a desired cargo type and latching the gates shut. When the swinging gates are situated around the pore openings, these gates can control the entrance to the pore interiors shown in figure 1.7.5.

Iminodiacetic acid has a chelating property and chemical structure similar to that of one-half of an ethylenediaminetetraacetic acid (EDTA) molecule. When IDA is attached to the surface of silica nanoparticles with a flexible linker, two neighboring IDA molecules can bind strongly to a metal ion such as Co^{2+} and Ni^{2+}.[51,52] The IDA binding constant with various metal centers exhibits an ~ 10^3 decrease if changing the pH from neutral to mildly acidic as a result of protonation of the carboxylate groups.[53] This mechanism is the basis of the operation of the pH-responsive nano-swinging gates.

Neighboring two IDA molecules chelate to the introduced metal ion forming a complex of $M(IDA)_2$ such as $Co(IDA)_2$, $Ni(IDA)_2$.[54] When the chelation occurs over a pore opening, the system can trap and release molecules into and from the pores (figure 1.7.5 and 1.7.6). Since IDA can form stable complexes with many different transition metal ions, this system can function with a variety of different metal latches.[51] This swinging gate system from Derrick Tarn was chosen for the study of delivering Ca, Fe, and Gd ions for cancer therapies and imaging. The synthesis procedure of IDA-modified MSNs was slightly modified and optimized in order to have maximum coverage of IDA on the MSNs to increase the ion loading.

1.7 Figures

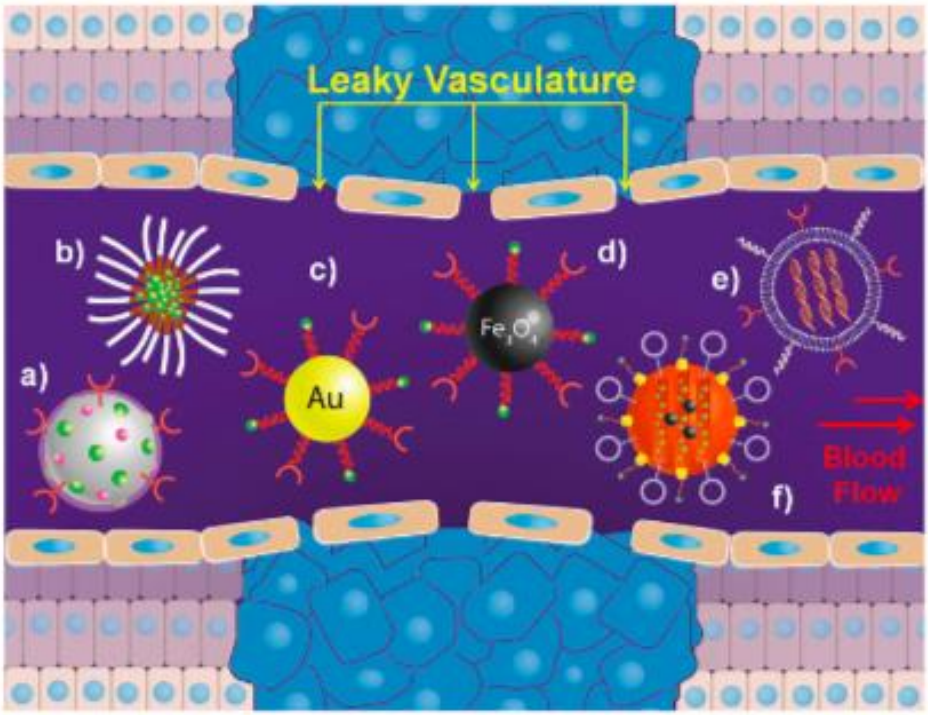

Figure 1.7.1. The demonstration of how a nanoparticle with the suitable size can utilize the enhanced permeability and retention effect (EPR) to escape from the blood stream through the leaky vasculature and enter the tumor cells. Various types of nanoparticles are depicted in the site of tumor growth in this cartoon representation. Here are the demonstrations of (a) polymeric nanogel, (b) polymeric micelle, (c) gold nanoparticle, (d) iron oxide nanoparticle, (e) siRNA ensconced in a liposome delivery vector, and (f) a stimuli-responsive capped mesoporous silica nanoparticle. The targeting ligands on the nanoparticles are shown as circles or semi-circles. Cargo, conjugated or encapsulated internally, is shown as green spheres. Purple spheres represent imbedded contrast agents. (Figure adapted from Chem. Soc. Rev., 2012, 41, 2590–2605)

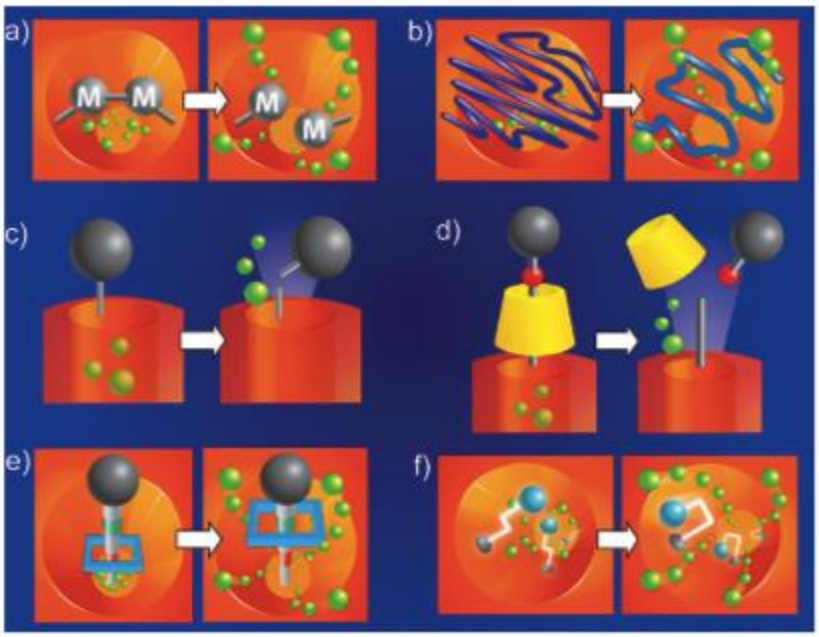

Figure 1.7.2. The six examples of controllable pore opening systems for mesoporous silica nanoparticle. The pore opening mechanisms are based on stimuli responsive delivery systems. The pore opening can be closed and open by (a) synthesizing molecules (e.g. coumarin) within the pore channels and then controlling the forming and breaking of covalent bonds between the molecules; (b) grafting polymer chains on the particle surface and then controlling the shrinking and swelling properties of the polymer; (c) attaching bulky groups (e.g. Au, CdS nanocrystals) over the pore openings and removing it when it's needed; (d) attaching a cyclic torus molecule in this ''snap-top'' design consisting of a [2]rotaxane with a bulky stopper and then by changing the interactions between torus molecule and the bulky stopper; (e) shuttling of a cyclic molecule along a molecular stalk towards and away from the pore opening in a supramolecular ''nanovalve'' design; (f) modifying the azobenzene molecules within the pore channels to hinder the diffusion of the encapsulated cargo molecules, whereas the activation of the wagging motion resulting from the cis-trans photoisomerization of the azobenzene pushes the cargo molecules out

of the mesopores. (Figure is adapted from *Chem. Soc. Rev.,* 2012, 41, 2590–2605)

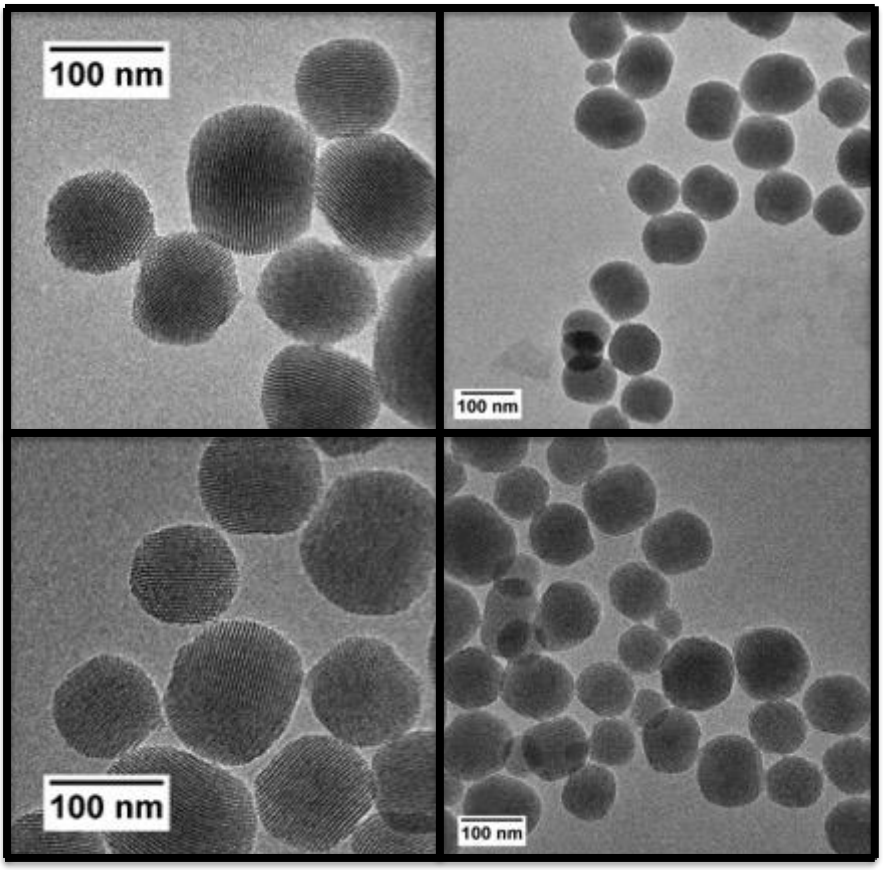

Figure 1.7.3. TEM images of MCM-41 type of mesoporous silica nanoparticle. The scale bar for TEM is 100 nm. The TEM image shows the clearly ordered pore channels.

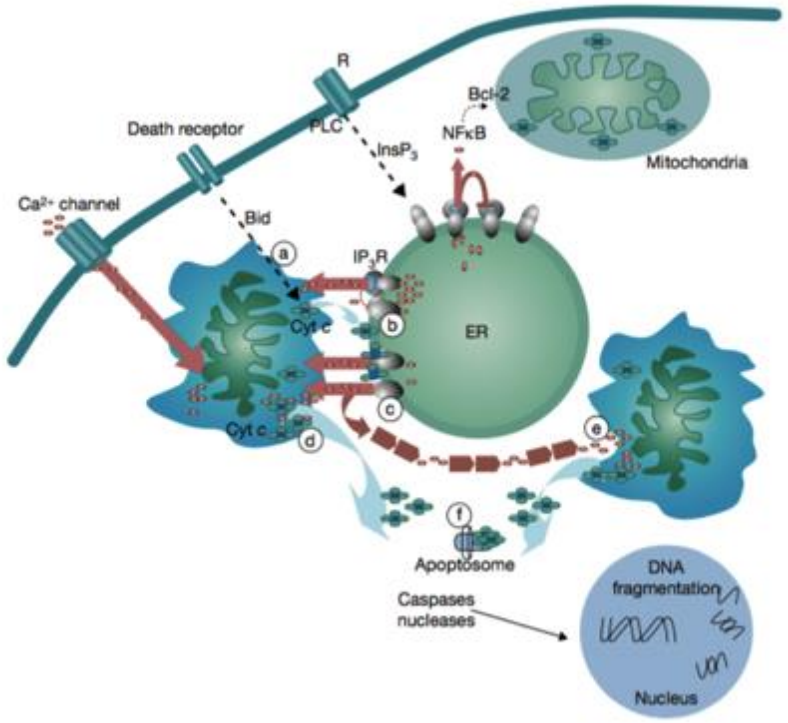

Figure 1.7.4 Description of how calcium as messengers in the cells can induce apoptosis. When the cell goes through unregulated calcium influx via plasma membrane channels, cell surface death receptors become activated, and apoptosis can be triggered. After the calcium enters the cells, the calcium can diffuse into the mitochondrion, or bind to the protein Bid on the mitochondrial membrane, inducing a permeability transition in the membrane of an adjacent mitochondrion, resulting in the release of cytochrome *c* (Cyt c) from that mitochondrion (**a**). Cytochrome *c* will then diffuse through to nearby endoplasmic reticulum (ER) and bind to $InsP_3$ receptors (**b**), thus enhancing calcium release from the endoplasmic reticulum (**c**). This calcium from the ER causes an increase in the cytoplasmic calcium concentration (**d**), resulting in calcium uptake by mitochondria. This triggers the release of cytochrome *c* from all of the mitochondria in the cell (**e**). The cytochrome *c* in the cytoplasm causes the apoptosome to form, leading to

the activation of caspases (**f**). Caspases and nucleases finalize the cell death process by cleaving protein substrates (caspases) and DNA (nucleases). (Figure adapted from *Nat. Cell Biol.*, 2003, **5**, 1041–1043)

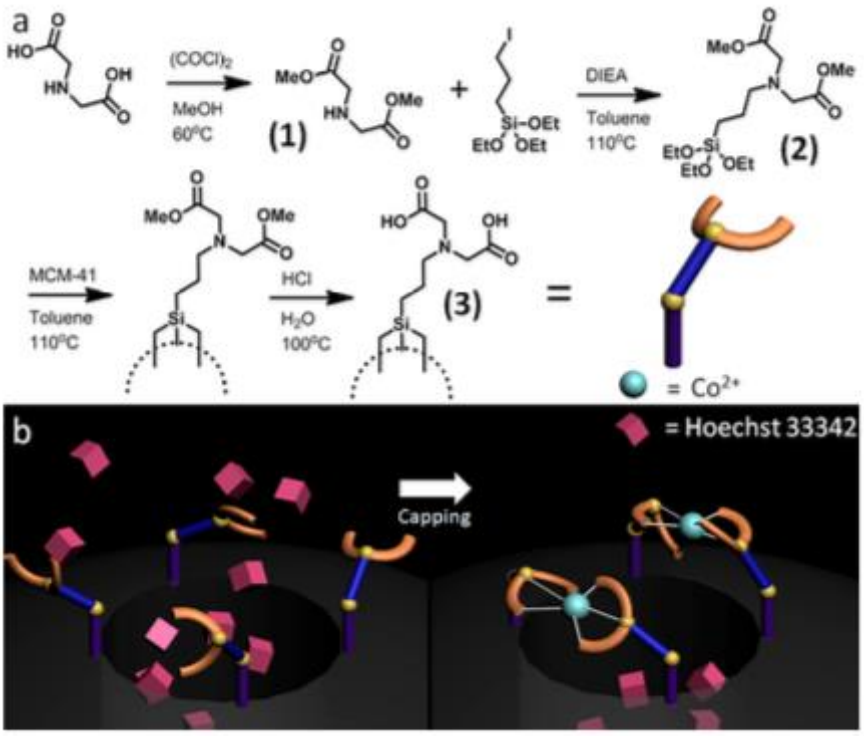

Figure 1.7.5. (a) The synthesis scheme of IDA-MSNs. Showing from the synthesis of IDA silane precursor to the attachment of IDA silane precursor onto the silica nanoparticle surface. (b) Demonstration of the swinging gate assembly and disassembly process to open or closed the pores. IDA-modified MCM-41 nanoparticles were loaded with Hoechst 33342 first, and then the nanogate was latched by chelating to Co^{2+}. (figure adapted from *Inorg. Chem.*, 2013, **52**, 2044–2049.)

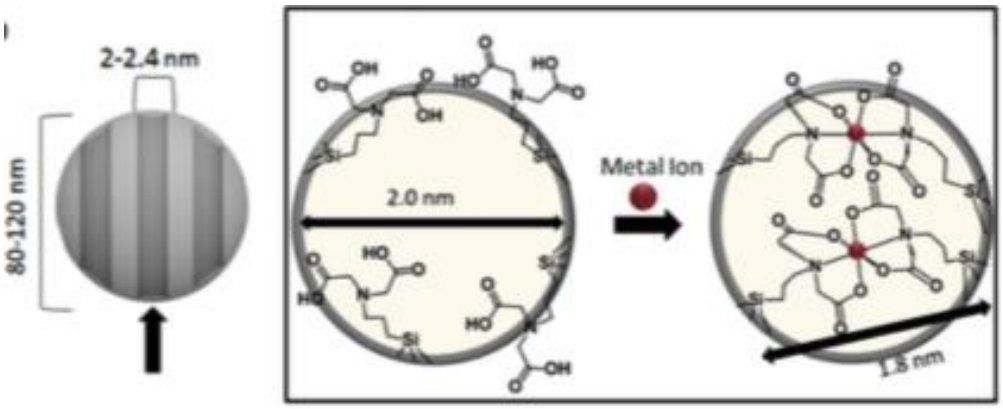

Figure 1.7.6. The illustration of the IDA modified pore channels of MSN. In the open state, the IDA groups are freely swinging and the pores are open, but the introduction of metal ions binds with IDA molecules and creates an inorganic complex across over the pore opening. (figure adapted from *Inorg. Chem.*, 2013, **52**, 2044–2049.)

1.8 References

1 H. Maeda, J. Wu, T. Sawa, Y. Matsumura and K. Hori, *J. Control. Release*, 2000, **65**, 271–284.

2 A. K. Iyer, G. Khaled, J. Fang and H. Maeda, *Drug Discov. Today*, 2006, **11**, 812–818.

3 X. Huang, X. Teng, D. Chen, F. Tang and J. He, *Biomaterials*, 2010, **31**, 438–448.

4 Y.-S. Lin and C. L. Haynes, *J Am Chem Soc*, 2010, **132**, 4834–4842.

5 Z. Li, J. C. Barnes, A. Bosoy, J. F. Stoddart and J. I. Zink, *Chem. Soc. Rev.*, 2012, **41**, 2590.

6 F. Tang, L. Li and D. Chen, *Adv. Mater.*, 2012, **24**, 1504–1534.

7 A. Popat, S. B. Hartono, F. Stahr, J. Liu, S. Z. Qiao and G. Qing (Max) Lu, *Nanoscale*, 2011, **3**, 2801.

8 L. P. Singh, S. K. Bhattacharyya, R. Kumar, G. Mishra, U. Sharma, G. Singh and S. Ahalawat, *Adv. Colloid Interface Sci.*, 2014, **214**, 17–37.

9 J. Kecht, A. Schlossbauer, T. Bein, S. Huh, J. W. Wiench, J. C. Yoo, M. Pruski and V. S. Y. Lin, *Chem. Mater.*, 2008, **15**, 7207–7214.

10 Y. Zhang, C. Y. Ang, M. Li, S. Y. Tan, Q. Qu, Z. Luo and Y. Zhao, *ACS Appl. Mater. Interfaces*, 2015, **7**, 18179–18187.

11 M. Xue, D. Cao, J. F. Stoddart and J. I. Zink, *Nanoscale*, 2012, **4**, 7569–7574.

12 S. Angelos, E. Choi, F. Vögtle, L. De Cola and J. I. Zink, *J. Phys. Chem. C*, 2007, **111**, 6589–6592.

13 B. Ruehle, D. L. Clemens, B.-Y. Lee, M. A. Horwitz and J. I. Zink, *J. Am. Chem. Soc.*, 2017, **139**, 6663–6668.

14 B. Rühle, S. Datz, C. Argyo, T. Bein and J. I. Zink, *Chem. Commun.*, 2016, **52**, 1843–1846.

15 J. L. Paris, M. V. Cabanas, M. Manzano and M. Vallet-Regí, *ACS Nano*, 2015, **9**, 11023–11033.

16 A. Calvo, M. Joselevich, G. J. A. A. Soler-Illia and F. J. Williams, *Microporous Mesoporous Mater.*, 2009, **121**, 67–72.

17 S. Huh, J. W. Wiench, J. C. Yoo, M. Pruski and V. S. Y. Lin, *Chem. Mater.*, 2003, **15**, 4247–4256.

18 Z. Hua, W. Bu, Y. Lian, H. Chen, L. Li, L. Zhang, C. Li and J. Shi, *J. Mater. Chem.*, 2005, **15**, 661–665.

19 J. W. Park, Y. J. Park and C. H. Jun, *Chem. Commun.*, 2011, **47**, 4860–4871.

20 T. Xia, M. Kovochich, M. Liong, H. Meng, S. Kabehie, S. George, J. I. Zink and A. E. Nel, *ACS Nano*, 2009, **3**, 3273–3286.

21 J. Lu, Z. Li, J. I. Zink and F. Tamanoi, *Nanomedicine Nanotechnology, Biol. Med.*, 2012, **8**, 212–220.

22 D. E. Clapham, *Cell*, 2007, **131**, 1047–1058.

23 L. Mellgren, *FASEB J.*, 1987, **1**, 110–115.

24 B. Ahvazi, K. M. Boeshans, W. Idler, U. Baxa and P. M. Steinert, *J. Biol. Chem.*, 2003, **278**, 23834–23841.

25 T. L. Arinzeh, T. Tran, J. Mcalary and G. Daculsi, *Biomaterials*, 2005, **26**, 3631–3638.

26 M. P. Mattson and S. L. Chan, *Nat. Cell Biol.*, 2003, **5**, 1041–1043.

27 S. Orrenius, B. Zhivotovsky and P. Nicotera, *Nat. Rev. Mol. Cell Biol.*, 2003, **4**,

552–565.

28 A. L. Feig and S. J. Lippard, *Chem. Rev.*, 1994, **94**, 759–805.

29 S. J. Oppenheimer, *J. Nutr.*, 2001, **131**, 616–635.

30 C. C. Winterbourn, *Toxicol. Lett.*, 1995, **82**–**83**, 969–974.

31 M. López-Lázaro, *Cancer Lett.*, 2007, **252**, 1–8.

32 J. N. Giedd, J. Blumenthal, N. O. Jeffries, F. X. Castellanos, H. Liu, A. Zijdenbos, T. Paus, A. C. Evans and J. L. Rapoport, *Nat. Neurosci.*, 1999, **2**, 861–863.

33 L. Lemieux, G. Hagemann, K. Krakow and F. G. Woermann, *Magn. Reson. Med.*, 1999, **42**, 127–135.

34 J. Ding, M. L. Eigenbrodt, T. H. Mosley, R. G. Hutchinson, A. R. Folsom, T. B. Harris and F. J. Nieto, *Stroke*, 2004, **35**, 16–21.

35 S. C. Partridge, J. E. Gibbs, Y. Lu, L. J. Esserman, D. Tripathy, D. S. Wolverton, H. S. Rugo, E. S. Hwang, C. A. Ewing and N. M. Hylton, *AJR. Am. J. Roentgenol.*, 2005, **184**, 1774–81.

36 A. I. Garcia-Diez, L. H. Ros Mendoza, V. M. Villacampa, M. Cizar and M. I. Fuertes, *Eur. Radiol.*, 2000, **10**, 462–466.

37 B. A. Moffat, T. L. Chenevert, T. S. Lawrence, C. R. Meyer, T. D. Johnson, Q. Dong, C. Tsien, S. Mukherji, D. J. Quint, S. S. Gebarski, P. L. Robertson, L. R. Junck, A. Rehemtulla and B. D. Ross, *Proc. Natl. Acad. Sci.*, 2005, **102**, 5524–5529.

38 P. Caravan, J. J. Ellison, T. J. McMurry and R. B. Lauffer, *Chem. Rev.*, 1999, **99**, 2293–2352.

39 J. P. Stack, O. M. Redmond, M. B. Codd, P. A. Dervan and J. T. Ennis, *Radiology*,

1990, **174**, 491–494.

40 P. Caravan, *Chem. Soc. Rev.*, 2006, **35**, 512.

41 H. Mondor and R. Ziekenhuis, *Neuroradiology*, 1994, **36**, 27–30.

42 H. P. Niendorf, J. C. Dinger, J. Haustein, I. Cornelius, A. Alhassan and W. Clauß, *Eur. J. Radiol.*, 1991, **13**, 15–20.

43 E. Healy, R. Hesselink, G. A. Press and S. Middleton, *Radiology*, 1987, **165**, 619–624.

44 S. H. Heywang, A. Wolf, E. Pruss, T. Hilbertz, W. Eiermann and W. Permanetter, *Radiology*, 1989, **171**, 95–103.

45 L. Xing, H. Zheng, Y. Cao and S. Che, *Adv. Mater.*, 2012, **24**, 6433–6437.

46 R. Liu, Y. Zhang and P. Feng, *J. Am. Chem. Soc.*, 2009, **131**, 15128–15129.

47 T. M. Guardado-Alvarez, L. Sudha Devi, M. M. Russell, B. J. Schwartz and J. I. Zink, *J. Am. Chem. Soc.*, 2013, **135**, 14000–14003.

48 D. He, X. He, K. Wang, J. Cao and Y. Zhao, *Langmuir*, 2012, **28**, 4003–4008.

49 J. Liu, W. Bu, L. Pan and J. Shi, *Angew. Chemie - Int. Ed.*, 2013, **52**, 4375–4379.

50 D. Tarn, M. Xue and J. I. Zink, *Inorg. Chem.*, 2013, **52**, 2044–2049.

51 Z. el Rassi and C. Horváth, *J. Chromatogr. A*, 1986, **359**, 241–253.

52 S. K. Seth, I. Saha, C. Estarellas, A. Frontera, T. Kar and S. Mukhopadhyay, *Cryst. Growth Des.*, 2011, **11**, 3250–3265.

53 S. Chaberek and A. E. Martell, *J. Am. Chem. Soc.*, 1952, **74**, 5052–5056.

54 E. Hochuli, H. Döbeli and A. Schacher, *J. Chromatogr. A*, 1987, **411**, 177–184.

Chapter 2

In Vitro Delivery of Calcium Ions by Nanogated Mesoporous Silica Nanoparticles to Induce Cancer Cellular Apoptosis

Published: *Molecular Systems Design & Engineering.* Mol. Syst. Des. Eng., ***2017***, *2*, *384–392*

2.1 Abstract

A pH operated nanogate on mesoporous silica nanoparticles (MSN) capable of a simultaneous dual-cargo delivery of both metal ions and organic cargo molecules was used to deliver both Hoechst 33342 nuclear stain and calcium ions to MiaPaCa-2 cancer cells. Delivery of calcium to the cell cytoplasm to induce cellular death is an attractive alternative to using traditional, more hazardous chemotherapy drugs. Treatment of cancer cells with Hoechst loaded, calcium latched nanogate-modified MSNs resulted in the autonomous release of both cargo types, as visualized by cell nuclei staining and calcium-induced apoptosis. Apoptosis was confirmed by observation of nuclear fragmentation, chromatin condensation, and Western-blotting for cleaved caspase-3.

2.2 Introduction

Mesoporous silica nanoparticles loaded with drugs and controlled by stimuli-response release mechanisms make it possible to deliver the drugs to cancer cells with no premature release.[1–5] Ingenious methods of using external control[6] (such as light[7,8], magnetic fields[9–11], ultrasound[12]) or autonomous control caused by cell-specific changes (such as pH[13–16], redox potential[17–19], enzymes[20–22] and other biomolecules[23,24]) have been developed to reduce off-target release of drugs. Most cancer drugs have severe side effects.[25–28] The goal of this research is to develop a method of delivering metabolically required innocuous metal ions into cells at high enough concentrations to disturb the function of specific enzymes or proteins or to destroy vital concentration gradients existing within cells and induce apoptosis. The metal ions should not be harmful to other cells even when released into the blood stream and diluted after cell death. Specifically, delivering concentrated calcium ions into diseased cells would stimulate the apoptotic cycle, and cell death would occur without any adverse side effects on healthy cells.[29] This treatment could be an alternative to using traditional, more hazardous and costly chemotherapy drugs.

Calcium ions are essential to biological systems. Calcium storage is normally highly regulated inside cells and the concentration in the cytosol is kept at a low level.[30] However, a large abundance of calcium in the cell cytoplasm induces a positive feedback loop that ultimately results in cell apoptosis.[29,31] The challenge is how to carry Ca^{2+} into cells and release it there. It is too small to be trapped by most of the existing stimuli-responsive gating mechanisms. In prior work we developed a gating mechanism we called a “swinging gate” that was comprised of flexible chelating ligands attached to a

pore surface.[32] In the presence of a metal ion, two of the ligands bind the metal; when this chelation occurred over a pore opening the binding resulted in "latching closed" the gate and preventing organic drug molecules from escaping. Acidification decreased the binding constant, unlatched the gate and resulted in drug release. The simultaneous release of the metal ion was considered a byproduct of the desired release of the drug cargo.

In this paper, we demonstrate that the decrease in pH from that of blood (pH 7.4) to that inside a lysosome after endocytosis of the particle (pH < 7) is able to operate the system,[33] and that particles designed to carry a large amount of Ca^{2+} efficiently induce apoptosis in cancer cells at very low particle concentrations. We make use of the calcium ion that latches the gate to induce apoptosis without using a toxic cargo (figure 2.6.1).

2.3 Results and discussions

2.3.1. Synthesis of nanoparticles with gates latched by calcium ions

Iminodiacetic acid (IDA) has chelating properties similar to those of one-half of an ethylenediaminetetraacetic acid (EDTA) molecule (figure 2.6.1).[34] When IDA is attached to silica with a flexible linker, two neighboring IDA molecules can bind strongly to a metal ion. The calculated size of the fully stretched calcium cross-linked IDA is about 1.8 nm.[32] It is probable that multiple IDA molecules are attached around the pore entrances; there are at least six available silanols around a perfectly shaped pore and likely more around a roughened pore entrance. One IDA cannot perfectly cover the exact center of a pore, but one or more located over the pore entrance can easily block cargos. The IDA binding constant with various metal centers exhibits a ~10^3 fold decrease upon

changing the pH from neutral to 5 as a result of protonation of the carboxylate chelating groups.[35] This property is the basis for the mechanism of operation of the pH responsive IDA nanovalves. A wide variety of metal ions can be used; in this paper Ca^{2+} is chosen because it is a nutritional requirement at normal physiological concentrations but is toxic to cells at high intracellular concentrations. It has a binding constant to IDA on the order of 10^2 and can be released when the ligand is protonated at ~pH 4-6.

The MCM-41 MSNs necessary for the calcium delivery platform were synthesized according to published methods.[32] In a typical synthesis of the 100 nm MCM-41 MSNs, the base catalyzed sol-gel synthesis was conducted at pH 12 and 80 °C. As shown in figure 2.6.9a and b, the average size of the MSNs as measured from TEM images was between 90-110 nm and thus in the desired size range for biomedical applications. The pore size was estimated to be about 2 nm. In figure 2.6.9c, the hexagonal arrangement of pores in the MSNs, which can be seen in the TEM images, was also confirmed by small angel X-ray scattering. The data show the typical 2D hexagonal (p6mm) pattern of MCM-41. The reflections can be indexed as the (100), (110), (200) and (210) planes. The d-spacing is 4.2 nm.

In order to modify the MSNs surface with IDA, the first step is to synthesize (diethyl iminodiacetate)-trimethylsilane via the nucleophilic substitution. The second step is to modify the MSNs surface with the (diethyl iminodiacetate)-trimethylsilane from first step. The third step is to convert the ester groups on (diethyl iminodiacetate)-trimethylsilane to carboxylic acid groups. The final iminodiacetic acid modified MSNs (IDA-MSNs) were made. The scheme is shown in figure 2.6.2.

The successful surface modification of MSNs with IDA groups was confirmed by

FT-IR as shown in figure 2.6.10. Noticeable in the spectrum of the MSNs with (diethyl iminodiacetate)propyl-moiety (blue line) are the aliphatic C-H stretching vibrations of the ethyl ester groups at 2978 and 2937 cm^{-1}, and the C=O stretching vibration at 1732 cm^{-1}. The disappearance of the aliphatic C-H stretching vibrations in the spectrum of the IDA-functionalized particles (pink line) and the remaining of the C=O stretching vibration indicate a successful conversion of the ester groups to free carboxylic acids. The successful functionalization was further supported by solid state ^{13}C-{^{1}H}-CP-MAS-NMR. The spectrum is shown in figure 2.6.11. The carbonyl peak appears at 168 ppm, the corresponding α-carbon peak at 46 ppm and the aliphatic carbons between -3 and 50 ppm.

To optimize the IDA surface coating of the particles and therefore the amount of calcium ions that can be loaded on the particles, two functionalization syntheses were explored. The first procedure utilizes the functionalization pathway was discussed above. The second functionalization procedure involved first modifying the surface of the MSN with the linker 3-iodopropyltrimethoxysilane, and then attaching by nucleophilic substitution dimethyl iminodiacetate as shown in figure 2.6.12. The idea was to minimize polymerization of the (diethyl iminodiacetate)-propylsilane, and thus increase the grafting efficiency. As will be discussed in the following section, the first procedure produced particles that bound the largest amount of calcium ions, and these particles were used in all of the following studies.

2.3.2. Binding and release of calcium ions and Hoechst dye molecules

In order to test the capability of IDA-MSNs to carry Ca^{2+}, the IDA-MSNs were suspended in a $CaCl_2$ solution overnight. After the calcium ions were chelated, the loaded IDA-MSNs were collected by centrifugation and washed with water several times to make sure that the adsorbed Ca^{2+} was washed off as shown in figure 2.6.13. The particles were suspended in pH 5 HCl solution overnight to release all of the Ca^{2+} and the amount released was measured by ICP-OES. The nanoparticles synthesized via the first functionalization pathway had an average release capacity of 0.42 μmol/mg of particles with a maximum in one of the batches of 0.54 μmol/mg of particles (Table S1). Nanoparticles that were synthesized via the second pathway had a much smaller average release capacity of 0.17 μmol/mg of particles. The former particles were chosen for all of the following studies.

2.3.3. Calcium latched Hoechst loaded IDA-MSNs

To confirm that the IDA groups on the MSNs' surfaces coordinated to calcium can trap and release cargo molecules from the pores, the IDA-MSNs were loaded with Hoechst 33342, a dye commonly used as a nuclear stain in cells that was chosen as the probe for its ease of detection by fluorescence spectroscopy. After suspending IDA-MSNs in a concentrated solution of the dye overnight to allow the dye to diffuse into the pores, the Hoechst loaded IDA-MSNs were latched shut by adding the calcium ions. Introducing the Ca^{2+} ion latches the nanogates together by bringing two IDA units together (figure 2.6.3). After the pores of MSNs were shut, the excess dye molecules adsorbed on the MSNs surfaces and excess calcium ions were washed away with fresh doubly distilled water until the supernatant no longer exhibited any fluorescence.

In order to monitor the functioning of the IDA nanogates, a real-time release profile of Hoechst dye from Ca^{2+} ion latched IDA-MSNs was generated. The fully assembled and latched nanoparticles were placed in a corner of a glass cuvette and an excitation beam (377 nm) was used to excite any dye released into the supernatant. The corresponding emission spectrum was collected to generate a time-resolved release profile. As shown in figure 2.6.3, before adding acidic solution into the cuvette no dye was released in the supernatant. However, after acidification to trigger the release, the intensity went up. To verify the calcium latch is necessary to hold back the Hoechst cargo, a control was performed with IDA-MSN loaded with Hoechst but unlatched with calcium ions. However, after subjected to the same washing steps as the calcium latched IDA-MSNs, the Hoechst molecules were washed out. When acidified to pH 5, only a barely noticeable absorbance was observed by UV-vis.

2.3.4. *In vitro* autonomous pH activated release of cargo

To test the autonomous release of cargo by pH of the IDA-MSN, MiaPaCa-2 cells were treated for three hours with a sample of IDA modified MSN loaded with Hoechst 33342 nuclear stain latched with calcium. As shown in figure 2.6.4, the lysosomal pH causes cargo release as illustrated by the blue fluorescent nuclear staining. To verify the calcium latch is necessary to hold back the Hoechst cargo, a control was performed where the cells were treated with IDA-MSN loaded with Hoechst but unlatched. In this sample, no Hoechst nuclear staining was observed because all of the Hoechst cargo had been washed out of the nanoparticle pores during the washing steps (figure 2.6.4b). This indicates that the calcium latch is responsible for successful cargo trapping inside the

MSN pores. Cells treated with this sample show no fluorescence staining, confirming that the observed fluorescence in figure 2.6.4a is due to released Hoechst. It is noteworthy to mention that signs of cellular apoptosis were present in the cells treated with calcium latched IDA-MSN. In this Hoechst stained sample, bright, condensed fluorescence was observed in a number of the treated cells (figure 2.6.4a), signifying collapsed nuclei and indicating the progression of cell death through an apoptotic mechanism.

2.3.5. Inhibition of lysosomal acidification and suppression of cargo release

The pH-activated mechanism of release was further corroborated by testing for cargo release after inhibiting acidification of the cells' lysosomes. MiaPaCa-2 cells were stained with acridine orange, a pH indicating dye, before treated with bafilomycin A1 to neutralize the lysosomes. In figure 2.6.5, the neutral cellular components of cells stained with acridine orange appear with green fluorescence (figure 2.6.5b), while the acidic lysosomal compartments appear orange/red under confocal microscopy (figure 2.6.5a). Once treated with bafilomycin A, the cells appear uniformly with green fluorescence (figure 2.6.5b), indicating that the acidification of lysosomes has been inhibited. Dosing the pH neutralized cells with IDA-MSN loaded with Hoechst and latched with calcium resulted in very little nuclear staining (figure 2.6.5d). Dosing a control group of cells not treated with bafilomycin with the same group of IDA-MSN resulted in Hoechst nuclear staining (figure 2.6.5c). These experiments indicated that the inhibition of acidification of the cell lysosomes blocked the release of Hoechst, and that the cell lysosomal compartments must be acidic in order to autonomously release cargo from loaded IDA-MSN, in agreement with our solution study result.

2.3.6. Apoptosis induced by intracellular calcium ion release

A large abundance of calcium delivered by IDA-MSNs into the cell cytoplasm induces a positive feedback loop that ultimately results in cell apoptosis (figure 2.6.6).[29] The release of calcium into the cytoplasm causes mitochondrial release of cytochrome C. Upon finding its way to the endoplasmic reticulum (ER) where the majority of intracellular calcium is stored, binding of cytochrome C with receptors on the ER causes endoplasmic release of calcium, resulting in additional cytochrome C release from the mitochondria. This positive feedback loop results in toxic concentrations of cytoplasmic calcium, ultimately causing the formation of an apoptosome and cell death.

The cell viability assay was conducted using a cell counting kit. Cells were seeded in 96-well plates and incubated in fresh culture medium. The cells were then washed with PBS and the medium was changed to a fresh medium containing Hoechest loaded, calcium latched IDA-MSN or a control (IDA modified MSN) or a second control (IDS MSN loaded with Hoechst but unlatched) at the indicated concentrations. After twenty-four hours the cells were washed with PBS to remove nanoparticles that were not taken up by the cells, and the cells were incubated in fresh medium for an additional forty-eight hours. The cells were then washed with PBS and incubated in DMEM for another two hours. The absorbance of each well was measured at 450 nm with a plate reader.

While control samples of unlatched Hoechst 33342-loaded IDA-MSN and plain IDA-MSN showed no toxicity within the tested dosage range, a sample of Hoechst-loaded, calcium-latched IDA-MSNs demonstrated a high amount of dose-dependent cell killing (figure 2.6.7). Exclusion of calcium from the control samples resulted in no cell toxicity, suggesting that the observed cell killing is due to a controlled delivery and

release of calcium into the cytosol. It is important to note that the chelating properties of unloaded IDA-MSNs do not cause cell toxicity even at high dosages (100 μg/mL), making this design a viable option for pharmaceutical applications.

2.3.7. Verification of apoptosis

The cells treated with calcium latched IDA-MSN above were examined for apoptosis by two methods: nuclear double staining with propidium iodide and Hoechst 33342 solution, and western blot for cleaved caspase-3 expression. For the first method, the cells were stained with propidium iodide/Hoechst 33342 (1:1) for 5 min and then examined by fluorescence microscopy. As shown in figure 2.6.8a, nuclear fragmentation and chromatin condensation were observed in the cells treated with calcium latched IDA-MSN. For the western blot assay, proteins collected from cell lysates were separated by gel electrophoresis on a polyacrylamide gel containing SDS and then transferred to nitrocellulose membranes. The membranes were probed with caspase-3 antibody as well as with cleaved caspase-3 antibody. As can be seen in figure 2.6.8b, appearance of cleaved caspase-3 band was detected after the treatment with calcium latched IDA-MSN.

2.4. Summary

IDA-modified MSNs were engineered and used to deliver both calcium and Hoechst 33342 nuclear stain to MiaPaCa-2 cancer cells. Treatment of the cells with IDA-MSNs resulted in lysosomal localization of the nanoparticles. The intrinsic low lysosomal pH allows for the autonomous release of both cargo types, as visualized by Hoechst nuclear staining and calcium induced apoptosis. The delivery of calcium to cancer cells

resulted in cancer cell killing at low particle concentrations while control particles that lacked calcium were found to be non-toxic. This design opens the possibility of a safer alternative to using traditional toxic and costly chemotherapy drugs.

2.5. Experimental

2.5.1. Chemicals and characterizations

Tetraethylorthosilicate (TEOS; 99%, Aldrich), cetyltrimethylammonium bromide (CTAB; 98%, Aldrich), Sodium hydroxide (Fisher), absolute ethanol (EtOH; Aldrich), methanol (Aldrich), Hydrochloric acid (Fisher), Dimethyl iminodiacetate (98%, Aldrich), 3-iodopropyltriethoxysilane (Gelest), N,N-diisopropylethylamine (Aldrich), $CaCl_2$ (Aldrich), Tris Buffer (Aldrich), Ca ICP standard (1000ppm, Peak Performance), Hoechst 33342 (2′-(4-Ethoxyphenyl)-5-(4-methyl-1-piperazinyl)-2,5′-bi-1H-benzimidazole trihydrochloride; 98%, Aldrich) were used as received. Anhydrous toluene was obtained by distillation from CaH_2 under dry nitrogen. Moisture-sensitive reactions were carried out under an inert atmosphere of dry nitrogen.

XRD measurements were made using a Panalytical X'Pert Pro powder diffractometer. Solid-state NMR was performed on a Bruker DSX300 spectrometer. TEM images were acquired on a Tecnai T12 microscope. IR measurements were made by using JASCO Fourier Transform Infrared Spectrophotometer. Hoechst release studies were obtained with an in-house time-resolved fluorescence spectroscopy setup. A Coherent 377 nm CUBE laser was used to excite the Hoechst dye, and the subsequent emission spectra were monitored using a Princeton Instruments Roper CCD detector cooled to liquid nitrogen temperatures. ICP-OES measurements were made using ICPE-9000

Shimadzu.

2.5.2. Synthesis of MCM-41 nanoparticles

NaOH solution (2 M, 870 µL, 1.7 mmol) and cetyltrimethylammonium bromide (CTAB, 0.25 g, 0.7 mmol) were mixed with deionized water (120 mL) in a 250 mL round bottom flask equipped with a magnetic stir bar. The temperature was kept constant at 80 °C for 1 hour and the stir rate was 700 RPM. Tetraethyl orthosilicate (TEOS, 1.2 mL, 5.4 mmol) was added dropwise under continuous stirring for 2 hours at 80 °C. The solution color turned from clear to milky white. The solution was cooled down to room temperature and the MSNs were collected by centrifugation (7830 RPM, 15 min). The MSNs were washed with methanol and distilled water until the washings showed a pH of 7. To extract the surfactant, the MSNs (120 mg) were suspended in methanol (75 mL) in a 250 mL round bottom flask and kept at room temperature with sonication and stirring. Concentrated HCl (12 M, 4.2 mL) was added to the suspension and the solution was refluxed for 6 hours. The MSNs were recollected by centrifugation (7830 RPM, 15 min) and washed with methanol and distilled water several times. Complete extraction of CTAB from the pores was confirmed through IR spectroscopy.

2.5.3. Method I synthesis of the (Dimethyl Iminodiacetate)-Propyltriethoxysilane nanogated particles

Dimethyl iminodiacetate (1 mL, 6 mmol), and 3-iodopropyltriethoxysilane (1 mL, 5 mmol) were dissolved in anhydrous toluene (5 mL) in a 50 mL three-necked round bottom flask equipped with a reflux condenser, N_2 gas inlet, an outlet for gas, and

magnetic stir bar. Anhydrous toluene was prepared under N_2 and refluxed with CaH_2 for two to three hours. Catalytic amounts of N,N-diisopropylethylamine (30 µL) were added and the mixture allowed to react under dry N_2 overnight at reflux. In order to push the reaction to complete, the mole ratio of dimethyl iminodiacetate and 3-iodopropyltriethoxysilane needed to be more than 1:1.

In a 50 mL round bottom flask, 50 mg of MSNs that were washed with anhydrous toluene (2 x 10 mL) were suspended in anhydrous toluene dried over calcium hydride (10 mL). The as-synthesized (dimethyl iminodiacetate)-propyltriethoxysilane was added to the MSN suspension and heated overnight at reflux temperature. The functionalized particles were collected by centrifugation (7830 RPM, 10 min) and washed with toluene (2 x 10 mL) and methanol (2 x 10 mL).

To hydrolyze the ester to form the desired iminodiacetic acid modified nanoparticles (IDA-MSN), the dimethyl iminodiacetate modified silica nanoparticles (50 mg) were suspended in doubly distilled water (50 mL) followed by slow addition of concentrated HCl (3 mL) to the reaction mixture. The mixture was allowed to reflux for 6 h. The particles were collected by centrifugation (7830 RPM, 10 min) and washed with methanol and distilled water until the pH of the washings was neutral.

2.5.4. Method II synthesis of the (Dimethyl Iminodiacetate)-Propyltriethoxysilane nanogated particles

For the attempt to increase the surface modification efficiency, the grafting of 3-iodopropyltrimethoxysilane (1 mL, 5 mmol) onto the MSNs was conducted first under dry N_2 at 70 °C for 5.5 h. The idea was to minimize polymerization of the (dimethyl

iminodiacetate)-propylsilane, which is synthesized during the nucleophilic substitution, and thus increase the grafting efficiency. The iodo group-modified MSNs were collected by centrifugation and washed with anhydrous toluene (5 x 10 mL). 3-Iodopropyltrimethoxysilane is sensitive to moisture in the air. If the reaction temperature exceeded 75 °C, the iodo groups degraded and a purple I_2 precipitate was formed. To form the desired product, nucleophilic substitution was conducted. Dimethyl iminodiacetate (1 mL, 6 mmol) and catalytic amounts of N,N-diisopropylethylamine (30 µL) were added to a suspension the modified MSN suspension in anhydrous toluene. The reaction was carried out at 70 °C under dry N_2 for 8 h.

2.5.5. Loading and containment of Hoechst 33342

IDA-MSNs (10 mg) were washed twice with methanol and with doubly distilled water. IDA-MSNs were centrifuged and suspended in a fresh solution of Hoechst 33342 in water (1 mM, 1 mL) and stirred overnight to allow the dye to diffuse into the pores of the particles. The Hoechst 33342 loaded IDA-MSNs were collected by centrifugation.

To close the nanogates on the IDA-MSNPs with Ca^{2+}, the Hoechst 33342-loaded IDA-MSNs were stirred in a buffered $CaCl_2$-solution (300 µL, 160 mg/mL, Tris Buffer pH 8) overnight. The closed IDA-MSNPs were collected by centrifugation (15,000 RPM, 10 min) and washed with doubly distilled water until the washing no longer exhibited fluorescence under UV light.

2.5.6. Measurement of dye release profiles activated by pH change

The release of the Hoechst 33342 dye from the particles was monitored by fluorescence spectroscopy. A solid bolus of particles was placed on one side of the

bottom of a cuvette and a small stir bar placed on the opposite side. The cuvette was slowly and carefully filled with doubly distilled water with minimal disturbance of the particles. The solution was stirred very slowly to distribute any escaped dye molecules throughout the cuvette. A 377 nm diode laser beam (14 mW) was directed through the solution above the sample to excite the dye that diffused out of the pores when the gate was opened. The emission spectrum and intensity of excited Hoechst dye fluorescence were monitored in real time using a monochromator with a CCD detector. A baseline was collected for over 2 hours to monitor any leakage of dye from the particles and any particles that became suspended by the stirring. After a stable baseline was established, a known quantity of dilute HCl was added to decrease the solution pH to 5. The fluorescence intensity as a function of time was plotted to measure the amount of dye released after the nanogate was opened. After complete release (i.e., when the intensity leveled off), the supernatant was collected by centrifugation (7830 RPM, 25 min) and analyzed through UV-Vis to determine weight percent release of Hoechst dye.

2.5.7. Loading and release of calcium ions from IDA-MSNs

To load the IDA-MSNs with Ca^{2+} ions, 10 mg IDA-MSNs were stirred in a buffered $CaCl_2$-solution (300 µL, 160 mg/mL, Tris Buffer pH 8) overnight. To collect the calcium loaded IDA-MSNs, the MSNs were centrifuged down and then washed with 1.5 mL millipore water four times. The collected calcium loaded IDA-MSNs were re-suspended in 1 mL millipore water. To obtain the uptake capacity, the calcium ion concentration of the loading solution before and after centrifugation was converted into the mass and was divided by the mass of MSNs.

The triggered calcium ion release was measured by suspending the calcium

loaded IDA-MSNs in 1.5 mL pH 5 HCl solution overnight. Particles were centrifuged down and the amount of calcium ions in the resulting supernatant was determined by ICP-OES. 1000 ppm Ca standard solution was used to make standard solutions of 0.1 to 50 ppm for making calibration curve.

1 mL of each centrifuged supernatants including after loading and washing steps were diluted 10 times with 2% HNO_3 to make 10 mL solutions for ICP-OES analysis. The release capacity was then defined as the mass of calcium divided by that of MSNs.

2.5.8. Cell culture

Human cancer-cell line MiaPaca-2 was obtained from the American Type Culture Collection and maintained in Dulbecco's modified Eagle's medium (DMEM; GIBCO) or RPMI-1640 medium (Cellgro) supplemented with 10% fetal calf serum (Sigma), 2% l-glutamine, 1% penicillin, and 1% streptomycin stock solutions. The media were changed every three days, and the cells were passaged by trypsinization before confluence.

2.5.9. Fluorescence and confocal microscopy

Cells were cultured overnight on a Lab-Tek chamber slide system (Nalge Nunc International). After the cells were incubated with nanoparticles for 3 hours, they were washed with PBS and examined with via fluorescence microscopy (Carl Zeiss).

2.5.10. Cell death assay

The cytotoxicity assay was performed by using a cell-counting kit from Dojindo Molecular Technologies, Inc. Cells were seeded in 96-well plates (5000 cells/well) and incubated in fresh culture medium at 37 °C in a 5% CO_2/ 95% air atmosphere for 24 h.

The cells were then washed with PBS and the medium was changed to a fresh medium containing Hoechst loaded, calcium latched IDA-MSN, or Control (IDA modified) MSN, or the second control (IDA modified MSN loaded with Hoechst but unlatched) at the indicated concentrations. After 24 h, the cells were washed with PBS to remove nanoparticles that were not taken up by the cells, and the cells were then incubated in fresh medium for an additional 48 h. The cells were washed with PBS and incubated in DMEM with 10% WST-8 solution for another 2 h. The absorbance of each well was measured at 450 nm with a plate reader. Because the absorbance is proportional to the number of viable cells in the medium, the viable cell number was determined by using a previously prepared calibration curve (Dojindo Co.).

2.5.11. Apoptosis assay

Cell death was also examined by using the propidium iodide and Hoechst 33342 double-staining method. The cells were stained with propidium iodide/Hoechst 33342 (1:1) for 5 min and then examined using fluorescence microscopy. For the western blot assay, proteins collected from cell lysates were separated by gel electrophoresis on a polyacrylamide gel containing SDS and then transferred to nitrocellulose membranes. The membranes were blocked with Tris-buffered saline (TBS) containing 5% (w/v) skimmed milk. After being washed with TBS containing 0.1% Tween 20 (Sigma), the membranes were incubated overnight at room temperature with caspase-3 antibody (BD Science) and cleaved caspase-3 antibody (Cellsignaling) diluted with TBS. After being washed, the membranes were incubated for 2 h at room temperature with the second

antibody (Santa Cruz Biotechnology, CA). Bands were detected with an ECL system (Amersham Pharmacia Biotech K.K., UK).

2.6. Figures

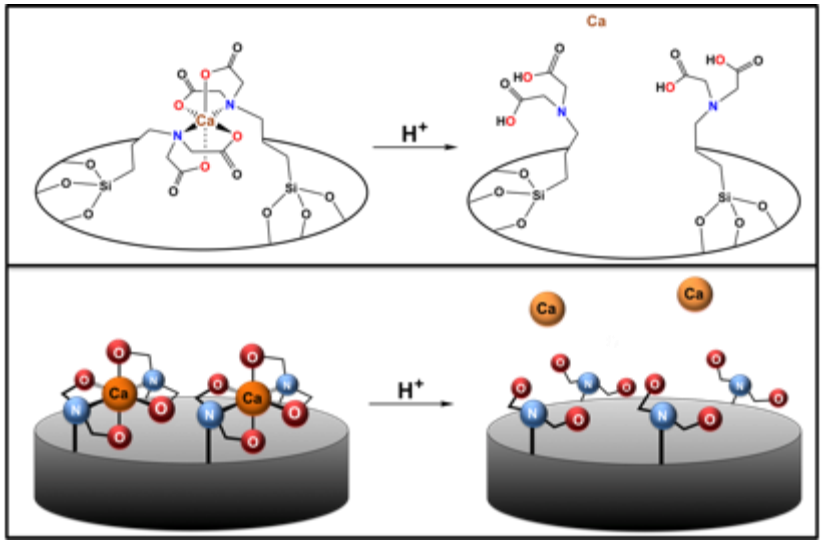

Figure 2.6.1. Top: The chemical structure of the calcium ion chelated by the IDA ligands. The ligands are shown bonded to the surface of the nanoparticles at a pore opening. Protonation of the ligands decreases the binding constant and releases the calcium ion. Bottom: Sketch of the nanogates latched by calcium ions controlling the pore opening.

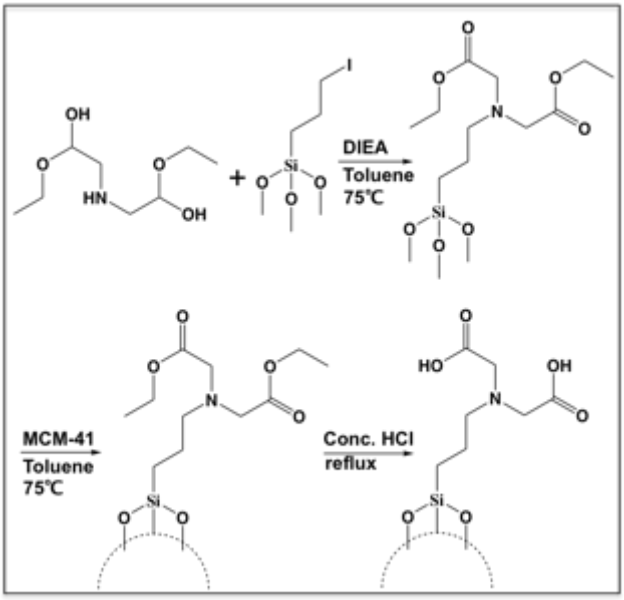

Figure 2.6.2. Chemical reactions for the "method 1" synthesis of the nanogate. First the IDA precursor is bonded to the linker molecule. Then the assembled molecule is bonded to the silica surface and the ester linkages are cleaved to produce the final product. Synthesis in the reverse order ("method 2") results in particles with lower calcium ion carrying capacity.

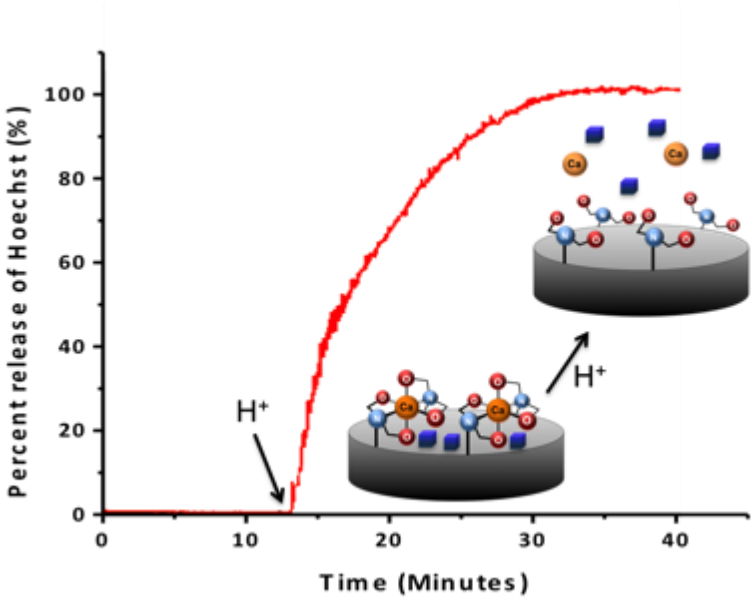

Figure 2.6.3. Release profile of the cargo molecule Hoechst33342 from the gated pores. No leakage occurs at pH 7.4. Upon acidification the gates are unlatched and the cargo molecule diffuses from the pores.

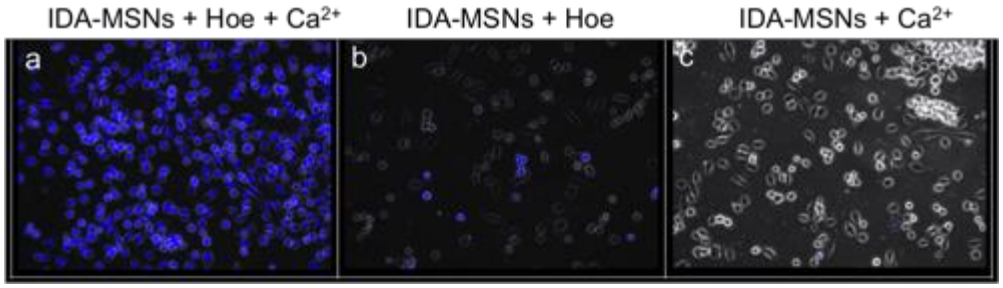

Figure 2.6.4. Hoechst 33342 nuclear staining of MiaPaCa-2 cells. (a) A cell sample treated with Hoechst loaded, calcium latched nanogates showing blue fluorescent staining of cellular nuclei caused by the autonomous release of Hoechst. Nanoparticles are uptaken by endocytosis and localize in the cellular lysosomal compartments. The lower lysosomal pH causes unlatching of calcium and release of the store Hoechst dye. (b) A control sample where the nanomachine was assembled and loaded with Hoechst, but the latching steps with calcium omitted. In this sample, most of the loaded Hoechst dye is removed during the washing steps, therefore, little cellular staining is observed after treatment to cells. (c) A control sample of calcium latched IDA-MSN not loaded with Hoechst to verify the observed blue fluorescence is due to the Hoechst dye.

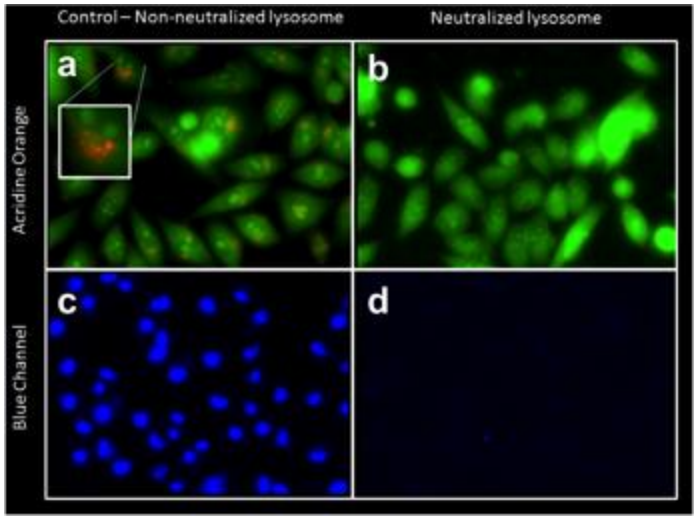

Figure 2.6.5. Fluorescence microscopy images of MiaPaCa-2 cells treated with Hoechst loaded, calcium latched IDA-MSN. The top frames show the outline of cells stained with acridine orange, a pH sensitive dye that fluoresces green at neutral pH, but red/orange at low pH. In the right frames, the acidification of cellular lysosome was inhibited by treatment with bafilomycin A1. In the green channel, the uniform presence of green fluorescence indicates that the lysosomes in this sample are of neutral pH. Subsequent treatment of these cells with Hoechst loaded, calcium latched IDA-MSN resulted in negligible Hoechst nuclear staining, which indicates that a low lysosomal pH is required to unlatch the nanogates and release cargo. In the left frames, a control shows that when the acidification of lysosomes is not inhibited with bafilomycin A1 treatment, Hoechst nuclear staining is observed. This demonstrates that the nanogates are activated by a low lysosomal pH.

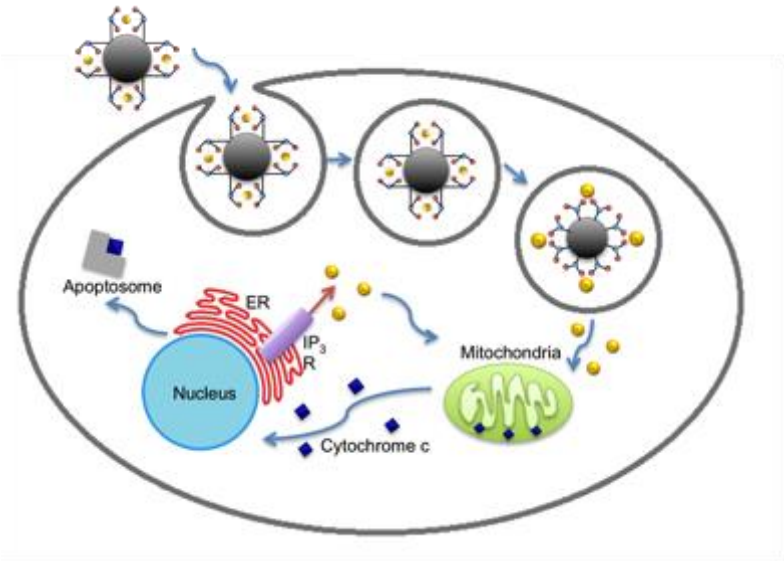

Figure 2.6.6. The role of calcium in orchestrating cellular apoptosis. Release of the death receptor Bid or influx of calcium into the cell cytoplasm causes the mitochondria to release cytochrome c. Some of the released cytochrome C ultimately binds to receptors on the endoplasmic reticulum (ER), causing an outflux of calcium to the cytoplasm. An increased presence of calcium in the cytoplasm causes the mitochondria to release additional cytochrome C, generating a positive feedback loop. Upon calcium concentrations reaching cytotoxic levels, an apoptosome is assembled which leads to cell apoptosis.

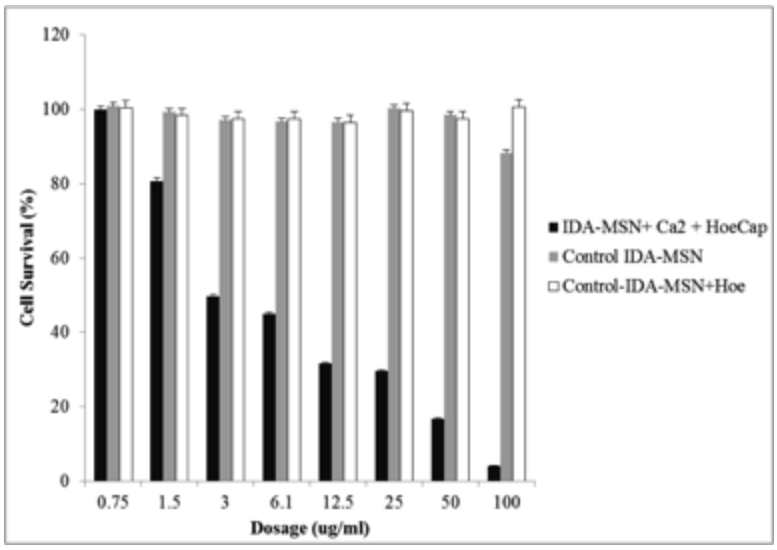

Figure 2.6.7. Cell viability assay of MiaPaCa-2 cells treated with Hoechst loaded, calcium latched IDA-MSN(black bar), Control - IDA modified MSN(grey bar), and Control - IDA modified MSN loaded with Hoechst but unlatched(white bar). Both control samples show no cell killing within the dosage applied. Cell death is only observed when the IDA-MSN is latched with calcium. This suggests that a delivery of calcium causes cell death.

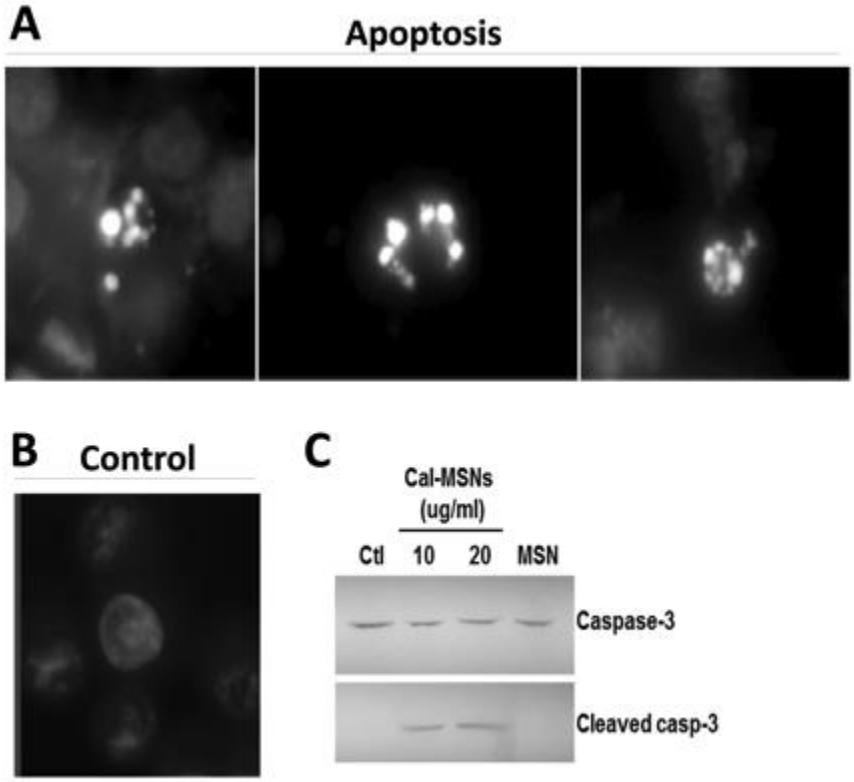

Figure 2.6.8. (A) Apoptosis induced by calcium latched IDA-MSN. MiaPaca-2 cells were incubated for 24 h with calcium latched IDA-MSN and then stained with propidium iodide/Hoechst 33342. (B) The image of the control cells without treatment. (C) Western blotting for caspase 3 expression.

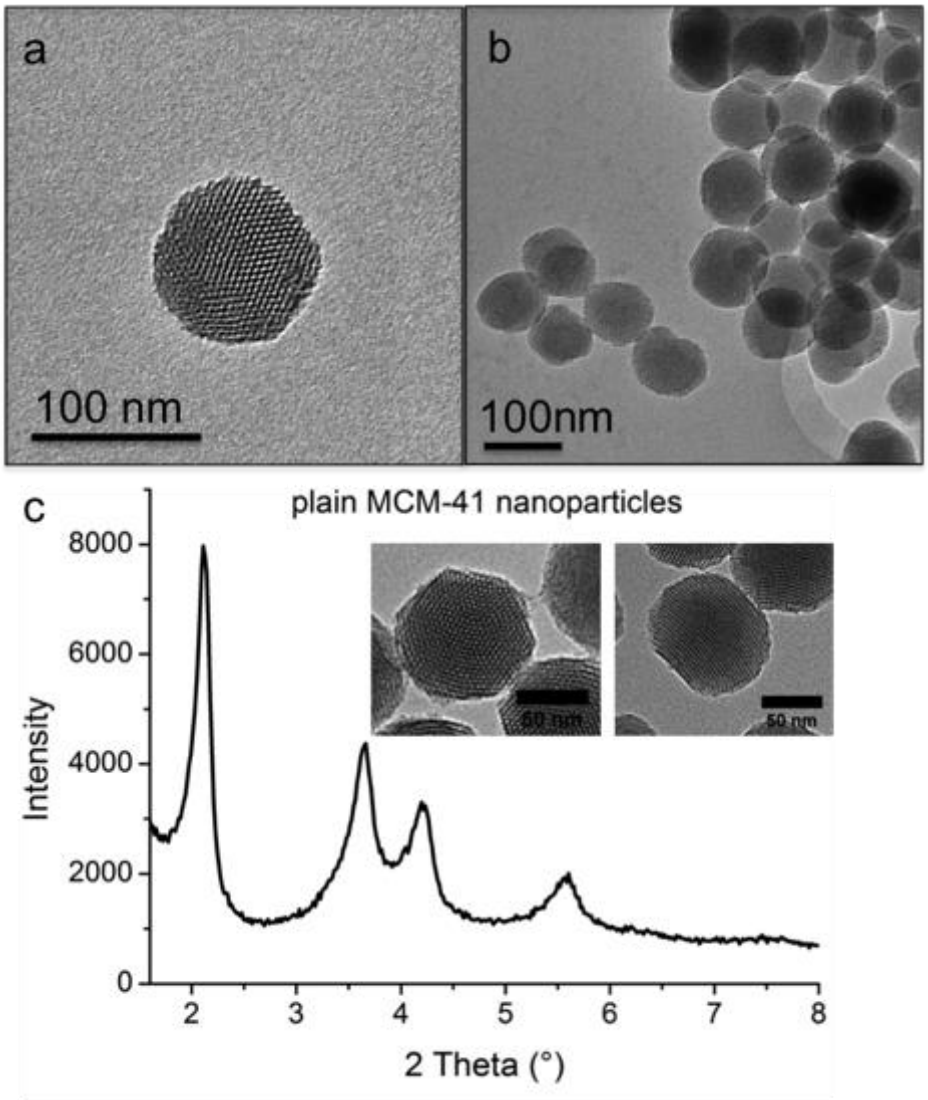

Figure 2.6.9. a. and b. TEM images of MCM-41; c. SAXS diffractogram of plain MCM-41 showing the 2D hexagonal pattern. Inset: TEM images of plain MSNs

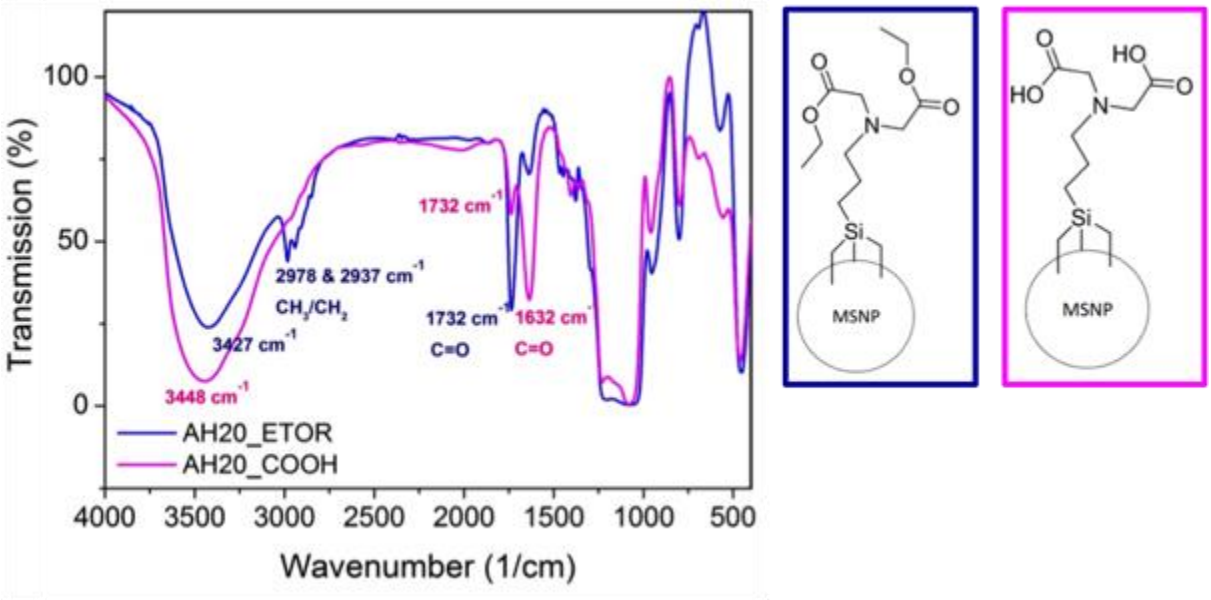

Figure 2.6.10. FT-IR spectroscopy of functionalization process. MSNPs with diethyl iminodiacetate)-propyl moiety (Blue line) and IDA-MSNPs (pink line).

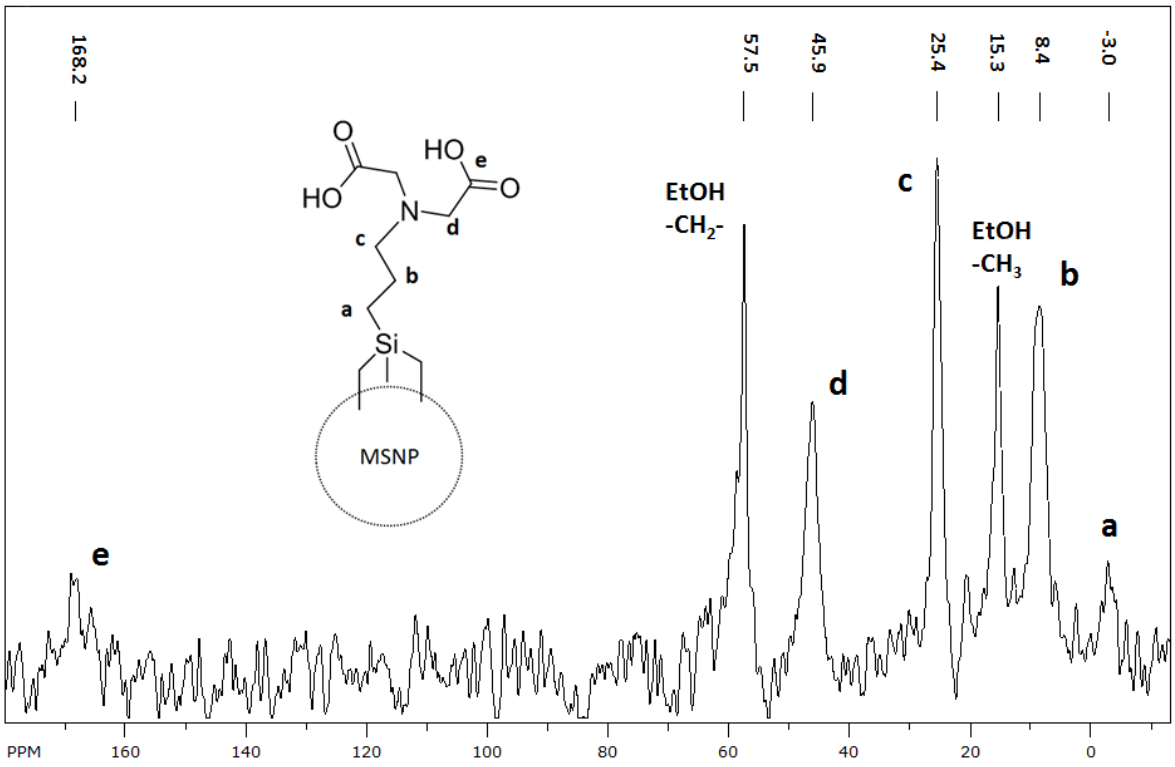

Figure 2.6.11. Solid state ^{13}C-{H}-CP-MAS-NMR spectrum of IDA-MSNPs

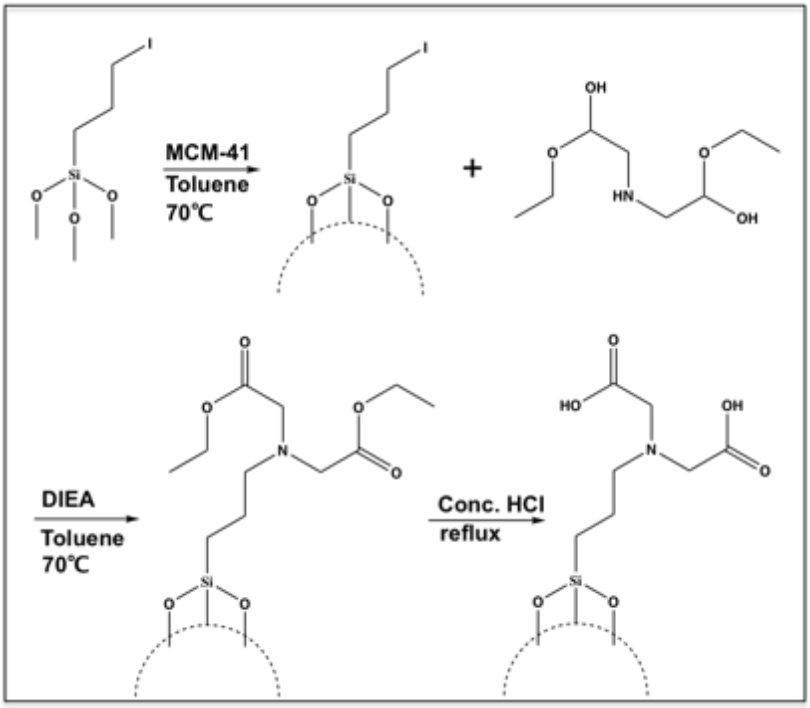

Figure 2.6.12. Chemical reaction of method 2. The linker molecule was first attached on the MSNs followed by the IDA precursor.

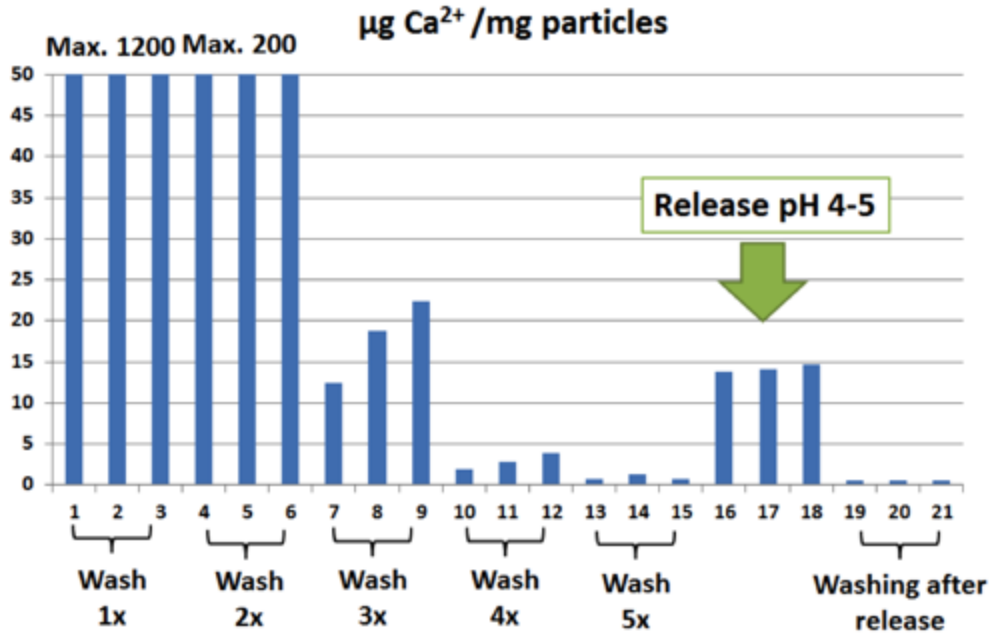

Figure 2.6.13. ICP-OES data of Calcium amount in the washed supernatants and release supernatants. All three trials show that the calcium was washed away completely after five times wash. After lowering the pH, the calcium release was triggered.

2.7 Table

Ca release data from IDA-MSN	µmol Ca2+/mg particle %	Wt% (mg Ca/mg particles)
Batch 1	0.35	1.4
Batch 2	0.46	1.9
Batch 3	0.54	2.2
Batch 4	0.33	1.3
Batch 5	0.12	0.5
Batch 6	0.22	0.9

Table 2.7.1. Batch 1-4, the functionalization was conducted with the nucleophilic substitution first and then grafted the as-synthesized silane onto MSNs. Batch 5-6, the functionalization was to graft 3-Iodopropyltrimethoxysilane onto the MSNs at first, and then the nucleophilic substitution was conducted.

2.8 References

1 Z. Li, J. C. Barnes, A. Bosoy, J. F. Stoddart and J. I. Zink, *Chem. Soc. Rev.*, 2012, **41**, 2590.

2 C. Argyo, V. Weiss, C. Bräuchle and T. Bein, *Chem. Mater.*, 2014, **26**, 435–451.

3 M. Vallet-Regí, F. Balas and D. Arcos, *Angew. Chemie - Int. Ed.*, 2007, **46**, 7548–7558.

4 F. Tang, L. Li and D. Chen, *Adv. Mater.*, 2012, **24**, 1504–1534.

5 Y. Chen, H. Chen and J. Shi, *Adv. Mater.*, 2013, **25**, 3144–3176.

6 B. Ruehle, P. Saint-Cricq and J. I. Zink, *ChemPhysChem*, 2016, **17**, 1769–1779.

7 T. M. Guardado-Alvarez, L. S. Devi, J.-M. Vabre, T. A. Pecorelli, B. J. Schwartz, J.-O. Durand, O. Mongin, M. Blanchard-Desce and J. I. Zink, *Nanoscale*, 2014, **6**, 4652.

8 J. Liu, W. Bu, L. Pan and J. Shi, *Angew. Chemie - Int. Ed.*, 2013, **52**, 4375–4379.

9 P. Saint-Cricq, S. Deshayes, J. I. Zink and A. M. Kasko, *Nanoscale*, 2015, **7**, 13168–13172.

10 A. H. Lu, E. L. Salabas and F. Schüth, *Angew. Chemie - Int. Ed.*, 2007, **46**, 1222–1244.

11 B. Rühle, S. Datz, C. Argyo, T. Bein and J. I. Zink, *Chem. Commun.*, 2016, **52**, 1843–1846.

12 J. L. Paris, M. V. Cabanas, M. Manzano and M. Vallet-Regí, *ACS Nano*, 2015, **9**, 11023–11033.

13 M. Xue, X. Zhong, Z. Shaposhnik, Y. Qu, F. Tamanoi, X. Duan and J. I. Zink, *J. Am. Chem. Soc.*, 2011, **133**, 8798–801.

14 H.-Y. Chiu, W. Deng, H. Engelke, J. Helma, H. Leonhardt and T. Bein, *Sci. Rep.*, 2016, **6**, 25019.

15 F. Yu, X. Tang and M. Pei, *Microporous Mesoporous Mater.*, 2013, **173**, 64–69.

16 J. Sun, C. Hong and C. Pan, *J. Phys. Chem. C*, 2010, **114**, 12481–12486.

17 B. Y. Lee, Z. Li, D. L. Clemens, B. J. Dillon, A. A. Hwang, J. I. Zink and M. A. Horwitz, *Small*, 2016, **12**, 3690–3702.

18 T. M. Guardado-alvarez, L. S. Devi, M. M. Russell, B. J. Schwartz and I. Zink, *J Am Chem Soc*, 2013, **135**, 14000–14003.

19 M. W. Ambrogio, T. A. Pecorelli, K. Patel, N. M. Khashab, A. Trabolsi, H. A. Khatib, Y. Y. Botros, J. I. Zink and J. F. Stoddart, *Org. Lett*, 2010, **12**, 3363–3366.

20 A. Popat, S. B. Hartono, F. Stahr, J. Liu, S. Z. Qiao and G. Qing (Max) Lu, *Nanoscale*, 2011, **3**, 2801.

21 C. Hu, P. Huang, Z. Zheng, Z. Yang and X. Wang, *Langmuir*, 2017, **33**, 5511–5518.

22 J. Liu, B. Zhang, Z. Luo, X. Ding, J. Li, L. Dai, J. Zhou, X. Zhao, J. Ye and K. Cai, *Nanoscale*, 2015, **7**, 3614–3626.

23 B. Ruehle, D. L. Clemens, B.-Y. Lee, M. A. Horwitz and J. I. Zink, *J Am Chem Soc*, 2017, **139**, 6663–6668.

24 S. H. van Rijt, D. a. Bölükbas, C. Argyo, S. Datz, M. Lindner, O. Eickelberg, M. Königshoff, T. Bein and S. Meiners, *ACS Nano*, 2015, **9**, 2377–2389.

25 N. Pabla and Z. Dong, *Kidney Int.*, 2008, **73**, 994–1007.

26 S. Miura, M. Maemondo, A. Iwashima, T. Harada, S. Sugawara, K. Kobayashi, A. Inoue, T. Nakagawa, Y. Takiguchi, H. Watanabe, T. Ishida, M. Terada, H. Kagamu,

A. Gemma and H. Yoshizawa, *Invest. New Drugs*, 2017, **35**, 227–234.

27 D. Schmid, G. E. Jarvis, F. Fay, D. M. Small, M. K. Greene, J. Majkut, S. Spence, K. M. McLaughlin, K. D. McCloskey, P. G. Johnston, A. Kissenpfennig, D. B. Longley and C. J. Scott, *Cell Death Dis.*, 2014, **5**, e1454.

28 K. Chatterjee, J. Zhang, N. Honbo and J. S. Karliner, *Cardiology*, 2010, **115**, 155–162.

29 M. P. Mattson and S. L. Chan, *Nat. Cell Biol.*, 2003, **5**, 1041–1043.

30 S. Orrenius, B. Zhivotovsky and P. Nicotera, *Nat. Rev. Mol. Cell Biol.*, 2003, **4**, 552–565.

31 P. Pinton, *Oncogene*, 2010, **27**, 6407–6418.

32 D. Tarn, M. Xue and J. I. Zink, *Inorg. Chem.*, 2013, **52**, 2044–2049.

33 C. C. Scott and J. Gruenberg, *BioEssays*, 2011, **33**, 103–110.

34 S. Chaberek Jr. and A. E. Martell, *J. Am. Chem. Soc.*, 1952, **74**, 5052–5056.

35 H. Irving and D. H. Mellor, *J Chem Soc*, 1962, **0**, 5222–5237.

Chapter 3

Enhanced Fenton Reaction for Reactive Oxygen Species Generation by Iron Ion-Loaded Mesoporous Silica Nanoparticles for Cancer Therapy

3.1 Abstract

Reactive oxygen species (ROS)-induced apoptosis is a widely practiced strategy for cancer therapy. Through the Fenton reaction, H_2O_2 could be catalyzed by iron ions to the ROS such as hydroxyl radicals (·OH), which cause oxidative damages to lipids, proteins, and DNA. By utilizing Fenton chemistry, we herein demonstrated triggering ROS generation by delivering iron ions through iron ion-loaded mesoporous silica nanoparticles (MSNs) to induce the Fenton reaction in the tumors, by taking advantage of the mild acidity (pH 4.5-5) and the overproduced H_2O_2 in a tumor microenvironment. By delivering non-toxic iron ions for enhanced Fenton reaction, we achieved anticancer activity but minimized systemic toxicity.

3.2. Introduction

Ferroptosis is an emerging strategy of cancer therapy which utilizes triggering a Fenton reaction, in which excess reactive oxygen species (ROS) are produced in tumor cells to induce cell death.[1–3] Iron ions (Fe^{2+}, Fe^{3+}) are known to be responsible for the Fenton reaction - iron ions reacting with hydrogen peroxide in the cells to create hydroxyl radicals.[4] However, such redox activity can generate free radicals and other strongly oxidizing species capable of causing a wide range of biological injury.[2] This can occur through a variety of mechanisms, such as lipid bilayer oxidation or DNA damage. One study showed that cancer cells and tissues, or bacteria-infected cells produce large amounts of hydrogen peroxide,[5] which is obtained from mitochondria-generated superoxide ions in a process that is catalyzed by the overexpressed superoxide dismutase. By utilizing the naturally high concentration of H_2O_2 in tumor cells, the technique of triggering the Fenton reaction to kill cancer cells or bacteria has been reported.[6–8]

Fenton reaction:[4]

$$Fe^{2+} + H_2O_2 \rightarrow Fe^{3+} + \cdot OH + OH^- \qquad (1)$$

$$Fe^{3+} + H_2O_2 \rightarrow Fe^{2+} + \cdot OOH + H^+ \qquad (2)$$

Much research has been conducted on how to trigger Fenton reactions in tumors to act as cancer therapies, such as small molecule drugs (Sorafenib,[9] sulfasalazine[10]) and Ferroptosis-inducing nanomaterials (ex: iron oxide nanoparticles).[11–14] The small molecules for ferroptosis-based cancer therapy have many advantages, such as long shelf life and low long-term toxicity (they are easily metabolized or cleared from the body). However, there are also some limitations for small molecules, such as no targeting properties (causing Fenton reactions in normal tissues and cells), short half-life in

circulating blood, and low accumulation at tumor sites due to rapid renal clearance.[1]

In order to overcome the disadvantages of small molecules for Ferroptosis-based cancer therapy, Ferroptosis nanomaterials have been introduced, including iron oxide nanoparticles and FePt nanoparticles.[6,13] The advantages of nanomaterials for ferroptosis-based cancer therapy are numerous. They possess precise targetability, such as passive targeting (through enhanced permeability and retention (EPR) effect)[15,16] and active targeting (through surface functionalization of targeting agents).[17,18] Also, the nanomaterials can reduce renal clearance, prolong the half-life in circulating blood, and enhance accumulation at tumor sites through PEI/PEG coating.[19]

Here we demonstrated that delivering large amounts of iron ions into cancer cells can cause cell death. Iron ions are not only responsible for the Fenton reaction, but are also essential to biology systems and exist in enzymes and proteins.[20] Delivered iron ions are released and diluted in the system after cell death, so they are not as harmful as traditional cancer drugs. By replacing toxic cancer drugs with iron ions, we propose a safer cancer therapy alternative. To the best of our knowledge, we are the first group to report on delivering iron ions through mesoporous silica nanoparticles to induce the Fenton reaction in cancer cells.

Making a drug delivery platform suitable for metal ions poses several challenges. First, it is necessary to consider the platform used to hold the payload that later is to be released specifically in the tumor cells, especially for the small size of metal ions. Here, we chose mesoporous silica nanoparticles (MSNs) as the carriers, due to their large internal pore volume and surface area, pore size, morphology, and huge flexibility for chemical modifications.[21–23] Second, in order to load the iron ions and release them in the

tumor cells, we chose the iminodiacetic acid (IDA) as the chelator modified onto the MSN surface and bound to the iron ions. The IDA's binding constant decreases ~10^3 when pH drops from 7 to 4, which is the essential working mechanism;[24,25] the iron ions have to be bound on the MSNs at pH 7-7.4 (the body's pH) and released in the lysosomes in tumor cells (pH4.5-5).[26]

3.3. Results and discussions

3.3.1. Synthesis of silica mesoporous nanoparticles and surface modification with IDA

The iminodiacetic acid can act as a tridentate ligand to form a metal complex with two, fused, five membered chelate rings at high pH (above pH 9). It can also act as a bidentate ligand through its two carboxylate groups around pH 4-9 since the nitrogen is protonated. Two close-by IDAs can act as an Ethylenediaminetetraacetic acid (EDTA) molecule, which is well known for chelation property with many metal ions (Cu, Co, Ca, Mn, Fe, et al.)[26] From our previous work, the IDA binding constant with Calcium ions exhibits a ~10^3 fold decrease upon changing the pH from neutral to 5 as a result of protonation of one of the carboxylate chelating groups.[27] This property enables the controllable release mechanism of metal ions in the cells. In tumor cell, the lysosome pH can be as low as 4.5 where the metal ions will be released and most of the body remains pH 7-7.4 where the metal ions are chelated with IDA groups.[28] The stability constant of $Fe(II)(IDA)_2$ is 5.8. The pKa of IDA pKa for amino groups: 8.15-9.7; for the 2 carboxylate groups: 2.37-3.45

The MCM-41 MSNs delivery platform for iron ions were synthesized from the published methods.[27,29] In a typical synthesis of the 100 nm MCM-41 MSNs, the base catalyzed sol-gel synthesis was conducted at pH 12 and 80 °C. As shown in figure 3.6.2A, the average size of the MSNs as measured from TEM images was between 120-150 nm and thus in the desired size range for biomedical applications. From figure 3.6.6, the N_2 adsorption-desorption isotherm analysis shows that the MCM-41 nanoparticles have a pore size diameter around 2.8 nm as calculated according to the BJH method based on the adsorption branch of the isotherms and the IDA-MSNs have a pore size diameter around 2.4 nm. BET surface area was calculated over the range of partial pressure between ~0.08–0.23 P/P^0. From BET calculation, the MCM-41 has surface area of 920 m^2/g and the IDA-MSN has that of 780 m^2/g. As expected, post-grafting IDA groups onto the surface of the MCM-41 and the pores decreased the surface area and pore diameter of MCM-41.

The synthesis of final iminodiacetic acid modified MSNs (IDA-MSNs) were made as previous reported method as shown in figure 3.6.1. First, the precursor silane was obtained via nucleophilic substitution reaction between diethyl iminodiacetate and 3-iodopropyltrimethoxysilane. The product silane is (diethyl iminodiacetate)-trimethylsilane. Second, through post-grafting, (diethyl iminodiacetate)-trimethylsilane was grafted onto the MSNs surface. Third, acidic hydrolysis of the ester groups on (diethyl iminodiacetate)-trimethylsilane was performed to form carboxylic acid groups. The step-by-step synthesis of IDA-MSN was confirmed by FTIR as shown in figure 3.6.2B. The black line is the IR data of MCM-41 before acid extraction, which has aliphatic C-H stretching vibrations of the ethyl ester groups at 2849 and 2920 cm^{-1}. The

red line is the MCM-41 after removing CTAB, which shows the disappearance of C-H stretching. The successful post-grafting of IDA groups was also proven. The emerging of the C=O stretching vibration (1640 and 1740 cm^{-1}) indicate a successful post-grafting of carboxylic acids (blue line). From figure 3.6.2C, the TGA analysis of MCM-41 after acid extraction and IDA-MSNs shows that about 8 wt% IDA groups were post-grafted onto the MCM-41 nanoparicles. To further verify the successful surface modification of IDA groups onto MSNs, the ^{13}C NMR and ^{29}Si NMR were conducted shown in figure 3.6.3 and 3.5.4.

The peak assignment for iminodiacetic acid modified MSNs is based on the ^{13}C NMR data from the Spectral Database for Organic Compounds, SDBS. Figure 3.6.5a to 3.6.5c are the solid state ^{13}C NMR data of iminodiacetic acid, (3-aminopropyl) triethoxysilane, and tetraethyl orthosilicate (TEOS). The chemical structure of IDA-MSNs is shown in the figure 3.6.3. Iminodiacetic acid has two carbon peaks at 48 and 170 ppm, as shown in figure 3.6.5a. From the IDA-MSN spectrum, there are peaks at 58 (carbon d) and 170 ppm (carbon e), which agrees with the iminodiacetic acid NMR spectrum. The shift from 48 ppm to 58 ppm could be from three-carbon chain attached to IDA (figure 3.6.3). In order to assign the carbon peaks for the carbon linker connecting IDA on the IDA-MSNs, the ^{13}C NMR of (3-aminopropyl) triethoxysilane (figure 3.6.5b) serves as the reference. The carbon linker between Si and N has three carbon peaks at 7, 27, and 45 ppm from Si to N, which agrees with my IDA-MSN data for carbons a, b, and c. In the IDA-MSN spectrum (figure 3.5.3), the peaks around 20 ppm haven't been assigned between peak a and b. The 20 ppm peak could be the from the un-hydrolyzed ethoxyl groups from TEOS. The NMR spectrum of TEOS is shown in figure 3.6.5c.

TEOS has two carbon peaks at 18 and 59 ppm. The 18 ppm peak in TEOS agrees with the 18-20 ppm peaks in the IDA-MSN spectrum. TEOS has a peak at 59 ppm, which could explain why the 60 ppm peak in IDA-MSN has a shoulder. The conclusion is that the major peaks in the IDA-MSN spectrum have IDA and (3-aminopropyl) triethoxysilane carbon signals. The extra peaks in the IDA-MSN spectrum are from unhydrolyzed ethozyl groups from TEOS.

3.3.2. Binding and release of iron ions

In order to test the capability of IDA-MSNs to carry iron ions, the IDA-MSNs were suspended in a $(NH_4)_2Fe(SO_4)_2 \cdot 6H_2O$ solution overnight for iron ions to chelate to IDA groups. After the iron ions were chelated, the iron ion loaded IDA-MSNs were collected by centrifugation and washed with water several times to make sure that the adsorbed iron ions on the MSN surface was washed off, as shown in figure 3.6.2D. The washing step was processed by mixing fresh Millipore water with the collected iron loaded IDA-MSNs, suspending the IDA-MSNs well, the IDA-MSNs collected by centrifugation, and the supernatant removed. This washing process was carried out four times. The separated supernatants of washing steps were analyzed with ICP-OES. The release step was carried out by suspending the iron loaded IDA-MSNs in pH 5 HNO_3 solution overnight to release all the iron ions from the IDA groups and the amount of released iron ions was measured by ICP-OES. The nanoparticles had an average release capacity of 0.69 μmol/mg of particles with a maximum in one of the batches of 1.29 μmol/mg of particles.

3.3.3. Cell viability study by intracellular iron delivery

Iron ions are essential and highly regulated to maintain normal cell functions. If the iron concentration is disordered in the cells, it can cause cell death, likely from unregulated Fenton reactions. With the IDA modified MCM-41 nanoparticles, delivering small cargoes as metal ions is feasible. Also, with the MCM-41 platform, through EPR effects, a large amount of iron ions can be directly delivered into the cells. The cell viability data is shown in figure 3.6.7. The THP-1 cells were treated with free iron ions, pure IDA-MSNs, and Fe(II)@IDA-MSNs for 72 hours. As figure 3.6.7 shows, only the cell Fe(II)@IDA-MSNs treatment showed a dose-dependent cell killing effect (50% cell viability from 100 μg/mL). Bare IDA-MSNs without iron showed no toxicity within the tested dose range, meaning this nano-carrier is safe to be used in a bio-system. The free iron ions treatment actually showed the dose dependence of cell growth effect, possibly because iron ion is one of the essential nutrition from human cells within a reasonable concentration range. One way-ANOVA was used to see if there were any significant differences between any two data sets, which yielded a p-value $< 10^{-14}$. Student's t-tests were used to compare two data sets' normalized means to each other. The results of this test were $p < 0.05$ for all treatments compared to control, and for all treatments compared to each other.

3.3.4. ROS production through delivered iron ions by MSNs

In order to investigate if the excess iron ions delivered into tumor cells can enhance the Fenton reaction, cell death was triggered via ROS production. ROS production in tumor cells was measured after incubation with the 2,7-dichloro-dihydro-

fluorescein diacetate (H_2DCFHDA) probe for oxidative stress. After diffusing into cells, DCFH-DA is deacetylated by intracellular esterases to the non-fluorescent 2',7'-dichlorofluorescin (DCFH), which can be oxidized to the highly fluorescent 2',7'-dichlorofluorescein (DCF) dye that is proportional to ROS species present. After incubation with the ROS probe, free iron ions, pure IDA-MSN, and Fe(II)@IDA-MSN are added to cells and ROS is measured over time by fluorescence of the DCF dye. As expected, from figure 3.6.8, the pure IDA-MSN doesn't produce excess ROS compared to control. The control is cells treated with H_2DCFHDA but not treatments. When the Fe ions were delivered by MCM-41 through EPR effect, it's expected to be a more efficient way to enter the cells, so the ROS amount is higher than that in the free iron ion treated cells. Compared to the control, the ROS amount the Fe(II)@IDA-MSN and free iron ion treated cells were six and four times higher after 24h treatment, respectively. From the cell viability data (figure 3.6.7), 20% cell growth was observed for the free Fe(II) treatment after 72h; however, the cell viability went down to 60% with Fe(II)@IDA-MSN treatment. As a result, and at the end of 72h, the total cell number was different for free iron ion and Fe(II)@IDA-MSN treatments. Concurrently, total cell count was measured at 72h treatment in order to normalize ROS production by the total number of cells. The reason for this experiment is to demonstrate the helping effect of iron ion on cell growth. To contrast, Fe(II)@IDA-MSN caused cell death. The ROS was produced by all cells, and as a result, the signal from each well needed to be normalized to cell counts, shown in figure 3.6.8B. Relative to the control, the free iron ion caused 8 times ROS signal and Fe(II)@IDA-MSN caused 14 times more. The positive control of ROS assay was also conducted to confirm that the DCF probe was working as shown in figure 3.6.9.

3.3.5. Verification of cell death from Iron and the produced ROS

In order to further understand if the delivered Fe ions from IDA-MSNs cause the cell death, the iron chelator (Deferiprone, DFP) was used to chelate to the iron ions in the cells.[30] The THP-1 cells were first treated with DFP for 24h and then with Fe(II)@IDA-MSNs for 72h. As the figure 3.6.10A shows, the Fe(II)@IDA-MSNs treated cells had 54% viability; however, the DFP treated cells had almost 98% viability. The IDA-MSNs treatment had 88% cell viability. As a result, DFP as a iron chelator successfully saved the cells from the extra iron ions delivered by IDA-MSNs. The second proof that Fe(II)@IDA-MSNs cause cell death was conducted with a radical scavenger N-Acetyl-L-cysteine (NAC).[31] By treating cells with NAC, the ROS produced from the enhanced Fenton reaction can be reduced. From figure 3.6.10B, the IDA-MSNs treatment had 80% cell viability and the Fe(II)@IDA-MSNs had 57% cell viability. The NAC and IDA-MSNs treatment had about 90% cell viability. The cell death of IDA-MSN treatments is likely due to IDA-MSNs (100 μg/mL dose). The NAC treatment successfully reduced the cell death by 40% compared to the Fe(II)@IDA-MSN treatment. In conclusion, DFP as an iron chelator successfully bound to the extra iron ions delivered via IDA-MSNs, and DFP's reduction of cell death proves that Fe ions from IDA-MSNs are responsible for this cell death. The NAC as the radical scavenger, in this case, successfully reduced the amount of ROS from the Fenton reaction triggered by the iron ions delivered via IDA-MSNs.

3.3.6. Verification of necrosis

To further understand how intracellular delivered iron ion with IDA-MSNs caused cell death, cells treated with Fe(II)@IDA-MSNs for 72 hours were stained with propidium iodide (PI) dead cell nuclear stain and Annexin V-Alexa Fluor 488 conjugate (Annexin), a marker of apoptosis. Dual staining for dead cells and apoptotic cells allows us to quantify the percent cell population undergoing apoptosis or necrosis using flow cytommetry. Q1 means necrotic cells; Q2 means late apoptotic cells; Q3 means early apoptotic cells; Q4 means living cells. In order to draw the gating to divide the Q1-Q4 areas, the single stained, double stained non-treated cells were analyzed. The positive apoptosis control was conducted. The THP-1 cells were treated with cisplatin, as cisplatin is known for triggering apoptosis in cells.[32,33] The control (non-treated) cells with single stained of PI and ANNEXIN are also shown in figure 3.6.12 A and B. PI stained cells mean the necrotic cells are shown in Q1 region and the ANNEXIN stained cells mean the apoptotic cells (early stage of apoptosis: Q3; late stage of apoptosis: Q2). The cisplatin treated cells for the dual stained and single stained with ANNEXIN data is shown in figure 3.6.12C and D. From figure 3.6.12C, the cell population distribution is obviously going through apoptosis, because the cells were spreading through Q3 and then Q4 and finally Q1. On the other hand, if the cells were going through necrosis, the cells would spread vertically from Q4 to Q1. As figure 3.6.11 shows, the control cells, free iron ion treated cells, and the IDA-MSNs treated cells have the similar trends of cell population distribution as the cisplatin treated cells (figure 3.6.12C), indicating these treatments would trigger apoptosis. However, the Fe(II)@IDA-MSNs treated cells, which is shown in figure 3.6.11D, have a vertical movement from Q4 to Q1 and very few apoptotic cells 2.89% (late apoptotic and early apoptotic).

The free iron ion treated cells had similar percentages (84.6%) of living cells compared to the control. The difference between free iron ion treated cells and the control is the early apoptotic population, which is 2% higher. The IDA-MSNs treated cells had same trend of the cell population; however, compared to the control and the free iron ion treatments, the population of the necrotic cell increased 12%. This 12% of dead cells was expected, as when the dose of IDA-MSNs was as high as 100 μg/mL, cell death was often observed. The Fe(II)@IDA-MSN treatment showed much higher population of necrotic cells (20.1%) compared to free iron (3.39%) and control (2.53%) treatments, but very few apoptotic cells (2.89%). From how the cells distributed through Q1-Q4 (either from Q4 to Q3 and Q2 and then Q1 or from Q4 to Q1 vertically), and the percentage of cell populations at different stages, the Fe(II)@IDA-MSNs treatment caused a different cell death mechanism than the other three treatments (control, free iron ion, and IDA-MSNs). This experiment proved that the delivered free iron ions by IDA-MSNs caused cell necrosis.

3.4. Summary

IDA-modified MSNs were engineered and used to deliver iron ion to THP-1 cancer cells. Treatment of the cells with Fe(II) loaded IDA-MSNs resulted in lysosomal localization of the nanoparticles. The intrinsically low lysosomal pH allows for the autonomous release of iron ions, so the Fenton reaction was magnified, as proved by ROS assay. The delivery of iron ions to cancer cells resulted in cancer cell death, while control particles that lacked iron ions were found to be non-toxic, and free iron ions resulted in cell growth. This design demonstrates how to trigger Fenton reactions by

delivering non-toxic iron ions to produce a high concentration of hydroxyl radicals to cause cell death. Utilizing the non-harmful metal ions can be a replacement to using traditionally toxic and costly chemotherapy drugs.

3.5. Experimental

3.5.1. Chemicals and Characterizations

Dimethyl iminodiacetate (98%, Aldrich), 3-iodopropyltriethoxysilane (Aldrich), Tetraethylorthosilicate (TEOS; 99%, Aldrich), cetyltrimethylammonium bromide (CTAB; 98%, Aldrich), Sodium hydroxide (1M; Fisher), Hydrochloric acid (Fisher), absolute ethanol (EtOH; Aldrich), methanol (Aldrich), N,N-diisopropylethylamine (Aldrich), Ammonium iron(II) sulfate hexahydrate (99%, Aldrich), Iron(III) nitrate nonahydrate (98.0-101.0%, crystalline, Alfa Aesar), Fe ICP standard (1000ppm, AccuStandard), were used as received. Anhydrous toluene was obtained by distillation from CaH_2 under dry nitrogen. Moisture-sensitive reactions were carried out under an inert atmosphere of dry nitrogen.

IR analyses were made by using JASCO Fourier Transform Infrared Spectrophotometer. ICP-OES measurements were acquired using ICPE-9000 Shimadzu. TEM images were obtained on a Tecnai T12 microscope. Nitrogen adsorption and desorption isotherms were obtained at 77 K using an Autosorb-iQ (Quantachrome Instruments). Thermogravimetric analysis (TGA) was performed using a Perkin-Elmer Pyris Diamond TG/DTA under air. Approximately 10-12 mg of sample was loaded into aluminum pans. The UV-vis spectra were acquired from Carry 5000 UV-vis-NIR spectrophotometer. The ^{13}C solid state NMR experiment and ^{29}Si solid state NMR were

performed with a *DSX300*.

3.5.2. Synthesis of MCM-41 Nanoparticles

In a 250 mL round bottom flask equipped with a magnetic stir bar, the NaOH solution (1 M, 1.75 mL, 1.7 mmol), cetyltrimethylammonium bromide (CTAB, 0.25 g, 0.7 mmol), and deionized water (118 mL) were mixed. The temperature was heated to and kept constantly at 80 °C for 1 hour with vigorous stirring. Tetraethyl orthosilicate (TEOS, 1.2 mL, 5.4 mmol) was added dropwise (1 drop/1second) and then 0.79 mL Ethyl Acetate was added under continuous stirring and then the mixture was mixed for 2 hours at 80 °C. The solution color turned from clear to milky white. The solution was cooled down to room temperature and added methanol (MSN solution: methanol= 10 mL: 30 mL) and the MSNs were collected by centrifugation (7830 RPM, 15 min). The MSNs were washed with methanol 4-5 times and kept in methanol. To extract the surfactant (CTAB), the MSNs (200 mg) were suspended in methanol (60 mL) and then the concentrated HCl (12 M, 2.4 mL) was added to the suspension in a 250 mL round bottom flask. The mixure was refluxed for 6 hours under stirring. The MSNs were recollected by centrifugation (7830 RPM, 15 min) and washed with methanol and distilled water several times. Complete extraction of CTAB from the pores was confirmed through IR spectroscopy.

3.5.3. Synthesis of the (Dimethyl Iminodiacetate)-Propyltriethoxysilane modified MSNs

The synthesis scheme is shown in figure 3.6.1. First, the linker of (dimethyl

Iminodiacetate)-propyltriethoxysilane is synthesized by mixing (8 mmol) diethyl iminodiacetate, 1.2 mL 3-iodopropyltrimethoxysilane (6 mmol) and 100 µL *N,N*-diisopropylethylamine (DIEA, 0.6 mmol) in 10-15 mL anhydrous toluene at 75 °C and stirred under a dry N_2-atmosphere for 5 h at 75 °C. Second, for the grafting of the synthesized (diethyl iminodiacetate)-propyltrimethoxysilane on the MCM-41 MSNs, the 100 mg of after extracted CTAB MSNs were first washed twice with toluene and suspended in 20 mL anhydrous toluene. Then they were added to the reaction mixture and stirred overnight under dry N_2 at 75 °C. The functionalized particles were collected through centrifugation (7830 rpm, 15 min) and washed with Methanol (3x, 30 mL) and distilled water (3x, 30 mL).

3.5.4. Synthesis of Iminodiacetic Acid Modified Nanoparticles (IDA-MSNs)

The diethyl iminodiacetate modified MSNs were suspended in 20 mL water and then 20 mL concentrated HCl was added under stirring. The mixture was refluxed for 4 h. The IDA-MSNs were collected through centrifugation (7830 rpm, 15 min) and washed with ethanol (3x, 30 mL). The particles were stored in EtOH.

3.5.5. Loading and release of Fe(II) ions from IDA-MSNs

For the loading of the IDA-MSNs with Fe^{2+} ions, ammonium iron (II) sulfate hexahydrate (250 mg) was dissolved in 1 mL Millipore water. The prepared Fe^{2+} solution was added into 10 mg IDA-MSNs and stirred overnight. To collect the iron loaded IDA-MSNs, the MSNs were centrifuged down and then washed with 1 mL millipore water four times. The collected iron loaded IDA-MSNs were re-suspended in 1mL millipore

water. To obtain the uptake capacity, the iron ion concentration of the loading solution before and after centrifugation was converted into the mass and was divided by the mass of MSNs.

The triggered iron ion release was measured by suspending the iron loaded IDA-MSNs in 1 mL pH 5 HNO_3 solution overnight. Particles were centrifuged down and the amount of iron ions in the resulting supernatant was determined by ICP-OES. 100 ppm Fe standard solution was used to make standard solutions of 0.1 to 10 ppm for making calibration curve. The centrifuged supernatants including after loading and washing steps were diluted to a suitable concentration range with 5% HNO_3 and make 10mL solutions for ICP-OES analysis. The release capacity was then defined as the mass of iron divided by that of MSNs.

3.5.6. Cell culture and culture conditions

Human leukemia cancer cell line THP-1 cells (purchased from ATCC) were grown in RPMI-1640 media supplemented with 10% fetal bovine serum (FBS), 1% Penicillin-Streptomycin at a humidified 37 °C with 5% CO_2.

3.5.7. Cell viability assay

THP-1 cells are seeded at a density of 3000 cells/well in a 96-well plate (Grenier) with 1 μg/mL phorbol 12-myristate acetate (PMA) and incubated in fresh culture medium at 37 °C in a 5% CO_2 atmosphere for 24 hours. After 24 hours, cells are changed into fresh media and treatments are administered. Treatments are Fe@IDA-MSN, IDA-MSN, and free Fe(II) in the form of the ammonium iron(II) sulfate hexahydrate salt. 72 hours

after treatment, ATP content is measured using Promega CellTiter-Glo Luminescent Cell Viability Assay (CTG) according to manufacturer's instructions, and analyzed by SpectraMax M5 micro-plate spectrophotometer. For all viability data, treatments are done in triplicates. Release capacity of Fe@IDA-MSN (0.60 μmol Fe/mg MSN) from ICP-OES is used to calculate the concentration of free Fe(II) to add in the free iron treatment control condition.

3.5.8. Detection of reactive oxygen species (ROS)

Detection of ROS is assayed according to manufacturer's instructions (OxiSelect Intracellular ROS Assay Kit, Cell BioLabs Inc.). THP-1 cells were seeded in a 96-well plate at the density of 45000 cells/well with 1μg/mL PMA overnight. Dissolve 1 mg of H_2DCFHDA (2',7'-dichlorodihydro- fluorescein diacetate) (Sigma Aldrich) in 50 μL DMSO to make a 50 μM solution. 10 μL of H_2DCFHDA solution was added into 10 mL RPMI01640 without FBS to make a 50 nM solution. THP-1 cells were treated with H_2DCFHDA solution (100 μL in each well) prior to treatment for 45 minutes in the incubator. Cells were washed with DPBS twice and treated in fresh media containing treatments and H_2O_2 for positive control. Fluorescence is measured using a SpectraMax M5 microplate reader at an excitation wavelength of 485 nm and emission at 538 nm. Resulting fluorescence is proportional to ROS produced.

3.5.9. Verification of cell death from radicals

THP-1 cells are seeded at a density of 5000 cells/well in a 96-well plate (Grenier) with 1 μg/mL phorbol 12-myristate acetate (PMA) and incubated in fresh culture medium

at 37 °C in a 5% CO_2 atmosphere for 24 hours. After 24 hours, cells are changed into fresh media containing 5 mM N-Acetyl-L-cysteine (NAC). After treated with NAC for 24h, the treatments were 100 ug/mL Fe@IDA-MSN, 100 ug/mL IDA-MSN, and free Fe(II) in the form of the ammonium iron(II) sulfate hexahydrate salt. 72 hours after treatment, ATP content is measured using Promega CellTiter-Glo Luminescent Cell Viability Assay (CTG) according to manufacturer's instructions, and analyzed by SpectraMax M5 micro-plate spectrophotometer.

3.5.10. Verification of cell death from Fe delivered from IDA-MSN

THP-1 cells are seeded at a density of 5000 cells/well in a 96-well plate (Grenier) with 1 μg/mL phorbol 12-myristate acetate (PMA) and incubated in fresh culture medium at 37 °C in a 5% CO_2 atmosphere for 24 hours. After 24 hours, cells are changed into fresh media containing 0.01 mM 3-Hydroxy-1,2-dimethyl-4(1H)-pyridone (Deferiprone DFP). After treated with DFP for 24h, the treatments were 100 ug/mL Fe@IDA-MSN, 100ug/mL IDA-MSN, and free Fe(II) in the form of the ammonium iron(II) sulfate hexahydrate salt. 72 hours after treatment, ATP content is measured using Promega CellTiter-Glo Luminescent Cell Viability Assay (CTG) according to manufacturer's instructions, and analyzed by SpectraMax M5 micro-plate spectrophotometer.

3.5.11. Apoptosis assay

Cell death was examined by using a dual staining method for apoptosis and necrosis. Cells are seeded at a density of 1.5 X 10^6 and treated with 1 μg/mL phorbol 12-myristate acetate (PMA) one day prior to treatments were administered. After all the cells

were attached to the bottom, the cells were changed into fresh media and treatments were administered. After 72h treatment time, the apoptosis assay was administrated using Annexin V-Alexa Fluor 488 and Propidium Iodide dual stain according to manufacturer's instructions (Alexa Fluor 488 Annexin V/Dead Cell Apoptosis Kit, Thermo Fisher Scientific). The non-treatment cells were prepared for single stain, dual stain, and no stain samples as controls. The cells were treated with cisplatin to have positive control for apoptosis in order to divide the gate. The IDA-MSNs, free Fe(II), and Fe(II)@IDA-MSNs treated cells were double stained for FACS analysis. All flow cytometry data are acquired on a five-laser LSRII cytometer (BD Biosciences) and analyzed using FlowJo software.

3.5.12. Statistical Methods

Mean and standard deviation (SD) were calculated for each parameter. Comparisons between groups were evaluated by unpaired Student's t-test and one-way ANOVA. A statistically significant difference was assumed to exist when p was <0.05.

One way- ANOVA was used to see if there were any significant differences between any two data sets in which there were p is 10^{-14}. Student t test were used to compare two data sets compare their normalized means to each other.

3.6. Figures

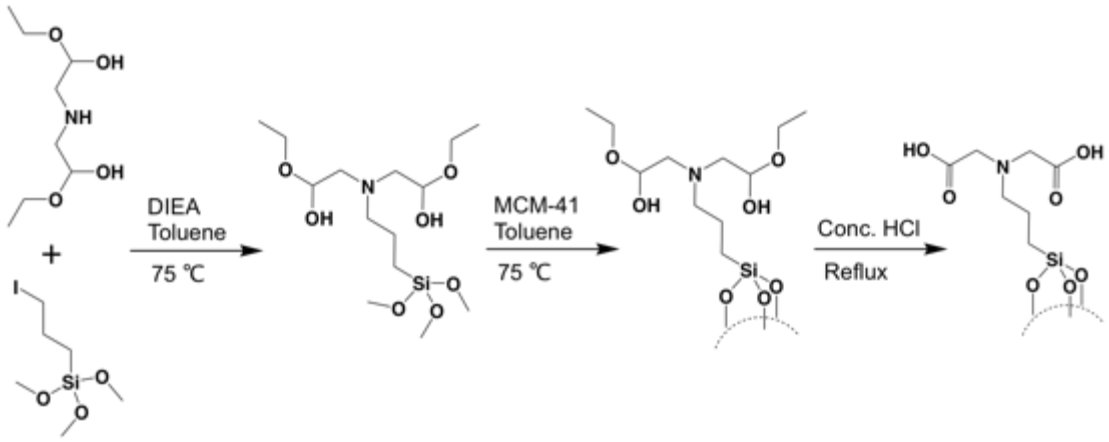

Figure 3.6.1. The synthesis scheme of IDA-MSNs

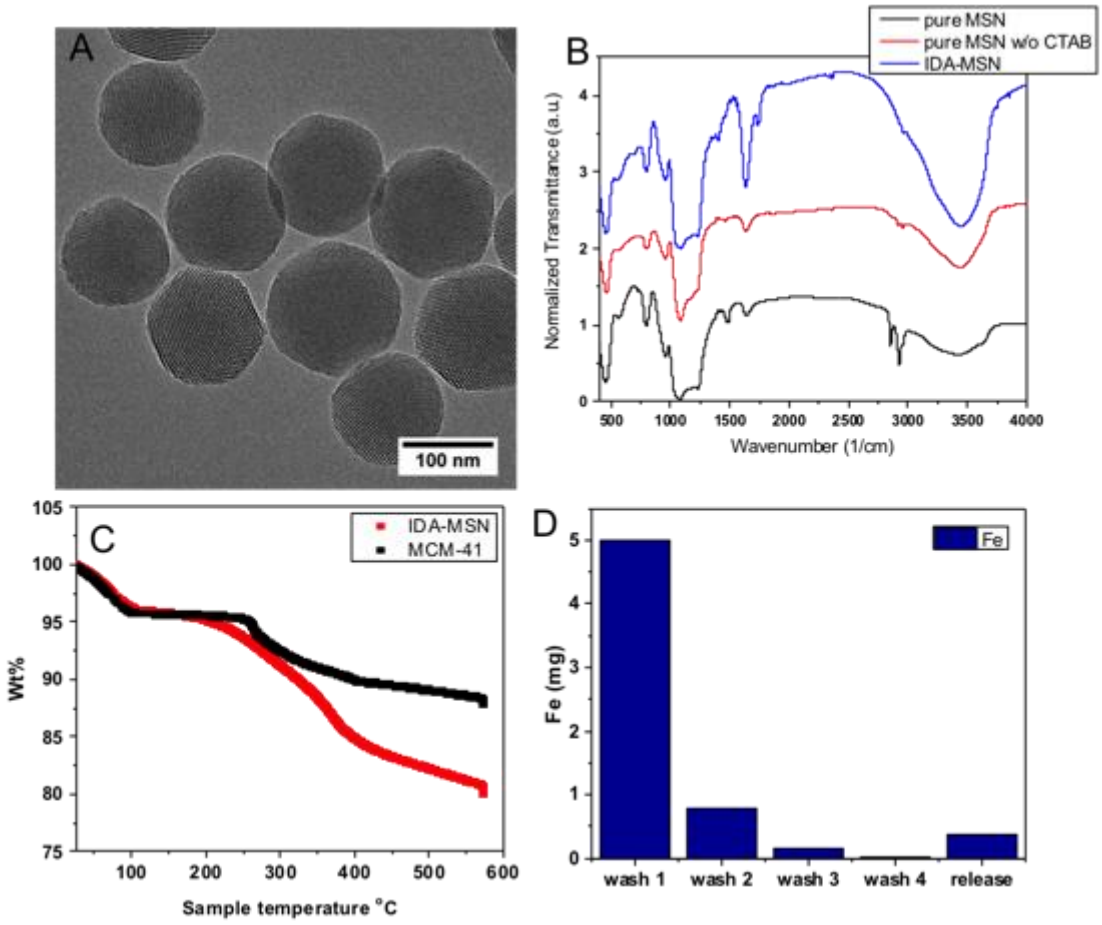

Figure 3.6.2. Characterization of IDA-MSNs. A. TEM images of MCM-41. B. the FTIR data of the synthetic steps of IDA-MSNs. C. TGA analysis of IDA-MSNs and MCM-41. D. ICP data of the supernatant solution of washing and releasing steps.

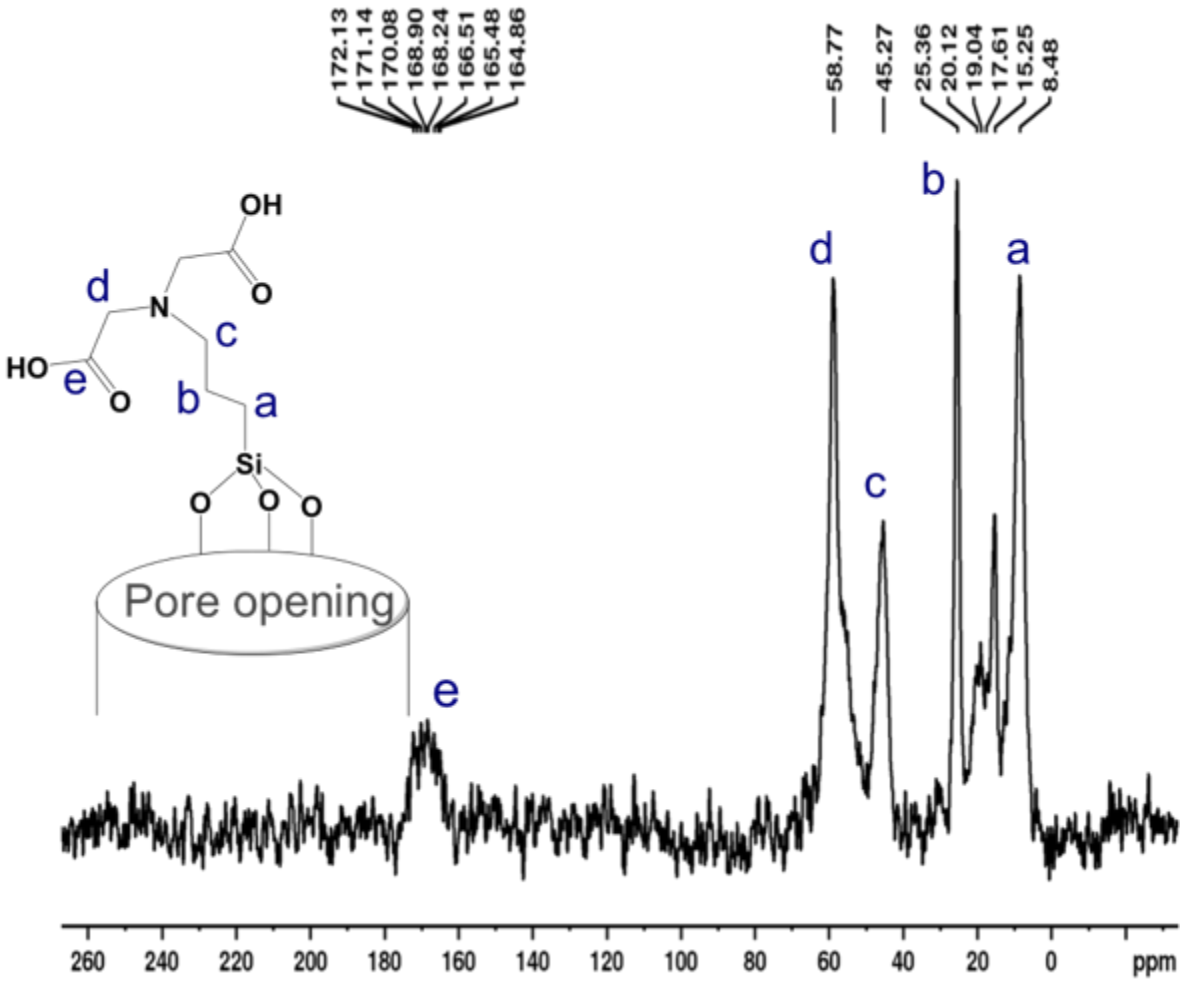

Figure 3.6.3. Solid state ^{13}C NMR spectrum of IDA-MSNs.

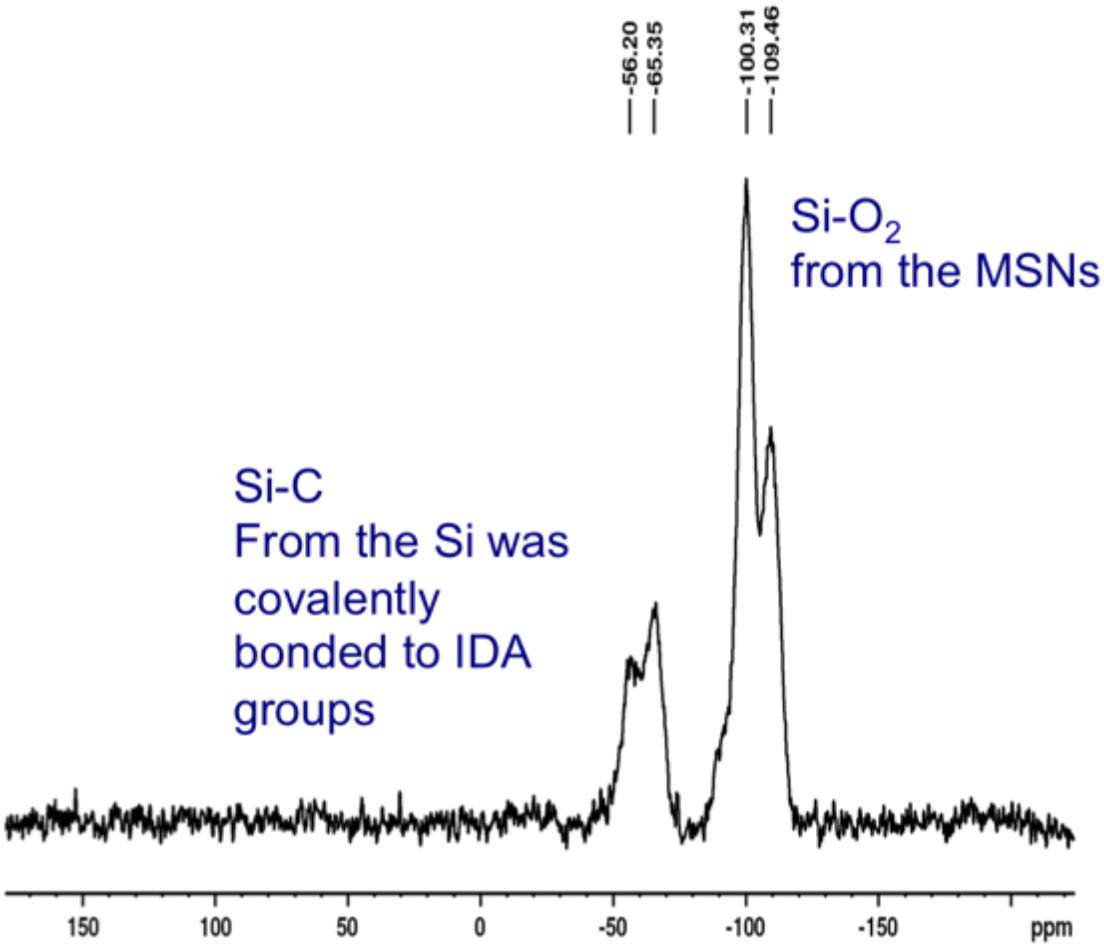

Figure 3.6.4. Solid state ^{29}Si NMR spectrum of iminodiacetic acid modified MSN.

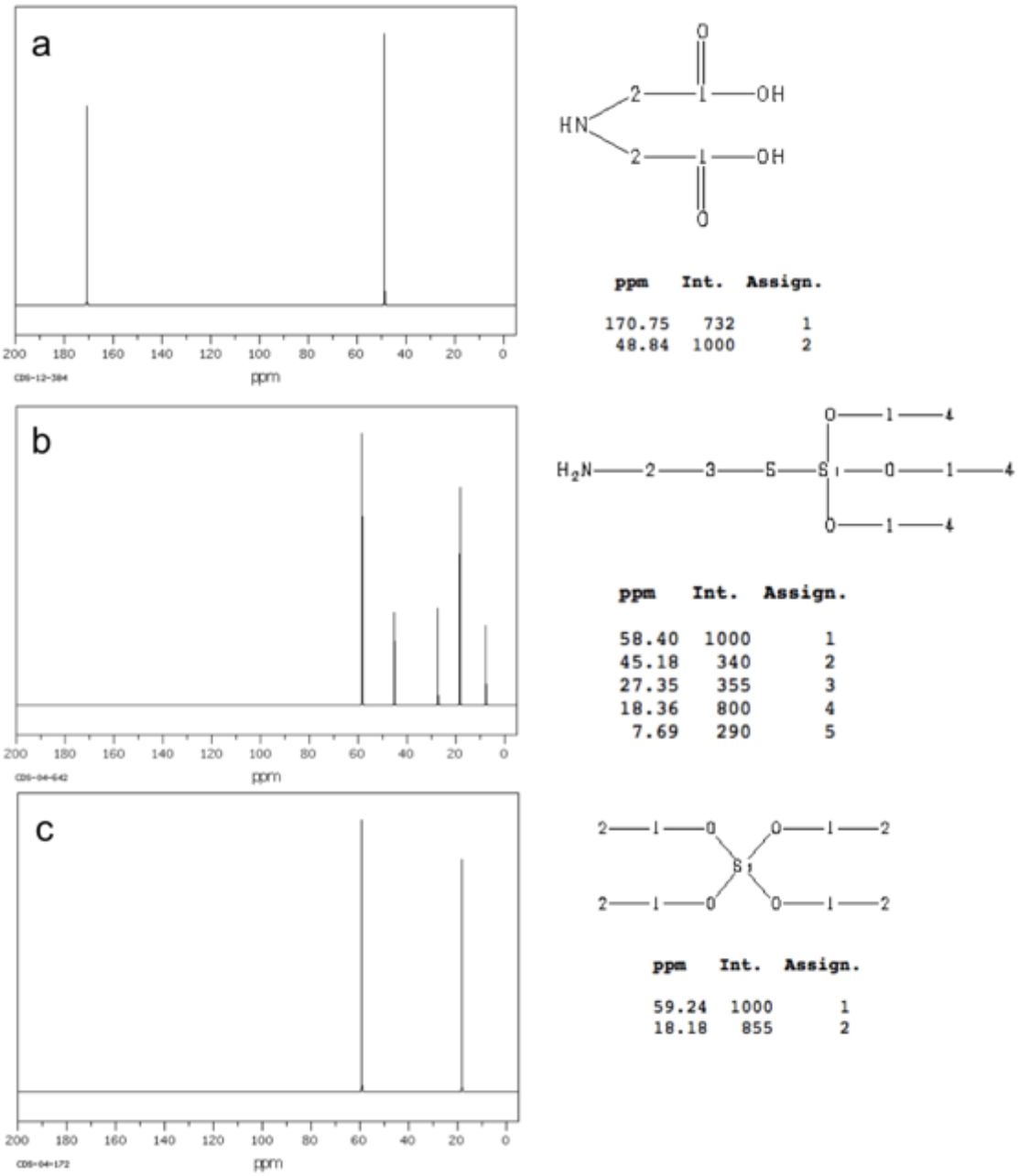

Figure 3.6.5. The ^{13}C NMR data references are obtained from the Spectral Database for Organic Compounds, SDBS. Figure 3.6.5a is the ^{13}C NMR data for iminodiacetic acid. Figure 3.6.5b is the ^{13}C NMR data for (3-aminopropyl) triethoxysilane. Figure 3.6.5c is the ^{13}C NMR data for tetraethyl orthosilicate (TEOS).

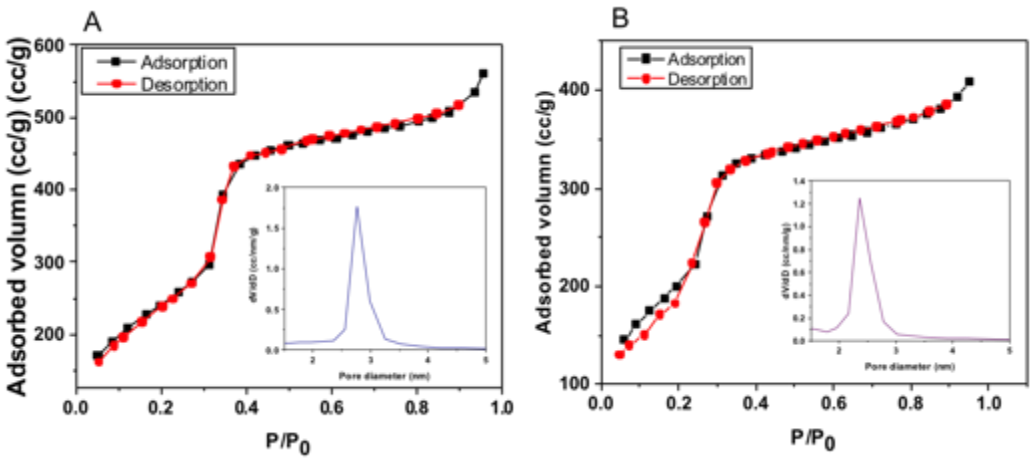

Figure 3.6.6. N_2 adsorption and desorption data of MCM-41 (A) and IDA-MSN (B) The inserts are the pore diameter distributions from BJH calculation.

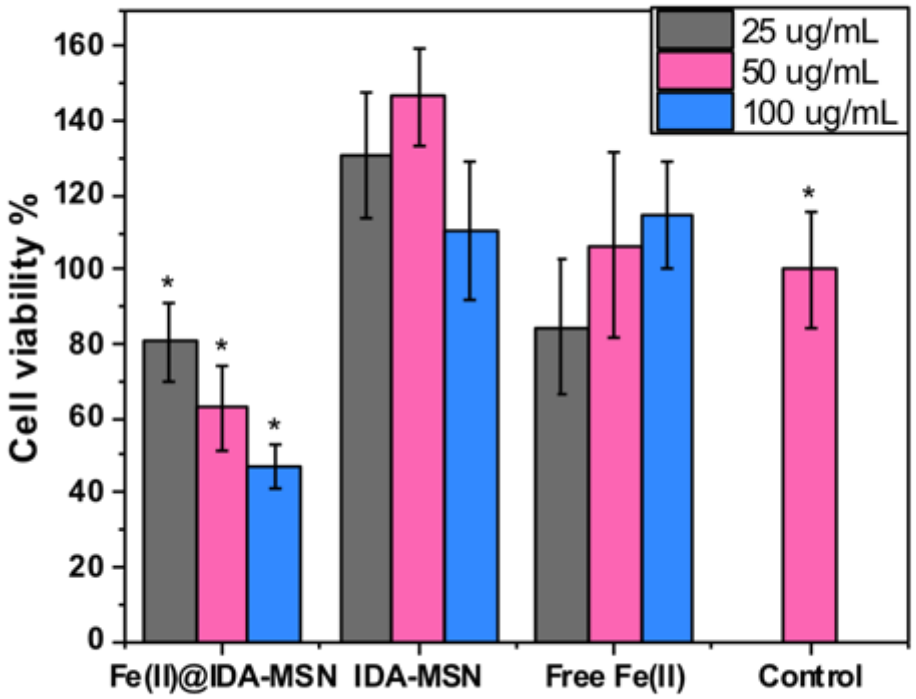

Figure 3.6.7. Assessment of Cell viability in THP-1 cells treated with IDA-MSNs, Fe(II) loaded IDA-MSNs and free Fe(II) for 72h. Cell viability tests were performed by CTG assay. Then the CTG assay solutions were added to evaluate cell viabilities by measuring the luminescence on a SpectraMax M5 microplate spectrophotometer. * = $p < 0.05$ when compared to each other using two-tailed t-tests

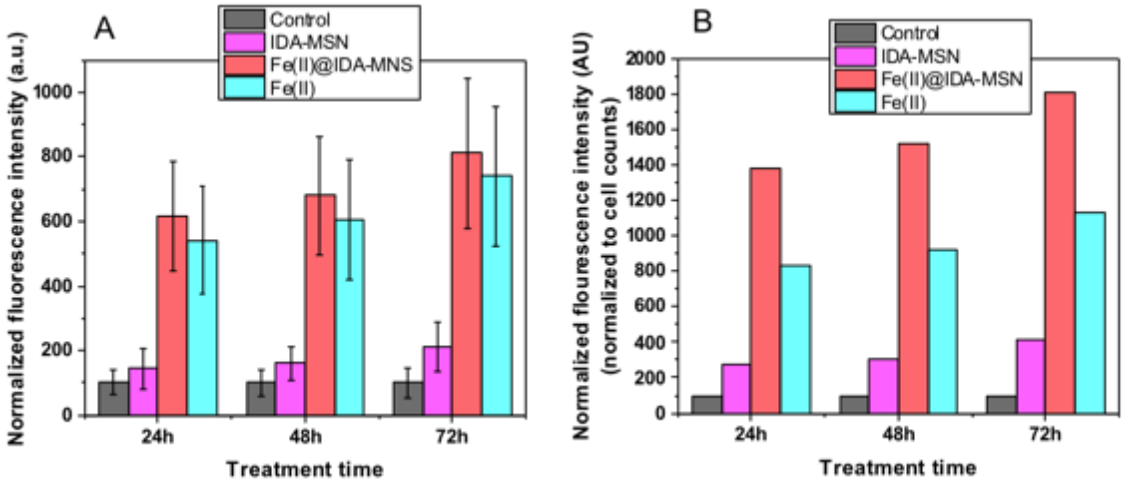

Figure 3.6.8. (A) Comparison of ROS generation in THP-1 cells with IDA-MSNs, Fe(II) loaded IDA-MSNs and free Fe(II). (B) The fluorescence was normalized to cell counts.

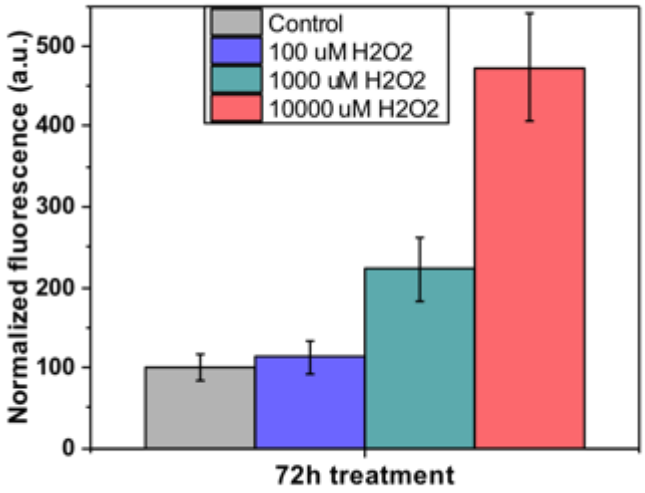

Figure 3.6.9. The positive control of ROS assay. THP-1 cells were treated with DCF and different concentration of H_2O_2.

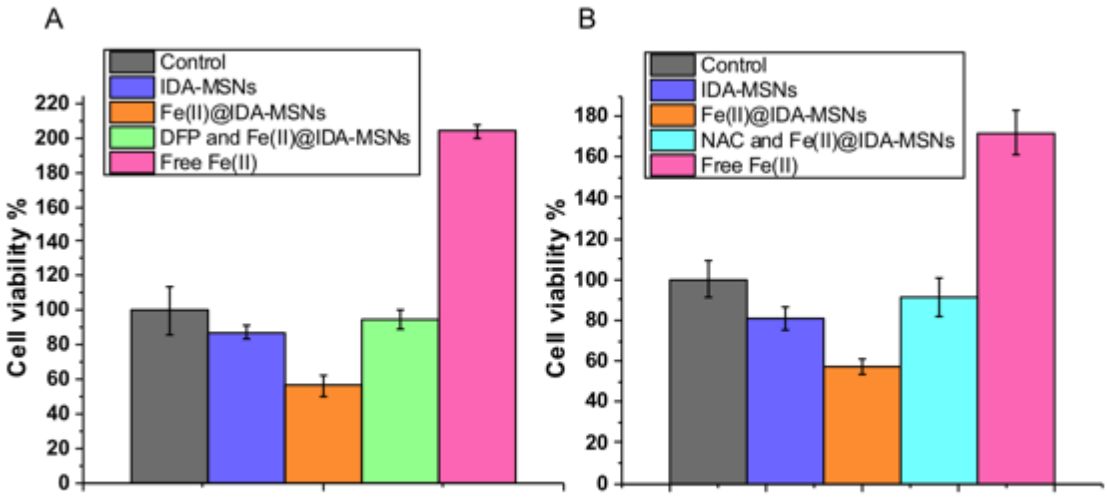

Figure 3.6.10A, The cell viability assay. The THP-1 cells were treated with DFP overnight, and then with Fe(II)@IDA-MSNs. 3.5.10B.The THP-1 cells were treated with NAC and then Fe(II)@IDA-MSNs. The cells were treated with free Fe(II), IDA-MSNs, Fe(II) loaded IDA-MSNs but not with DFP and NAC for comparisons. The control was the cells without treatment.

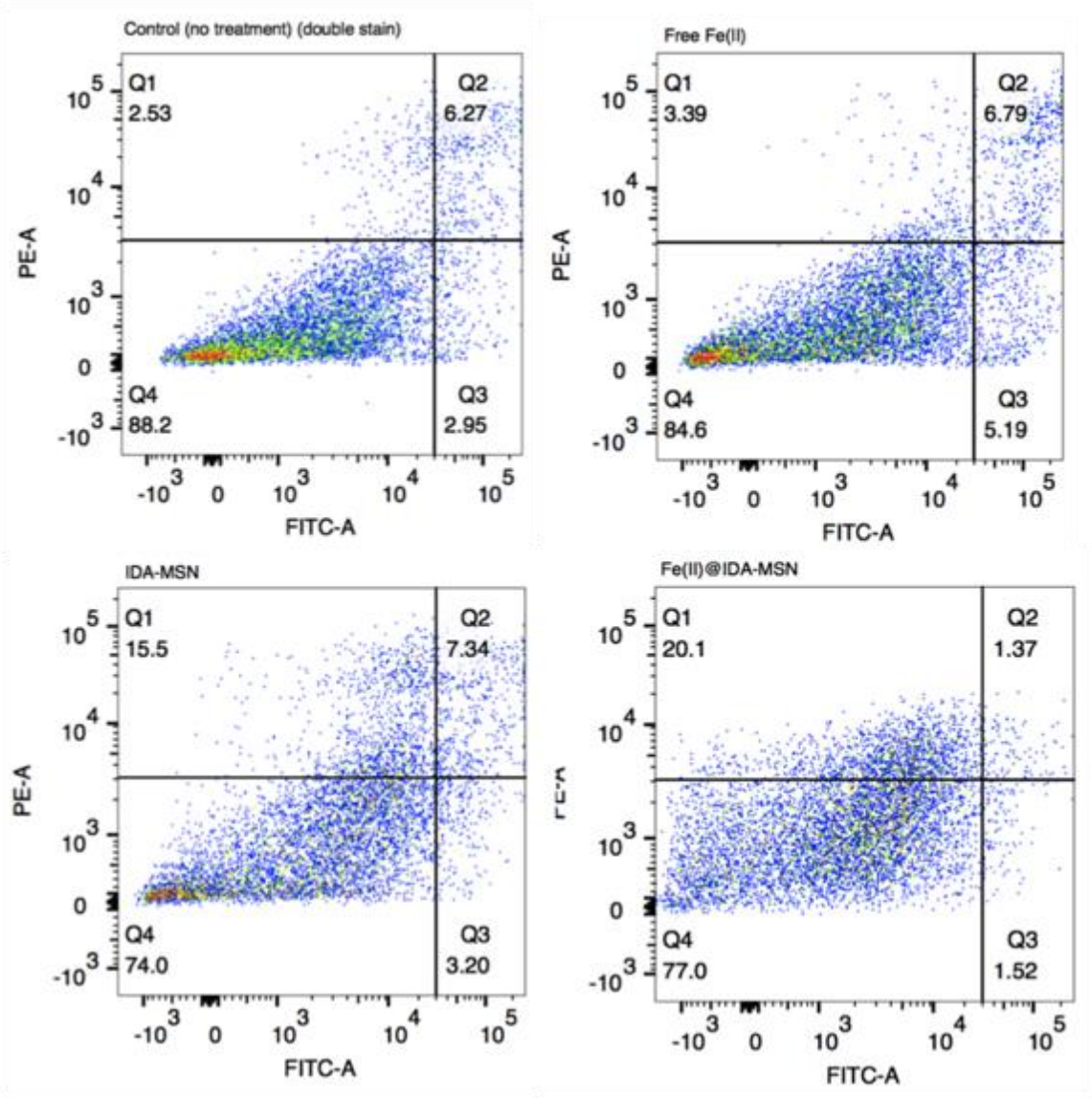

Figure 3.6.11. The apoptois assay. The cells were double stained with Annexin V-Alexa Fluor 488 and propidium iodide. The cells were treated with free Fe(II), IDA-MSNs, Fe(II) loaded IDA-MSNs. The control was the cells without treatment.

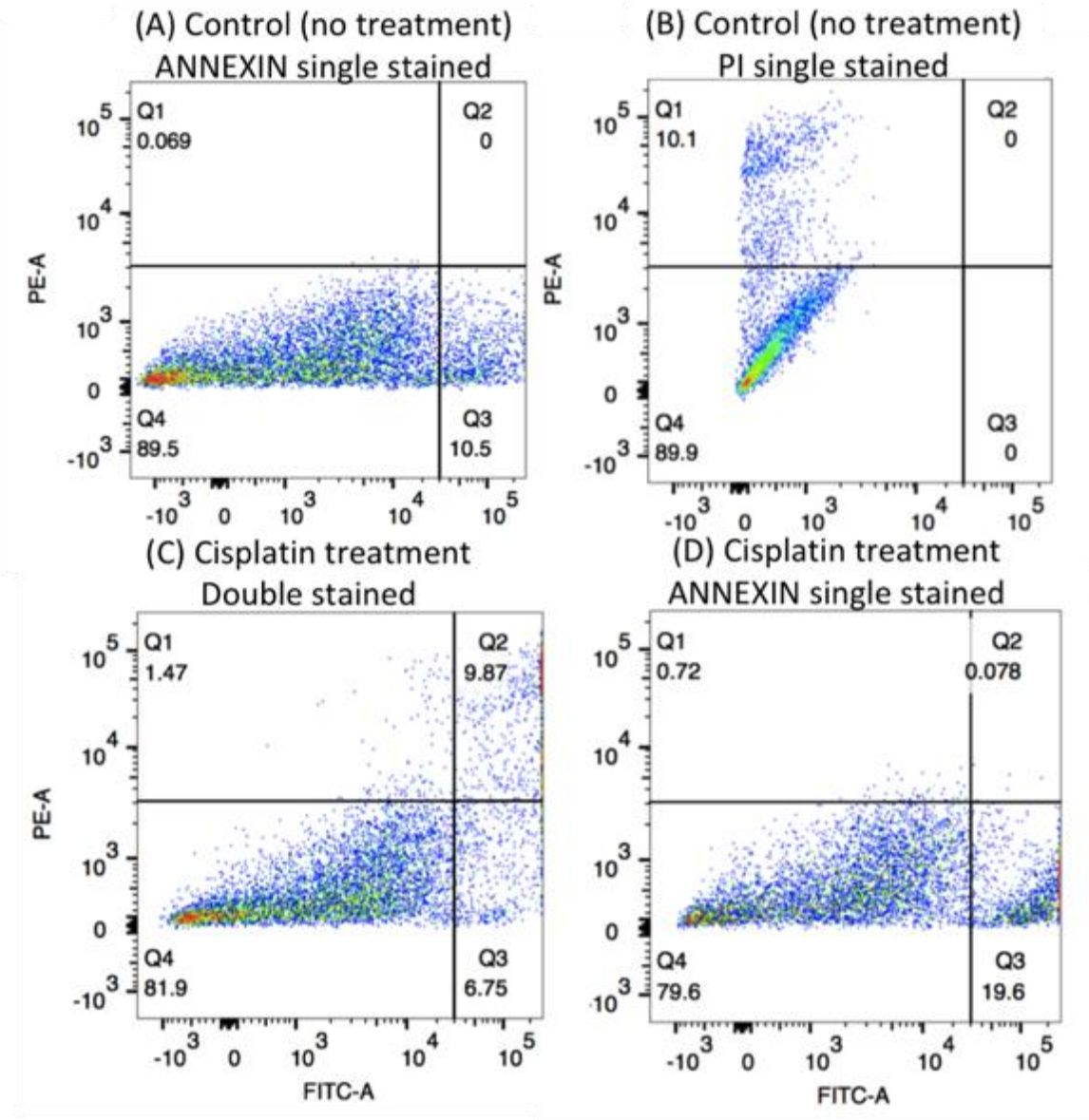

Figure 3.6.12. The positive control of necrosis assay. THP-1 cells were treated with cisplatin and then dual stained with PI and Annexin

3.7 References

1 Z. Shen, J. Song, B. C. Yung, Z. Zhou, A. Wu and X. Chen, *Adv. Mater.*, 2018, **30**, 1–15.

2 S. J. Dixon and B. R. Stockwell, *Nat. Chem. Biol.*, 2014, **10**, 9–17.

3 S. J. Dixon, K. M. Lemberg, M. R. Lamprecht, R. Skouta, E. M. Zaitsev, C. E. Gleason, D. N. Patel, A. J. Bauer, A. M. Cantley, W. S. Yang, B. Morrison and B. R. Stockwell, *Cell*, 2012, **149**, 1060–1072.

4 C. C. Winterbourn, *Toxicol. Lett.*, 1995, **82**–**83**, 969–974.

5 M. López-Lázaro, *Cancer Lett.*, 2007, **252**, 1–8.

6 Z. Zhou, J. Song, R. Tian, Z. Yang, G. Yu, L. Lin, G. Zhang, W. Fan, F. Zhang, G. Niu, L. Nie and X. Chen, *Angew. Chemie - Int. Ed.*, 2017, **56**, 6492–6496.

7 P. Ma, H. Xiao, C. Yu, J. Liu, Z. Cheng, H. Song, X. Zhang, C. Li, J. Wang, Z. Gu and J. Lin, *Nano Lett.*, 2017, **17**, 928–937.

8 C. Vilchèze, T. Hartman, B. Weinrick and W. R. Jacobs, *Nat. Commun.*, , DOI:10.1038/ncomms2898.

9 X. Sun, X. Niu, R. Chen, W. He, D. Chen, R. Kang and D. Tang, *Hepatology*, 2016, **64**, 488–500.

10 M. Lo, Y. Z. Wang and P. W. Gout, *J. Cell. Physiol.*, 2008, **215**, 593–602.

11 W. P. Li, C. H. Su, Y. C. Chang, Y. J. Lin and C. S. Yeh, *ACS Nano*, 2016, **10**, 2017–2027.

12 C. Zhang, W. Bu, D. Ni, S. Zhang, Q. Li, Z. Yao, J. Zhang, H. Yao, Z. Wang and J. Shi, *Angew. Chemie - Int. Ed.*, 2016, **55**, 2101–2106.

13 L. Yue, J. Wang, Z. Dai, Z. Hu, X. Chen, Y. Qi, X. Zheng and D. Yu, *Bioconjug.*

Chem., 2017, **28**, 400–409.

14 D. W. Zheng, Q. Lei, J. Y. Zhu, J. X. Fan, C. X. Li, C. Li, Z. Xu, S. X. Cheng and X. Z. Zhang, *Nano Lett.*, 2017, **17**, 284–291.

15 H. Maeda, J. Wu, T. Sawa, Y. Matsumura and K. Hori, *J. Control. Release*, 2000, **65**, 271–284.

16 A. K. Iyer, G. Khaled, J. Fang and H. Maeda, *Drug Discov. Today*, 2006, **11**, 812–818.

17 R. Bazak, M. Houri, S. El Achy, S. Kamel and T. Refaat, *J. Cancer Res. Clin. Oncol.*, 2015, **141**, 769–784.

18 M. Liong, J. Lu, M. Kovochich, T. Xia, S. G. Ruehm, A. E. Nel, F. Tamanoi and J. I. Zink, *ACS Nano*, 2008, **2**, 889–896.

19 H. Meng, M. Xue, T. Xia, Z. Ji, D. Y. Tarn, J. I. Zink and A. E. Nel, *ACS Nano*, 2011, **5**, 4131–4144.

20 E. L. Mackenzie, K. Iwasaki and Y. Tsuji, *Antioxid. Redox Signal.*, 2008, **10**, 997–1030.

21 A. Popat, S. B. Hartono, F. Stahr, J. Liu, S. Z. Qiao and G. Qing (Max) Lu, *Nanoscale*, 2011, **3**, 2801.

22 J. E. Lee, N. Lee, T. Kim, J. Kim and T. Hyeon, *Acc. Chem. Res.*, 2011, **44**, 893–902.

23 Z. Li, J. C. Barnes, A. Bosoy, J. F. Stoddart and J. I. Zink, *Chem. Soc. Rev.*, 2012, **41**, 2590.

24 H. Irving and D. H. Mellor, *J Chem Soc*, 1962, 5222–5237.

25 S. Chaberek and A. E. Martell, *J. Am. Chem. Soc.*, 1952, **74**, 5052–5056.

26 D. Tarn, M. Xue and J. I. Zink, *Inorg. Chem.*, 2013, **52**, 2044–2049.

27 D. Tarn, C.-J. Yu, J. Lu, A. Hartz, F. Tamanoi and J. I. Zink, *Mol. Syst. Des. Eng.*, 2017, **2**, 384–392.

28 E. S. Lee, Z. Gao and Y. H. Bae, *J. Control. Release*, 2008, **132**, 164–170.

29 M. Xue, X. Zhong, Z. Shaposhnik, Y. Qu, F. Tamanoi, X. Duan and J. I. Zink, *J. Am. Chem. Soc.*, 2011, **133**, 8798–801.

30 N. Mobarra, M. Shanaki, H. Ehteram, H. Nasiri, M. Sahmani, M. Saeidi, M. Goudarzi, H. Pourkarim and M. Azad, *Int. J. Hematol. Stem Cell Res.*, 2016, **10**, 239–247.

31 O. I. Aruoma, B. Halliwell, B. M. Hoey and J. Butler, *Free Radic. Biol. Med.*, 1989, **6**, 593–597.

32 V. M. Gonzalez, M. a Fuertes, C. Alonso and J. M. Perez, *Mol. Pharmacol.*, 2001, **59**, 657–663.

33 A. H. Lau, *Kidney Int.*, 1999, **56**, 1295–1298.

Chapter 4

Cellular uptake efficiency study of enhanced T_1 relaxivity gadolinium-loaded iminodiacetic acid modified mesoporous silica nanoparticles

4.1 Abstract

The rational design of theranostic for enhanced diagnostic imaging in response to tumor milieu is critical for efficient cancer chemotherapy. The gadolinium (Gd)-based contrast agents have attracted lots of attention due to the high T_1 enhancement from Gd. However, the toxicity of Gd-related contrast agents from high dosage being injected still has to be further reduced. We herein fabricate the iminodiacetic acid modified mesoporous silica nanoaprticles (IDA-MSNs) to chelate to Gd^{3+} ions for magnetic resonance imaging (MRI) purposes. Concerning the toxicity of existing MRI contrast agents, the cellular uptake study of Gd laoded IDA-MSNs was conducted and carefully compared to that of Magnevist (Gd-DTPA). The cellular uptake efficiency of Gd-loaded IDA-MSNs is 600 times higher than that of Gd-DTPA. The T_1 relaxivity of Gd-loaded IDA-MSNs increased 7.2-fold over that of the Gd-DTPA. Combining the advantages of the high relaxivity and low dosage of Gd-loaded IDA-MSNs, the toxicity from the total Gd ions being injected can be greatly reduced.

4.2. Introduction

Magnetic resonance imaging (MRI) technology has been has used widely in clinical diagnostic therapies.[1] MRI is noninvasive which doesn't involve X-rays, and has been used to detect the whole body scans for tumor, infection, and infraction.[2] However, the sensitivity of MRI is not enough to detect early stage tumors or inflammations. As a result, various MRI contrast agents can be used to improve the contrast between normal and diseased tissues based on their magnetic functions.[3–6] The main requirements of MRI contrast agents are to have a strong effect on the longitudinal ($1/T_1$) and transverse ($1/T_2$) relaxation rate of water protons and a low toxicity.[3] Gadolinium has attracted great attention throughout the development of MRI contrast agents because of its large number (seven) of unpaired electrons.[4] However, the high toxicity of free Gd^{3+} (LD_{50} = 0.5 mmol/kg intravenous injection) must be reduced via chelation before its high relaxivity can be utilized.[7,8] Currently, the most widely used Gd contrast agent is Magnevist ($[Gd(DTPA)(H_2O)]^{2-}$ (LD_{50} = 10 mmol/kg, intravenous injection) where DTPA is diethylenetriaminepentaacetic acid which is an octadentate ligand. The Gd(DTPA) has shown a greatly reduced toxicity (LD_{50} = 10 mmol/kg when intravenously injected) but it is a poor targeting agent due to its inability to distinguish between tumors and healthy tissues.[9–11] As a result, a Gd-based contrast agent with higher r_1 (relaxivity rate) and better targeting property is still in demand, which can be achieved via two ways. First, the available coordination sites for water molecules can be increased. Second, the overall molecular weight of the Gd^{3+} complex can be boosted by binding Gd^{3+} to a bigger ligand or confined Gd space in order to decrease the rotation correlation (tumbling) time.[12,13]

Mesoporous silica nanoparticles (MSNs) have been used in various bio-

applications due to their high porosity, large surface area (~1000 m^2/g, MCM-41), biocompatibility,[14] and capability of chemical modification.[15–17] The porosity provides access for the water molecules to come inside the pores and coordinate to the Gd^{3+} ions, while its large surface and adaptability to chemical modification provide the possibility to deliver small cargos such as metal ions directly into targets through passive targeting enhanced permeability and retention effect (EPR effect).[18,19] The applications combining MSNs and Gd as nano-medicine contrast agents have been reported to achieve enhanced water solubility, high loading capacity, sustained or triggered release, and site-specific accumulation within tumor tissues.[20–25] However, concerning the toxicity of Gd related contrast agent, careful investigation of cell uptake of the nano-medicine and comparison to Magnevist has to be conducted.

Here we report a method to chelate Gd^{3+} onto the surface of mesoporous silica nanoparticles to decrease the rotation correlation time of Gd^{3+}. The IDA is a tridentate ligand. By using two iminodiacetic acid (IDA) groups to coordinate to Gd^{3+} to form a hexadentate complex, it leaves three coordination sites on Gd available for water. In this work, we also demonstrate a 666 times increase in the uptake of Gd^{3+} into cancer cells by delivering through iminodiacetic acid group modified MSNs, as compared to the Magnevist Gd(DTPA). This suggests that the dose of contrast agent can be reduced 666 times with the more effective delivery of Gd^{3+}.

4.3. Results and discussions

4.3.1. Synthesis of silica mesoporous nanoparticles and surface modification with IDA

The same IDA-MSNs were used in chapter 3. The detailed synthesis and

characterization are described in section 3.3.1.

4.3.2. Gd uptake and release

In order to test the capability of IDA-MSNs to deliver Gd^{3+}, the IDA-MSNs were loaded with Gd^{3+} by being suspended in a $GdCl_3$ solution overnight. After the Gd ions were chelated, the Gd^{3+} loaded IDA-MSNs were collected by centrifugation and washed with water four times to make sure that the adsorbed Gd^{3+} on the surface of MSNs was washed off as shown in figure 4.6.1.

The wash 1 was the loading supernatant separated from the Gd-loaded IDA-MSNs. The wash 2-4 was the supernatant solutions from the Gd-loaded IDA-MSNs being re-suspended in fresh Millipore water and collected through centrifugation and analyzed by ICP-OES. The particles were suspended in pH 5 HNO_3 solutions overnight to release all of the Gd^{3+} and the amount released Gd^{3+} was measured by ICP-OES. The IDA-MSNs had an average release capacity of 0.16 μmol/mg of particles with a maximum in one of the batches of 0.232 μmol/mg of particles (Table 4.6.1). Zeta potential was conducted to confirm the Gd chelated IDA-MSNs. As shown in figure 4.6.2, the pure MCM-41 has -35 charge from the silanol ($Si\text{-}O^-$) on the surface; after postgrafting of Diethyl Iminodiacetate-Propyltriethoxysilane, the charge became -10 due to the consumption of some silanol groups; after converting COOEt to COOH groups, the particles carried -40 charge since at pH 7 carboxylate groups were deprotonated; after the introduction of Gd^{3+}, as some of the COO^- groups were chelated to Gd^{3+}, the surface charge became -13.

4.3.3. MRI results of Gd-loaded IDA-MSN and Magnevist

From figure 4.6.3, the Gd-loaded IDA-MSNs at pH 7 and pH 5 showed dose-dependent T_1 value change, meaning these Gd-loaded IDA-MSNs behaved as T_1 contrast agent. What is worthy to note is that the Gd-loaded IDA-MSNs showed a stronger T_1 contrast than the Magnevist. The 2.5 mg/mL IDA-MSNs, which had 375 nmole Gd^{3+}, showed T_1 of 102 ms compared to the 699.5 ms of the 320 nmole Magnevist. Even 640 nmole Magnevist had T_1 of 400 ms which was still higher than that of 2.5 mg/mL Gd-loaded IDA-MSNs which had 375 nmole of Gd^{3+}. The same phenomenon happened in the Gd^{3+} and IDA-MSN mixure under a pH of 5, in which case the Gd^{3+} was released from IDA-MSNs so the T_1 contrast came from the mixture of free Gd^{3+} and Gd on the IDA-MSNs in the gel. The 0.5 mg/mL mixture of free Gd^{3+} and Gd on the IDA-MSNs had a total 75 nmole of Gd^{3+}, which showed 759 ms T_1 contrast and was still better than 160 nmole Magnivest (819 ms). For a closer look at the pH 5 condition, the released Gd^{3+} and IDA-MSNs were separated. The data showed the T_1 contrast of IDA-MSNs did not depend on dosage and the Gd^{3+} in supernatant had similar T_1 contrast of the mixture of free Gd^{3+} and leftover Gd on the IDA-MSNs. The relaxivity (r_1) was calculated from the plot of Gd concentration (mM) vs. reciprocal value of relaxation times ($1/T_1$) as shown in figure 4.6.4. When the Gd was chelated on the surface of MSNs, the r_1 was 23.83 $mM^{-1}s^{-1}$. After Gd^{3+} was released from MSNs and entered the water/gel matrix, the relaxivity was 11.6 $mM^{-1}s^{-1}$, which is similar to free Gd^{3+} (r_1= 12.6 $mM^{-1}s^{-1}$). Comparing to Magnevist in the water/gel matrix which had a relaxivity of 3.3 $mM^{-1}s^{-1}$, the MSNs as a platform to deliver Gd enhanced the relaxivity 7 times, which means the Gd-loaded IDA-MSNs can achieve to same level of T_1 contrast with lower Gd^{3+} concentration than

Magnevist. The results agree with the theory that by slowing the rotational tumbling rate of Gd by binding Gd onto a bigger molecule or platform, its r_1 can be effectively increased. Since the coordination number of free Gd^{3+} is nine, when it chelates with two IDA groups, it has 3 coordination sites for water molecules. In comparison, DTPA ligand of Magnevist uses 8 out of 9 coordination sites, so only one coordination site is available for water molecule. Overall, the free Gd^{3+} (the pH 5 condition) and the chelated Gd^{3+} on the MSNs have significantly lower T_1 value than Gd(DTPA) which is consistent with literature.[27] The MRI imaging picture of comparison among Magnevist, Gd-loaded IDA-MSN at pH 7, and Gd-loaded IDA-MSN at pH 5 is shown in figure 4.6.5.

4.3.4. Cell toxicity and uptake study

In order to compare the Gd-loaded IDA-MSNs and Magnevist T_1 contrast in cells, the uptake study was conducted. The PANC-1 cells were treated with different concentrations of Gd-loaded IDA-MSNs and Magnevist. From figure 4.6.6, the Gd uptake amount in the cells was obtained. 1 mg of IDA-MSNs carries 0.15 μmole of Gd^{3+}, and the concentration of the stock of Magnevist is 500 mM and the treated Gd μmole was calculated for comparison as shown in 4.6.2. In order to get the same amount of Gd in the cells for efficient MRI imaging, for example, 500 μmole of Magnevist was needed for a Gd uptake amount of around 80 nmole. In contrast, if the Gd was delivered by IDA-MSNs, only 5 mg of IDA-MSNs were needed which carried 0.75 μmole Gd, which means the overall Gd dose was decreased by 666 times. In order to get a Gd uptake of around 20 nmole in cells, 50 μmole of Magnevist was needed which was also 666 times more compared to 0.075 μmole Gd delivered by IDA-MSNs. When the dose of

Magnevist was as low as 25 μmole, the cell uptake was around 9 μmole, while the Gd dose needed was only 0.01875 μmole when delivered with IDA-MSNs, which suggested that efficiency was 1333 times different between Gd on MSNs or Magnevist. The route of entry for MSNs is endocytosis, and many studies have shown accumulation of nanoparticles in endosomes and lysosomes in tumor cells. Through endocytosis, the Gd^{3+} loaded IDA-MSNs were delivered into the cells efficiently since the concentrated Magnevist and Gd^{3+} loaded IDA-MSNs were treated. From the study of Gd uptake in cell, it is clear that the dose for Gd content can be reduced by at least 300 times compared to Magnevist, which can lead to a great reduction of toxicity in the body. The toxicity of Gd for cells was also checked. The cell proliferation assay is shown in figure 4.6.7, where the treatment concentration of Gd-loaded IDA-MSNs, IDA-MSNs and Magnevist was consistent with the concentration that was monitored in MRI *in vitro* study. As the data showed, the concentration of the three materials treated in cells was safe for the cells.

4.3.5. *In vitro* MRI

Figure 4.6.8 showed that the T_1 values of cells which were treated with various concentrations of Gd IDA-MSNs and Magnevist. From the data, the T_1 value was changed based on different amount of Gd^{3+} inside the cells. After cells endocytosed the Gd^{3+} loaded IDA-MSNs, the pH in the lysosomes caused the Gd^{3+} to be released into the cells. The Gd^{3+} leaving the surface of MSNs caused the relaxivity to drop down to same level as Magnevist. However, in order to get the same T_1 contrast in the 500 μmole Magnevist treated cells, the needed Gd on the IDA-MSNs was as low as 0.75 μmole meaning the overall Gd was decreased 666 times.

4.4. Conclusion

In conclusion we have synthesized Gd^{3+} chelated iminodiacetic acid modified mesoporous silica nanoparticles (IDA-MSNs). Gd-loaded IDA-MSN displays much higher relaxivity (25 $mM^{-1}s^{-1}$) than that of Magnevist $[Gd(DTPA)(H_2O)]^{2-}$(3.5 $mM^{-1}s^{-1}$); this is likely because more than one water can be coordinated to Gd^{3+} (4-5 coordination sites available one the surface of MSNs and 8-9 coordination sites for free Gd^{3+}) and a substantial decrease of the Gd metal ion rotational motion when they were chelated onto the surface of MSNs. The observed high r_1 values, nanosize, easy derivatization and biocompatible of silica make Gd-incorporated mesoporous silica a versatile new class of MRI contrast agent. In recent years, the high demand of low toxicity and targeted MRI contrast agent is urgently needed. Our development of high r_1 nanosized mesoporous silica may help toward the goal of high imaging capability with significantly lower dose of Gd^{3+}. Together with high efficiency of delivering Gd into cancer cells and high r_1 value, these materials can serve as a targeted drug delivery system with visualization.

4.5. Experimental

4.5.1. Chemicals and characterizations

Gadolinium(III) chloride hexahydrate (99.9%, Alfa Aesar), Gd ICP standard (1000ppm, AccuStandard), Methyl cellulose (Aldrich) were used as received.

4.5.2. Loading Gd into IDA-MSNs and triggering release

To load the IDA-MSNs with Gd^{3+} ions, 10 mg IDA-MSNs were stirred in a GdCl3-solution (500 mg/mL, Millipore water) overnight. To collect the gadolinium

loaded IDA-MSNs, the MSNs were centrifuged down and then washed with 1 mL millipore water four times. The collected calcium loaded IDA-MSNs were re-suspended in 1 mL millipore water.

The triggered gadolinium ion release was measured by suspending the gadolinium loaded IDA-MSNs in 1 mL pH 5 HNO_3 solution overnight. Particles were centrifuged down and the amount of gadolinium ions in the resulting supernatant was determined by ICP-OES. 1000 ppm Gd standard solution was used to make standard solutions of 0.1 to 30 ppm for making calibration curve.

1 mL of each centrifuged supernatants including after loading and washing steps were diluted 10 times with 4% HNO_3 to make 10 mL solutions for ICP-OES analysis. The release capacity was then defined as the mass of gadolinium divided by that of MSNs.

4.5.3. Sample preparation of Gd-loaded IDA-MSNs and Magnevist for MRI

The MSNs and Magnevist were suspended in methyl cellulose gel homogeneously. The gel is made from 2 wt% methyl cellulose in Millipore water. The 1 g methyl cellulose was put in 25 mL water and was heated to 80 °C until the methyl cellulose was softened and easy to disperse. The hot mixture was added into 25 mL r.t Millipore water and then was stirred until the solution cooled down to r.t.. The solution was put in the 4 °C refrigerator for 2 h to form the gel. The gadolinium loaded IDA-MSNs were prepared as mentioned above and the MSNs were divided into various portions (10, 4, 2, 1, 0.4, 0.3, 0.2, 0.1 mg) and then suspended in 1 mL pH 7 or pH 5 HNO_3 solutions. The 1 mL of Gd-loaded IDA-MSNs solutions were mixed into 3 mL gel

and stored at 4 °C for 3 h in order to get rid of bubbles. The Magnevist was diluted at various concentrations in 1 mL Millipore water and then was mixed with the gel and stored at 4 °C for 3 h.

4.5.4. Cell culture and culture conditions

Human cancer-cell line PANC-1 was obtained from the American Type Culture Collection and maintained in Dulbecco's modified Eagle's medium (DMEM; Fisher; GIBCO) supplemented with 10% fetal calf serum (Fisher; GIBCO), 2% l-glutamine, 1% penicillin, and 1% streptomycin stock solutions (Fisher; GIBCO) at a humidified 37 °C with 5% CO_2. The media were changed every three days, and the cells were passaged by trypsinization (0.05% w/v Trypsin; GIBCO) before confluence.

4.5.8. Cell uptake study

PANC-1 Cells were seeded in 100 mm petri dishes (2 X 10^6 cells/petri dish) and incubated in fresh culture medium at 37 °C in a 5% CO_2/ 95% air atmosphere for 24 h. The cells were then washed with PBS and the medium was changed to a fresh medium containing Magnevist (50, 100, 250, 500, 1000 uL of stock solution in 10 mL medium) and gadolinium loaded IDA-MSN (0.0125, 0.05, 0.25, 0.5, 1 mg/mL) at the indicated concentrations. 3 petri dishes were used for one concentration treatment. After 24 h, the cells were washed with PBS to remove nanoparticles that were not taken up by the cells, and the cells were trypsinized and washed with 8-10 mL PBS and collected. The collected cells (around 20 x 10^6 cells for each treatment) were digested for ICP analysis. The as-collected cells were put in hot block (95 °C) for 4 h to dry the PBS and then

cooled down to r.t. 10 mL Aqua Regia were added into the cells and stayed at r.t. for 1 h until all the cells were dissolved. The solutions were put in hot block (95 °C) overnight. The fresh 4% 10 mL HNO_3 solutions were added into cells for 2 h at 95 °C in order to dissolve gadolinium back in the solutions. The as-prepared solutions were ready for ICP analysis.

4.5.5. Cell preparation for MRI

The PANC-1 cells were seeded at the density of 2 X 10^6 cells/petri dish and incubated in fresh culture medium at 37 °C in a 5% CO_2/ 95% air atmosphere for 24 h. The cells were then washed with PBS and the medium was changed to a fresh medium containing Magnevist (10, 50, 100, 500, 1000 uL of stock solution) and gadolinium loaded IDA-MSN (0.0125, 0.05, 0.25, 0.5, 1 mg/mL) at the indicated concentrations. Three petri dishes were used for one treatment meaning the cells amount was tripled. After 24 h, the cells were washed with PBS to remove nanoparticles that were not taken up by the cells, and the cells were trypsinized and collected by centrifuge. The collected cells were combined from 3 petri dishes and suspended in 200 µL PBS beffer and put in the 600 µL eppendorf tube. The 600 µL eppendorf tubes were filled with 300 □L methyl cellulose gel. The 200 µL cell suspension was mixed with the gel.

4.5.6. Proliferation assays

PANC-1 cells were seeded at a density of 10^4 cells/well in a 96-well plate and incubated in fresh culture medium at 37 °C in a 5% CO_2 atmosphere for 24 hours. After 24 hours, cells were changed into fresh media and treatments are administered. Treatments were Gd-loaded IDA-MSN (1000, 500, 250, 50, 12.5 ug/mL) and Magnevist

(100, 50, 10, 5, 1uL/mL). 24 hours after treatment, ATP content was measured using Promega CellTiter-Glo Luminescent Cell Viability Assay (CTG) according to manufacturer's instructions, and analyzed by Tecan Infinite M1000 Plate Reader. For all viability data, treatments were done in triplicates. Release capacity of Gd-loaded IDA-MSN (0.16 μmol Gd/mg MSN) from ICP-OES was used to calculate the concentration of Magnevist to treat the cells.

4.5.7. MRI Protocols

MRI scans were conducted to measure the T_1 and T_2 relaxation times of cells treated with various concentrations of Gd-loaded IDA-MSN and Magnevist on a 3 Tesla Siemens Prisma clinical MRI system (Siemens Healthineers, Erlangen, Germany) using a body array matrix and spine array coil. A T_1-weighted image set was first acquired using a spoiled gradient echo sequence (GRE) to serve as a reference. T_1 was measured using a turbo spin echo (TSE) sequence with an inversion recovery scheme. Parameters used were in-plane field of view (FOV): 200mm×200mm; in-plane matrix size: 256×256; slice thickness: 3mm; slice number: 12; echo time (TE): 13ms; repetition time (TR): 8s; bandwidth: 122 Hz/px; inversion times (TI): 50, 100, 150, 200, 300, 500, 750, 1000, 1250, 1500, 2500ms. T_2 was measured using a TSE sequence with the same parameters of FOV, resolution, slice thickness, number of slices, bandwidth and TR. TEs of 25, 37, 49, 62, 86, 99 and 123ms were used. To obtain T_1 and T_2 distribution maps, in-house fitting scripts were written and executed offline in Matlab R2017 (MathWorks, Natwick, MA, USA). Regions of interest (ROIs) were drawn on the resulting T_1 and T_2 maps inside the homogeneous regions inside each sample and the average T_1 and T_2 values of these

samples were recorded.

4.6. Figures

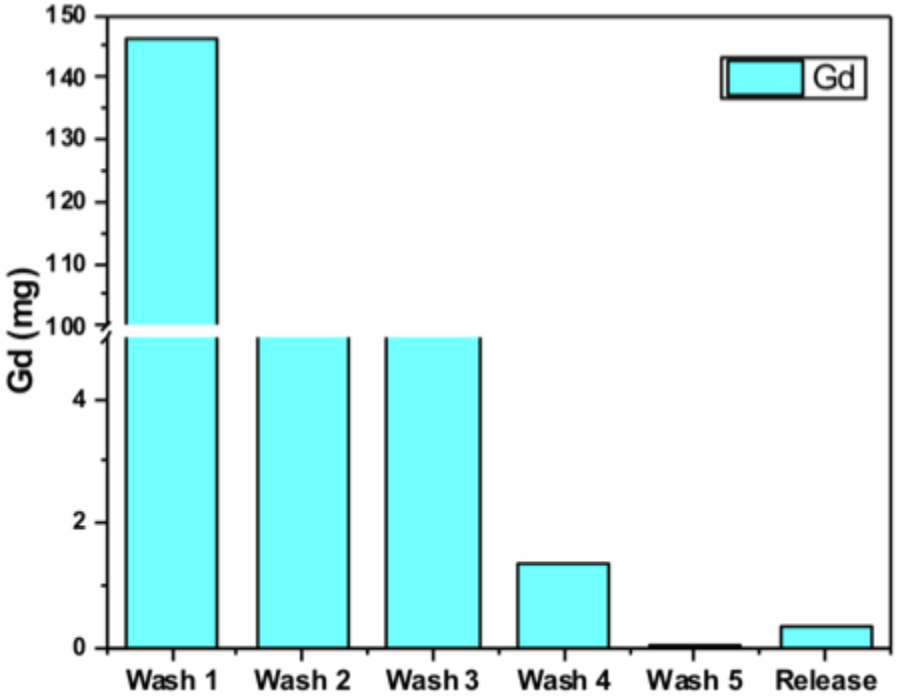

Figure 4.6.1. The supernatant solutions from loading, washing, and releasing steps of loading Gd^{3+} into IDA-MSNs

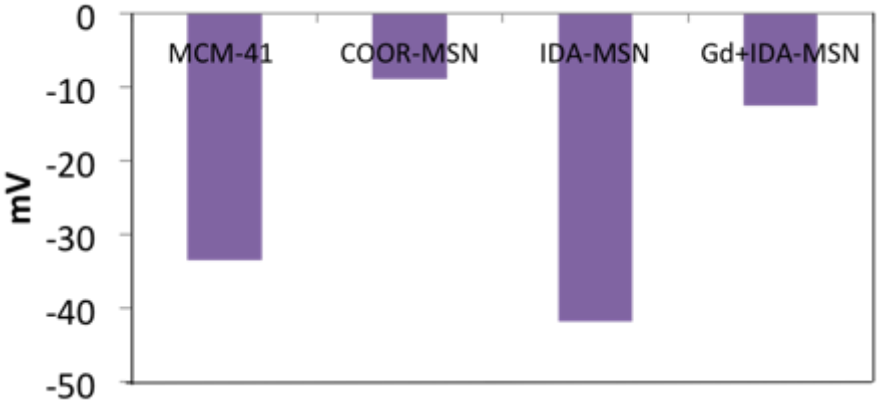

Figure 4.6.2. Zeta potential of MCM-41 after acid extraction, (Diethyl Iminodiacetate)-Propyltriethoxysilane modified MSNs (label as COOR-MSN), IDA-MSNs, and Gd chelated IDA-MSNs.

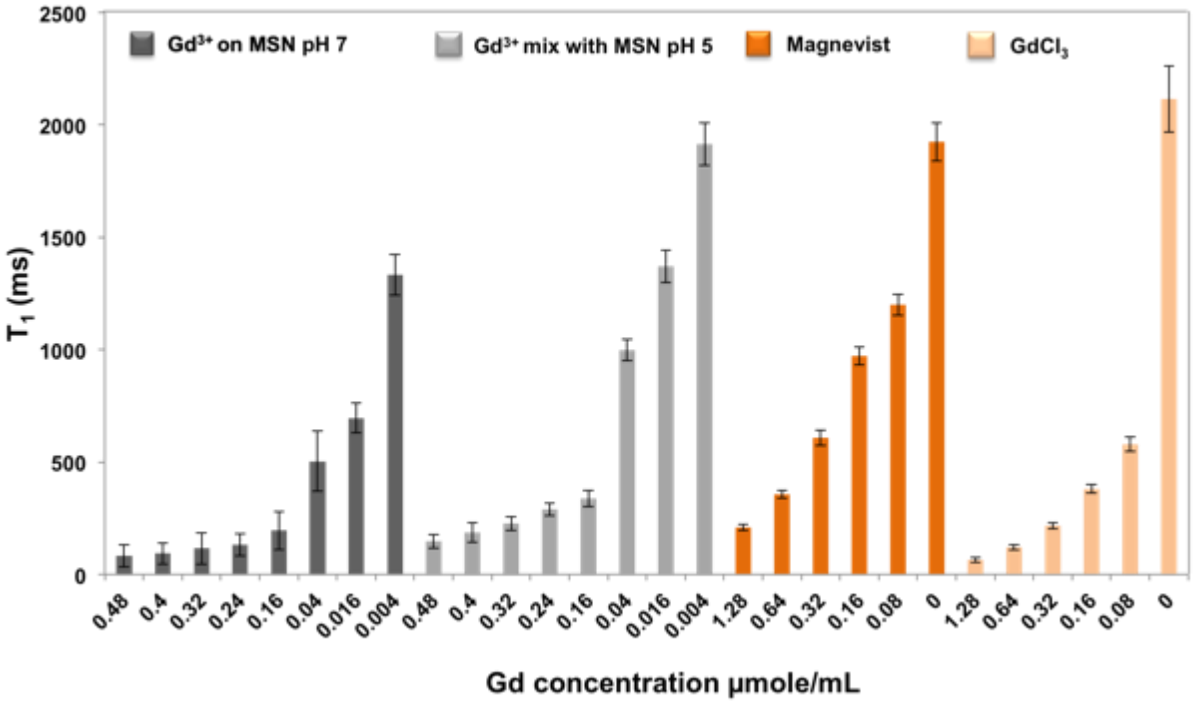

Figure 4.6.3. The T_1 contrast change from various concentrations of Gd^{3+} in different conditions: Gd^{3+} loaded IDA-MSNs at pH 7 (dark grey bar); Gd^{3+} released from MSNs at pH 5 (light grey bar); pure Magnevist Gd(DTPA) (orange bar); $GdCl_3$ (light orange bar)

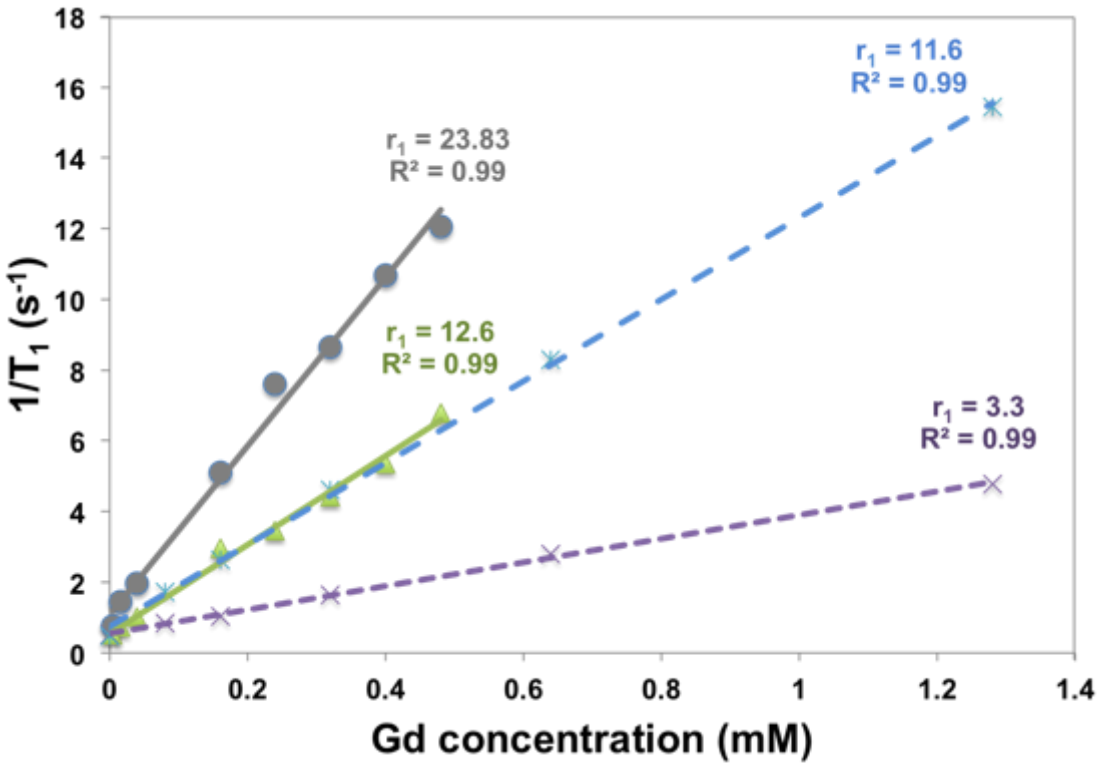

Figure 4.6.4. The relaxivity (r_1) curve of Gd-loaded IDA-MSN at pH 7 (grey dots); pH 5 (blue dots); $GdCl_3$ (green dots); pure Magnevist (purple dots).

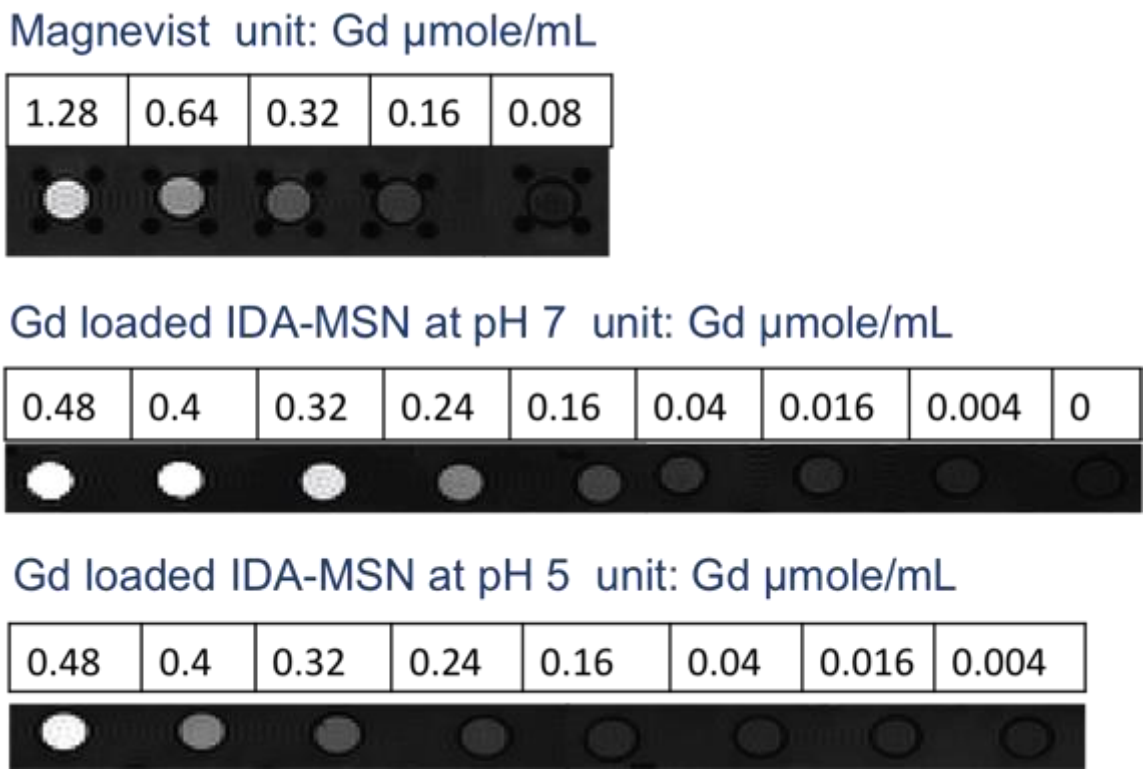

Figure 4.6.5. The MRI images of Magnevist, Gd-loaded IDA-MSN at pH 7, and Gd-loaded IDA-MSN at pH 5.

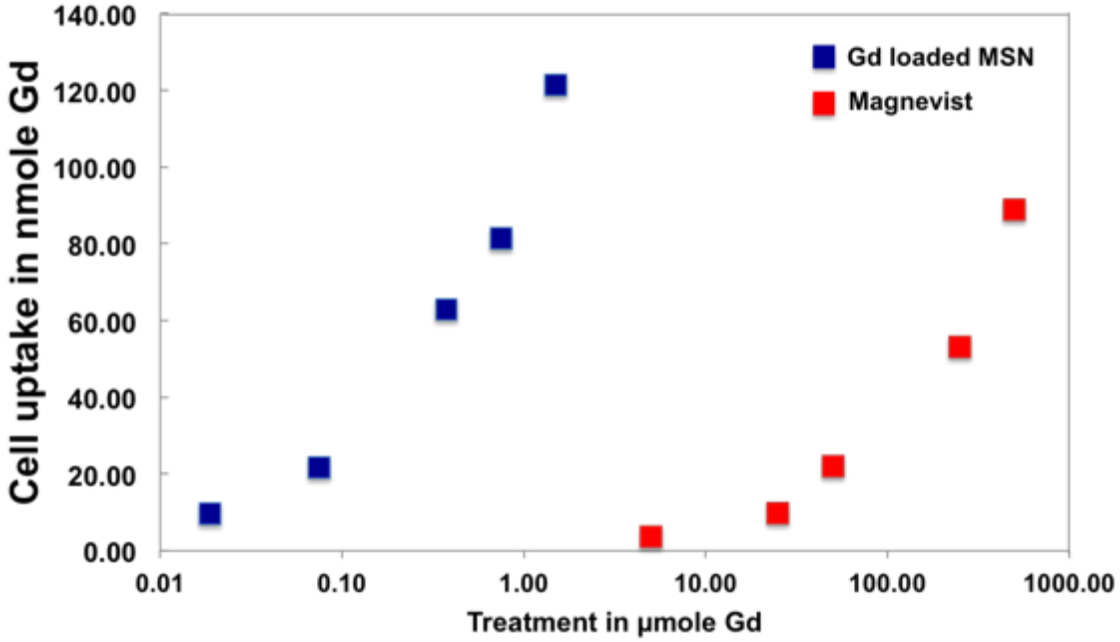

Figure 4.6.6. The cell uptake study of Gd-loaded IDA-MSNs and Magnevist.

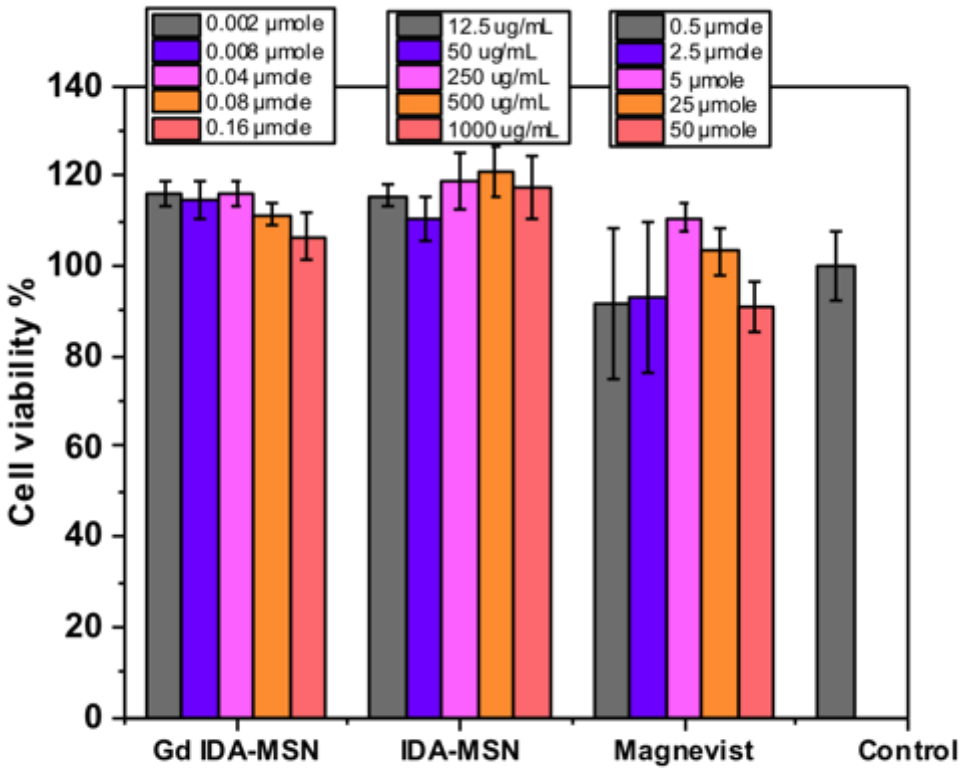

Figure 4.6.7. The PANC-1 cell proliferation data. The MSN mass of Gd-loaded IDA-MSNs and pure IDA-MSNs treatment concentrations are indicated in the second box. The Gd amount carried by IDA-MSNs is indicated in first box. The third box is the µmole of Magnevist/Gd treatment.

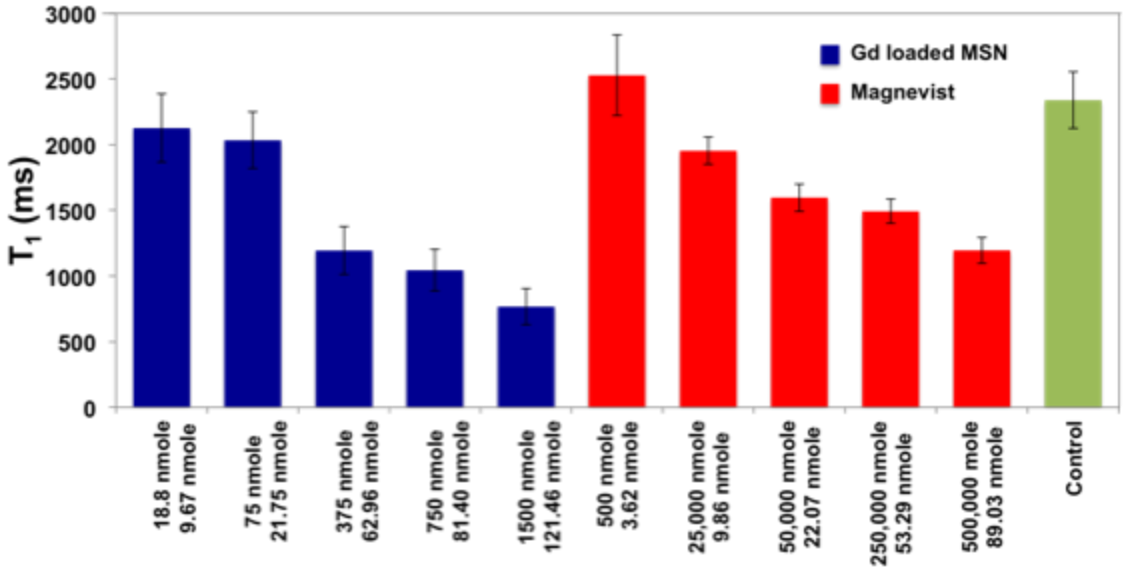

Figure 4.6.8. The T_1 values of Gd-loaded IDA-MSNs (blue bar) and Magnevist (red bar) in the cells. The left numbers of Gd means the treated Gd amount and the right numbers of Gd means the uptaken Gd amount in the cells, respectively. 1 mg IDA-MSNs carries 0.15 μmole Gd.

4.7. Tables

Batch #	Gd release µmole/mg MSN
1	**0.206**
2	**0.159**
3	**0.153**
4	**0.143**
5	**0.139**
6	**0.165**
7	**0.148**
8	**0.232**

Table 4.7.1. The ICP data of released Gd amount from various batches of IDA-MSN.

		Treatment µmole Gd	Cell uptake nmole Gd
Gd IDA-MSNs (mg)	**10**	**1.5**	**121.46**
	5	**0.75**	**81.4**
	2.5	**0.375**	**62.96**
	0.5	**0.075**	**21.75**
	0.125	**0.01875**	**9.67**
Magnevist (µL)	**1000**	**500**	**89.03**
	500	**250**	**53.29**
	100	**50**	**22.07**
	50	**25**	**9.86**
	10	**5**	**3.62**

Table 4.7.2. Detailed number of cell treatment. The second column is the amount of Gd-loaded IDA-MSN (mg) and Magnevist (µL) added into medium for treatments. The third column is the Gd amount (µmole) in the IDA-MSNs and Magnevist. The fourth column is the Gd amount (nmole) taken up by cells.

4.8. References

1 A. Aisen, W. Martel, E. Braunstein, K. McMillin, W. Phillips and T. Kling, *Am. J. Roentgenol.*, 1986, **146**, 749–756.

2 M. Sundaram and R. A. McLeod, *Am. J. Roentgenol.*, 1990, **155**, 817–824.

3 D. Hao, T. Ai, F. Goerner, X. Hu, V. M. Runge and M. Tweedle, *J. Magn. Reson. Imaging*, 2012, **36**, 1060–1071.

4 P. Caravan, J. J. Ellison, T. J. McMurry and R. B. Lauffer, *Chem. Rev.*, 1999, **99**, 2293–2352.

5 J. W. M. Bulte and D. L. Kraitchman, *NMR Biomed.*, 2004, **17**, 484–499.

6 W. J. M. Mulder, G. J. Strijkers, G. A. F. van Tilborg, A. W. Griffioen and K. Nicolay, *NMR Biomed.*, 2006, **19**, 142–164.

7 J. Ramalho, R. C. Semelka, M. Ramalho, R. H. Nunes, M. AlObaidy and M. Castillo, *Am. J. Neuroradiol.*, 2016, **37**, 1192–1198.

8 B. a Waltuck, *J. Qual. Particip.*, 2012, **34**, 13–15.

9 F. D. Hammer, P. P. Goffette, J. Malaise and P. Mathurin, *Eur. Radiol.*, 1999, **9**, 128–136.

10 F. G. Shellock and E. Kanal, *J. Magn. Reson. Imaginging*, 1999, **10**, 477–84.

11 R. Wertman, E. Altun, D. R. Martin, D. G. Mitchell, J. R. Leyendecker, R. B. O'Malley, D. J. Parsons, E. R. Fuller and R. C. Semelka, *Radiology*, 2008, **248**, 799–806.

12 P. Caravan, *Chem. Soc. Rev.*, 2006, **35**, 512.

13 K. Ni, Z. Zhao, Z. Zhang, Z. Zhou, L. Yang, L. Wang, H. Ai and J. Gao, *Nanoscale*, 2016, **8**, 3768–3774.

14 J. Lu, M. Liong, Z. Li, J. I. Zink and F. Tamanoi, *Small*, 2010, **6**, 1794–1805.

15 Z. Li, J. C. Barnes, A. Bosoy, J. F. Stoddart and J. I. Zink, *Chem. Soc. Rev.*, 2012, **41**, 2590.

16 J. E. Lee, N. Lee, T. Kim, J. Kim and T. Hyeon, *Acc. Chem. Res.*, 2011, **44**, 893–902.

17 A. Popat, S. B. Hartono, F. Stahr, J. Liu, S. Z. Qiao and G. Qing (Max) Lu, *Nanoscale*, 2011, **3**, 2801.

18 H. Maeda, J. Wu, T. Sawa, Y. Matsumura and K. Hori, *J. Control. Release*, 2000, **65**, 271–284.

19 A. K. Iyer, G. Khaled, J. Fang and H. Maeda, *Drug Discov. Today*, 2006, **11**, 812–818.

20 J. K. Hsiao, C. P. Tsai, T. H. Chung, Y. Hung, M. Yao, H. M. Liu, C. Y. Mou, C. S. Yang, Y. C. Chen and D. M. Huang, *Small*, 2008, **4**, 1445–1452.

21 Y. Liu, Z. Chen, C. Liu, D. Yu, Z. Lu and N. Zhang, *Biomaterials*, 2011, **32**, 5167–5176.

22 K. Vuu, J. Xie, M. A. McDonald, M. Bernardo, F. Hunter, Y. Zhang, K. Li, M. Bednarski and S. Guccione, *Bioconjug. Chem.*, 2005, **16**, 995–999.

23 Y. Song, X. Xu, K. W. Macrenaris, X.-Z. Zhang, C. A. Mirkin and T. J. Meade, *Angew. Chem. Int. Ed. Engl.*, 2009, **48**, 9143–9147.

24 A. M. Tang, J. S. Ananta, H. Zhao, B. T. Cisneros, E. Y. Lam, S. T. Wong, L. J. Wilson and K. K. Wong, *Contrast Media Mol. Imaging*, 2011, **6**, 93–99.

25 X. Hu, G. Liu, Y. Li, X. Wang and S. Liu, *J. Am. Chem. Soc.*, 2015, **137**, 362–368.

26 D. Tarn, M. Xue and J. I. Zink, *Inorg. Chem.*, 2013, **52**, 2044–2049.

27 Y.-S. Lin, Y. Hung, J.-K. Su, R. Lee, C. Chang, M.-L. Lin and C.-Y. Mou, *J. Phys. Chem. B*, 2004, **108**, 15608–15611.